

FORECASTING THE APPEARANCE AND EVOLUTION OF IONOSPHERIC IRREGULARITIES AND STRUCTURES: THEIR EFFECTS ON AF SYSTEMS

Cesar E. Valladares, et al.

**Boston College Institute of Scientific Research
Kenny Cottle Hall 205
140 Commonwealth Avenue
Chestnut Hill, MA 02467**

21 August 2015

Final Report

APPROVED FOR PUBLIC RELEASE; DISTRIBUTION IS UNLIMITED.



**AIR FORCE RESEARCH LABORATORY
Space Vehicles Directorate
3550 Aberdeen Ave SE
AIR FORCE MATERIEL COMMAND
KIRTLAND AIR FORCE BASE, NM 87117-5776**

DTIC COPY

NOTICE AND SIGNATURE PAGE

Using Government drawings, specifications, or other data included in this document for any purpose other than Government procurement does not in any way obligate the U.S. Government. The fact that the Government formulated or supplied the drawings, specifications, or other data does not license the holder or any other person or corporation; or convey any rights or permission to manufacture, use, or sell any patented invention that may relate to them.

This report was cleared for public release by the 377 ABW Public Affairs Office and is available to the general public, including foreign nationals. Copies may be obtained from the Defense Technical Information Center (DTIC) (<http://www.dtic.mil>).

**AFRL-RV-PS-TR-2015-0159 HAS BEEN REVIEWED AND IS APPROVED FOR
PUBLICATION IN ACCORDANCE WITH ASSIGNED DISTRIBUTION STATEMENT.**

//SIGNED//

Dr. James T. Keeney
Project Manager, AFRL/RVBXR

//SIGNED//

Glenn M. Vaughan, Colonel, USAF
Chief, Battlespace Environment Division

This report is published in the interest of scientific and technical information exchange, and its publication does not constitute the Government's approval or disapproval of its ideas or findings.

REPORT DOCUMENTATION PAGE				<i>Form Approved</i> OMB No. 0704-0188	
<p>Public reporting burden for this collection of information is estimated to average 1 hour per response, including the time for reviewing instructions, searching existing data sources, gathering and maintaining the data needed, and completing and reviewing this collection of information. Send comments regarding this burden estimate or any other aspect of this collection of information, including suggestions for reducing this burden to Department of Defense, Washington Headquarters Services, Directorate for Information Operations and Reports (0704-0188), 1215 Jefferson Davis Highway, Suite 1204, Arlington, VA 22202-4302. Respondents should be aware that notwithstanding any other provision of law, no person shall be subject to any penalty for failing to comply with a collection of information if it does not display a currently valid OMB control number. PLEASE DO NOT RETURN YOUR FORM TO THE ABOVE ADDRESS.</p>					
1. REPORT DATE (DD-MM-YYYY) 21-08-2015		2. REPORT TYPE Final Report		3. DATES COVERED (From - To) 16 Jun 2009 – 16 Aug 2015	
4. TITLE AND SUBTITLE Forecasting the Appearance and Evolution of Ionospheric Irregularities and Structures: Their Effects on AF Systems				5a. CONTRACT NUMBER FA8718-09-C-0041	
				5b. GRANT NUMBER	
				5c. PROGRAM ELEMENT NUMBER 61102F	
6. AUTHOR(S) Cesar E. Valladares, Charles S. Carrano, Keith M. Groves, Vadym Paznukhov and Patricia H. Doherty				5d. PROJECT NUMBER 2301	
				5e. TASK NUMBER PPM00005943	
				5f. WORK UNIT NUMBER EF004621	
7. PERFORMING ORGANIZATION NAME(S) AND ADDRESS(ES) Boston College Institute for Scientific Research Kenny Cottle Hall 205 140 Commonwealth Avenue Chestnut Hill, MA 02467				8. PERFORMING ORGANIZATION REPORT NUMBER	
9. SPONSORING / MONITORING AGENCY NAME(S) AND ADDRESS(ES) Air Force Research Laboratory Space Vehicles Directorate 3550 Aberdeen Avenue SE Kirtland AFB, NM 87117-5776				10. SPONSOR/MONITOR'S ACRONYM(S) AFRL/RVBX	
				11. SPONSOR/MONITOR'S REPORT NUMBER(S) AFRL-RV-PS-TR-2015-0159	
12. DISTRIBUTION / AVAILABILITY STATEMENT Approved for public release; distribution is unlimited. (OPS-15-9311dtd 14 Dec 2015)					
13. SUPPLEMENTARY NOTES					
14. ABSTRACT Work performed under this contract includes scientific and technological research to provide an understanding of the origin and evolution of small to large-scale structures that develop in the ionosphere at polar and equatorial latitudes. These structures and irregularities produce detrimental disturbances on Air Force communication, navigation and surveillance systems. Systems operating at polar latitudes experience disruptions due to the high variability of patch activity that depends on universal time, season, magnetic conditions, solar cycle, and hemisphere. At low latitudes, unwanted effects on systems are even more pronounced as Global Positioning System (GPS) receivers experience loss of signal lock when the ray path traverses an ionospheric plasma bubble. The GPS systems also experience substantial errors in the position on the order of tens of meters due to ionospheric density variability. Our studies have spanned the ascending phase of solar cycle 24, a phase characterized by: (1) an increase of the worldwide background density that degrades the accuracy of navigation systems; and (2) a strengthening of the intensity of scintillations that produces communications outages. The experimental, modeling and assimilation studies described in this report have improved our overall understanding of the high and low-latitude ionospheric processes that may ultimately lead to more reliable and complete forecasts. This contract also supported the operations, maintenance, installation and logistic support of ionospheric instruments that have been deployed around the world in support of the SCINDA and LISN Networks.					
15. SUBJECT TERMS Total Electron Content, TEC, Scintillation, Traveling Ionospheric Disturbances, SCINDA, LISN Ionosonde, Backscatter Radar					
16. SECURITY CLASSIFICATION OF:			17. LIMITATION OF ABSTRACT Unlimited	18. NUMBER OF PAGES 106	19a. NAME OF RESPONSIBLE PERSON Dr. James Keeney
a. REPORT Unclassified	b. ABSTRACT Unclassified	c. THIS PAGE Unclassified			19b. TELEPHONE NUMBER (include area code) (505) 853-1942

This page intentionally left blank.

TABLE OF CONTENTS

Section

List of Figures	iv
1.0 SUMMARY	1
2.0 INTRODUCTION	1
3.0 METHODS, ASSUMPTIONS, AND PROCEDURES.....	2
3.1 Observations, Analysis and Modeling of the Low, Middle and High Latitude Ionosphere	3
3.1.1 Observations of MSTIDs over South and Central America	3
3.1.2 Near Midnight TEC Enhancements over South America.....	7
3.1.3 Characteristics of TIDs using Small and Regional GPS Networks	10
3.1.4 Statistics of TEC Depletions Observed over the South American Continent in 2008	15
3.1.5 The Tropical Ionization Anomaly.....	19
3.1.6 Polar Cap Patches Observed During the Magnetic Storm of November 2003.....	25
3.2 Analysis, Modeling and Simulation of Scintillation Effects on DoD Systems	32
3.2.1 Simulating the Impacts of Scintillation on Space Radar	32
3.2.2 Importance of Decorrelation Time for Modeling Scintillation Impacts on GPS	36
3.2.3 Interpretation and Multi-frequency Scaling of Strong Scintillation	40
3.3 Ionospheric Sensor Installations	49
3.3.1 Maseno, Kenya Ionosonde.....	49
3.3.2 Addis Ababa, Ethiopia Ionosonde	53
3.3.3 Tupiza, Bolivia Ionosonde	55
3.3.4 Coherent Backscatter Radar in Bahir Dar, Ethiopia	56
3.4 Operations and Maintenance of SCINDA	68
3.4.1 Sites and Equipment	70
3.4.2 Performance	71
4.0 RESULTS AND DISCUSSION	84
5.0 CONCLUSIONS	84
REFERENCES	88
LIST OF SYMBOLS, ABBREVIATIONS, AND ACRONYMS.....	91
APPENDIX – EQUIPMENT LIST FOR SCINDA O&M	94

LIST OF FIGURES

Figure	Page
1 MSTIDs Measured between 16 UT on August 20 and 08 UT on August 21, 2011	4
2 dTEC Values Measured by 11 Stations in Colombia and Venezuela	4
3 MSTID's Phase Velocities Calculated using the Cross-Correlation Method (CCM).....	5
4 Image Observed by GOES 12 on August 20, 2011, 23:45 UT	6
5 TEC Measured with the LISN GPS Receiver at Huancayo on March 11-12, 2011	7
6 Regional Maps of TEC Values Measured Over South America on March 12, 2011	8
7 TEC Values along Three Latitudinal Sections Parallel to the Magnetic Field Lines within the South American Continent.....	9
8 Density Profiles Measured by the Jicamarca ISR on March 11 and 12, 2011	10
9 TEC Measured by Three GPS Receivers at Huancayo.....	11
10 Derivation of Different Parameters used by SADM-GPS for GPS Satellites 13 and 25.....	12
11 Cross Correlation Functions and TECP Curves for GPS Satellite 13.....	14
12 Phase Velocity of the TIDs Calculated using the CCM Method and Based on the Data Collected by the Small Array that Operated near Huancayo	14
13 TEC and Scintillations Observed at four South American Locations.....	16
14 Depletions Detected using all GPS Receivers over South America on 2 Days in April 2008....	17
15 Depletions Detected over South America on December 3, 2008.....	18
16 Spatial TEC Depletion Patterns on Two Consecutive Days	19
17 Measured Equivalent Vertical TEC from July 12, 2011 and TEC Resulting from an Interpolation and Fitting Procedure	20
18 Measured Equivalent Vertical TEC from December 12, 2010 and TEC Resulting from an Interpolation and Fitting Procedure	21
19 Temporal Evolution of TEC Observed on June 07, 2011 between 12 and 23 Hours LT	22
20 Temporal Evolution of TEC Values Observed on December 26, 2011 between 12 and 23 Hours LT	22
21 Computer Simulation of the Tropical Anomaly Conducted using the LLIONS Model	24

22	Sequence of Images from Qaanaaq between 2031 and 2053 UT during the Recovery Phase of the Magnetic Storm of November 20, 2003	26
23	630.0 nm Airglow Emissions from Qaanaaq Observed at 2009 UT on November 20, 2003 Projected to 250 km Altitude	27
24	Airglow Images and Vectors of the Patch Drift Velocities Plotted in a Geographic Frame and CG Polar Plot	28
25	Trajectory Analysis of the Patches Observed at Qaanaaq on November 20, 2003 at 2041, 2101, and 2129 UT	29
26	Model Column Emission Rates of Atomic Oxygen Arising from Radiative Recombination, and 630.0 nm Airglow Emissions Corresponding to Patches 2 and 4	30
27	Line-of-Sight Velocities Measured by the Sondrestrom Radar on November 20, 2003	31
28	ALTAIR Observations and Phase Screen Simulations of Radar RCS for a Tracking Scan of RIGIDSHERE-2 on 5 October 2006 Beginning at 1020:45 UTC	34
29	Observed PALSAR Image for 25 December 2007 at 03:20:30 UT during Quiet Ionospheric Conditions	35
30	Observed and Simulated PALSAR Images for 26 March 2008 at 03:19 UT	36
31	Scatter Plot of L1 S ₄ versus Time and 50th, 75th, and 95th Percentile Horizontal Error in the Receiver Reported Position versus Time	37
32	Occurrences of S ₄ Associated with a Loss of Lock Event together with the Probability of Losing Lock versus S ₄	38
33	Occurrences of τ_l that are Associated with a Loss of Lock Event (blue) and all Samples (red) with Probability of Losing Lock versus τ_l	38
34	Probability of Losing Lock versus both S ₄ and τ_l (left); Probability of Losing Lock versus τ_l for three Different Ranges of S ₄ Values (right)	39
35	Geometry of the UHF and L-band Links to Geostationary Satellites FLEETSAT-8 and INMARSAT 3-F2	41
36	Received Power and Intensity Decorrelation Time on the UHF and L-band Links at Ascension Island during the Evening of 22-23 March 2000.....	41
37	Average and Characteristic Zonal Irregularity Drift at Ascension Island during the Evening of 22-23 March 2000	42
38	S ₄ and Normalized Intensity Correlation Length as a Function of the Scattering Strength U for Shallow Spectra with p<3 (left) and Steep Spectra with p>3 (right)	43

39	Measured S_4 at UHF and Intensity Correlation Length for UHF (top) with Measured S_4 at L-band and Predicted S_4 at L-band from the Intensity Correlation Length at UHF using an Unmodified Power Law Irregularity Model with $p=2.5$	44
40	S_4 and Correlation Length for UHF as a Function of Scattering Strength for a two-Component Power Law	44
41	Measured S_4 at UHF and Intensity Correlation Length for UHF (top) with Measured S_4 at L-band and Predicted S_4 at L-band from the Intensity Correlation Length at UHF	45
42	Measured Intensity Spectrum (black) and Least-Squares Fit by the Strong Scatter Model (red) for UHF and L-band at 22.38 UT	46
43	Measured Intensity Spectrum (black) and Least-Squares Fit by the Strong Scatter Model (red) for UHF and L-band at 24.38UT.	46
44	Measured and Predicted S_4 using the IPE Technique for UHF and L-band.....	47
45	Irregularity Parameters Estimated with the IPE Technique	47
46	Scattering Strength Estimated with the IPE Technique at UHF and L-band.....	48
47	Phase Spectrum at Three Times during the Evening	48
48	Ionosonde Field Site at Maseno, Kenya.....	50
49	VIPIR System Installation in Maseno, Kenya	50
50	Daily foF2 Variations Recorded at Maseno on October 30, 31 2013	51
51	Maseno Ionosonde Data Availability.....	52
52	Consecutive Ionograms Recorded at Maseno with Unusual Es Layer Stratification	52
53	Recent Measurements at Maseno, Kenya after Several Repairs.....	53
54	VIPIR System Installation at Addis Ababa, Ethiopia	53
55	Ionogram Recorded by Addis Ababa VIPIR Ionosonde on July 29, 2014.....	54
56	Daily foF2 Variations Recorded at Addis Ababa on 20 June 2014	54
57	VIPIR System Installation at Tupiza, Bolivia	55
58	Ionograms Recorded by the Tupiza VIPIR Ionosonde in November 2012 and January 2013	56
59	Blue Nile Radar Antenna Configuration.....	58
60	System Diagram and Photograph of the Blue Nile Radar System in Bahir Dar	59

61	Types of Daytime Echoes Observed by the Bahir Dar Radar.....	59
62	Post-sunset Echoes Recorded by the Bahir Dar Radar	60
63	Additional Post-sunset Echoes Recorded by the Bahir Dar Radar	60
64	Details of Base Plates and Guy Points	61
65	Side and Front Views of Upper Guy Point Details	61
66	Antenna Elements and Mast Dimensions	62
67	Shorting Bar and Match Tube used in Beta Match Network on Antennas	63
68	VSWR and Complex Impedance Results for a Production Antenna Tested Prior to Shipping	63
69	Antenna Phases Measured with a Network Analyzer at the Power Divider Input	64
70	Phase Differences between Adjacent Antennas in the BNR Array	65
71	Real Impedance for each Antenna Measured on the BNR Array	66
72	Voltage Standing Wave Ratio (VSWR) of the BNR Array	66
73	Location of GPS Receivers Supported under this Contract	69
74	Simplified Diagram Showing Data Flow in the Operational Architecture.	70
75	NovAtel GPS Sensor System: Workhorse of the SCINDA Network	71
76	Collective Availability for the Circled Sites in Western South America	73
77	Collective Availability for the Circled Sites in Central South America	74
78	Collective Availability for the Circled Sites in Eastern South America	75
79	Collective Availability for the Circled Sites in the East Atlantic/West African Region	76
80	Collective Availability for Circled Sites in West Central Africa.....	77
81	Collective Availability for the Circled Sites in Central Africa.....	78
82	Collective Availability for the Circled Sites in East Africa	79
83	Collective Availability for the Circled Sites in Southwest Asia.....	80
84	Collective Availability for the Circled Sites in Indochina.....	81
85	Collective Availability for the Circled Sites in the Western Pacific Region	82

86	Collective Availability for the Circled Sites in the Central Pacific Region.....	83
87	Collective Availability for the Circled Sites in the Eastern Pacific Region.....	84

1.0 SUMMARY

The Boston College Institute for Scientific Research has performed scientific and technological research to provide an understanding of the origin and evolution of small to large-scale structures that develop in the ionosphere at polar and equatorial latitudes. These structures and irregularities produce detrimental disturbances on Air Force communication, navigation and surveillance systems. Systems operating at polar latitudes experience disruptions due to the high variability of patch activity that depends on universal time, season, magnetic conditions, solar cycle, and hemisphere. At low latitudes, unwanted effects on systems are even more pronounced as Global Positioning System (GPS) receivers experience loss of signal lock when the ray path traverses an ionospheric plasma bubble. The GPS system also experiences substantial errors in the position on the order of tens of meters due to ionospheric density variability. Our studies have spanned the ascending phase of solar cycle 24, a phase characterized by: (1) an increase of the worldwide background density that degrades the accuracy of navigation systems; and (2) a strengthening of the intensity of scintillations that produces communications outages. The experimental, modeling and assimilation studies described in this report have improved our overall understanding of the high and low-latitude ionospheric processes that may ultimately lead to more reliable and complete forecasts.

Our efforts under this contract also supported the operations, management, maintenance, installation and logistic support of ionospheric instruments that have been deployed around the world in support of the SCINDA (Scintillation Network and Decision Aid) network and the Low Latitude Sensor Network (LISN). Instruments in these networks include GPS receivers, triaxial fluxgate magnetometers, advanced fully digital ionosondes, and back-scatter radar system. These instruments form distributed observatories able to monitor the ionosphere over large areas of the globe. In addition, these instruments made it possible to study ionospheric features and processes, such as scintillation, Total Electron Content (TEC) and Traveling Ionospheric Disturbances (TIDs).

2.0 INTRODUCTION

The Earth's ionosphere is a continuously varying environment in which energy inputs, mass transfer and momentum exchange play an important role to define its steady state (climatology) and its disturbed state (weather). The primary driving mechanism for the ionosphere-thermosphere system is the Sun's ultraviolet (UV) and extreme ultraviolet (EUV) radiation.

At high latitudes the ionosphere and magnetosphere are strongly coupled by electric fields, currents and particles. Energy and momentum are exchanged between the ionosphere, magnetosphere, and the thermosphere in a complicated way that is not completely understood. The magnetosphere-ionosphere (M-I) coupling is a complex process in which field-aligned currents, Alfvén waves of ionospheric origin, downward (and upward) Poynting flux, plasma outflow from the ionosphere, development of plasma structures, feedback effects produced by the thermospheric dynamics and the neutral wind dynamo are all interlinked, originating several processes having spatial dimensions spanning many orders of magnitude.

When the plasma and magnetic field of the solar wind interact with the Earth's magnetic field, it creates a teardrop shaped magnetosphere. The outer surface of this region is referred as the magnetopause. The magnetopause prevents all but a fraction of the solar wind energy from

entering the magnetosphere. The energy that does not enter the magnetopause is stored in the form of particles and fields in the magnetotail. However, under some circumstances the energy is impulsively released into the ionosphere, a process call substorms, that commonly lasts for several hours. Geomagnetic storms are a sustained, long lived (on the order of days) response to a prolonged period of solar wind flow characterized by a strong interplanetary magnetic field ($> 20\text{nT}$) and sizable kinetic energy. During geomagnetic storms, a substantial energization of the ring currents exists; magnetospheric electric fields, particle precipitation, and current systems intensify leading to prompt penetrating electric fields that can reach mid and low latitudes. Almost simultaneously, the high latitude thermosphere can develop a disturbed dynamo with winds that can travel toward the equator. Magnetospheric particles precipitate into the polar caps heating the thermosphere and launching atmospheric disturbances such as atmospheric gravity waves. At high latitudes the ionospheric E field is dependent on the nature of the solar wind-magnetosphere coupling. When the Interplanetary Magnetic Field (IMF) is directed southward (B_z is negative) a well defined two-cell convection pattern is observed at polar latitudes. When the IMF is directed northward (B_z is positive), the convection pattern may present more than 2 cells with smaller convection velocities.

At low latitudes the ionospheric electric field is produced by the action of the E and F-region dynamos, which are driven by diurnal and semidiurnal wind patterns. The E-field forces the ions to move in the ExB direction at F-region altitudes, and almost parallel to the E-field at low altitudes. This resulting plasma transport and the ion-neutral chemistry affect the ionospheric composition and concentration, which consequently affect the neutral atmosphere dynamics changing the ion drag. These processes are further complicated by the appearance of currents (horizontal and field aligned), polarization charges, and B-parallel motions of the plasma that modify the E field and the resulting ExB motion of the plasma.

For these reasons, the ionosphere cannot be treated as a separate independent entity - even at low latitudes - and concurrent measurements of the solar wind, magnetosphere and thermosphere are highly desirable to elucidate the way the ionosphere couples to its adjacent layers, understand the ionospheric electrodynamics, and discern among competing theories that try to explain the development of plasma structures. Under this contract, Boston College has employed multi-instrument and multiple-site observing strategies to support this approach and to nowcast and forecast the state of the disturbed ionosphere. Due to societal dependence on technological systems, these studies are important as a step to predict and mitigate the adverse effects that the ionosphere produces on radio propagation links, surveillance systems and GPS navigation systems.

This report provides the details, results and conclusions of our studies as three main topics in Section 2. These topics include 1) Observations, Analysis and Modeling of the Low, Middle and High Latitude Ionosphere; 2) Analysis, Modeling and Simulation of Scintillation Effects on DoD Systems; 3) Ionospheric Sensor Installations; and 4) Operations and Maintenance of SCINDA.

3.0 METHODS, ASSUMPTIONS, AND PROCEDURES

This contract consists of many research topics including observations, analysis and modeling of the low, middle and high latitude ionosphere; analysis, modeling and simulation of scintillation effects on DoD systems; ionospheric instrumentation installations; and the operations and maintenance of the SCINDA network. Though there is cooperation and overlap

between the topics, the focus of each, the methodology and discussion is treated separately in this report.

3.1 Observations, Analysis and Modeling of the Low, Middle and High Latitude Ionosphere

3.1.1 Observations of MSTIDs over South and Central America. TEC values measured by GPS receivers that belong to the Low-latitude Ionosphere Sensor Network (LISN) and several other networks that operate in South and Central America were used to study the characteristics and origin of medium-scale traveling ionospheric disturbances (MSTID) in these regions. The TEC perturbations associated with these MSTIDs show a high degree of spatial coherence over distances > 1000 km allowing us to use measurements from receivers spaced by hundreds of km to calculate the MSTID's travel velocities, propagation direction, and scale-size. A pronounced increase in MSTID activity was observed in South and Central America at 16 UT on August 20, 2011 lasting until the end of August 21, 2011. The MSTID velocities show a very variable pattern that depends upon their local time and location. Counter-streaming MSTIDs were observed over the western part of South America on August 21, 2011. Regional maps of tropospheric temperature brightness, measured by the GOES-12 satellite, are used to identify and follow the development of the tropical storm (TS) Irene and several deep convective plumes. MSTIDs were observed propagating away from the TS Irene. This storm moved into the Caribbean region and intensified earlier on August 20 spawning a train of atmospheric gravity waves (AGW). The small scale size, the velocity less than 150 m/s and the close location of several MSTIDs with respect to the TS Irene indicate that these MSTIDs may be the result of primary AGWs that reached the F-region bottomside. These results open the possibility to use TEC values measured by networks of GPS receivers to construct regional, and probably global, maps of MSTIDs, identify their origin and study in detail the characteristics of MSTIDs corresponding to primary and secondary AGWs.

Regional Maps of MSTIDs Occurrence for August 20-21, 2011.

The goal of this section is to relate the dynamics of the MSTIDs observed on August 20-21, 2011 to the existence of a tropical storm in the Caribbean region and deep convective cells that originated within the central and southern parts of South America.

The regional maps of Figure 1 show TEC perturbations associated with the MSTIDs that developed over South and Central America on August 20 and 21, 2011. Each frame corresponds to a 4-hour interval in which we have plotted all the MSTIDs detected by almost all GPS receivers that are presently operating in South America. The first frame show that the MSTID's population increases across the South American continent in a sector limited between -10° and -20° geographic latitude. The following frame, corresponding to the period 20 - 24 UT, displays TEC perturbations (dTEC) persisting in South America, across the same latitudinal sector observed four hours earlier. This frame also shows MSTIDs extending between the Caribbean Sea and the eastern part of Central America. These newly-developed MSTIDs remain active until 08 UT on the following day.

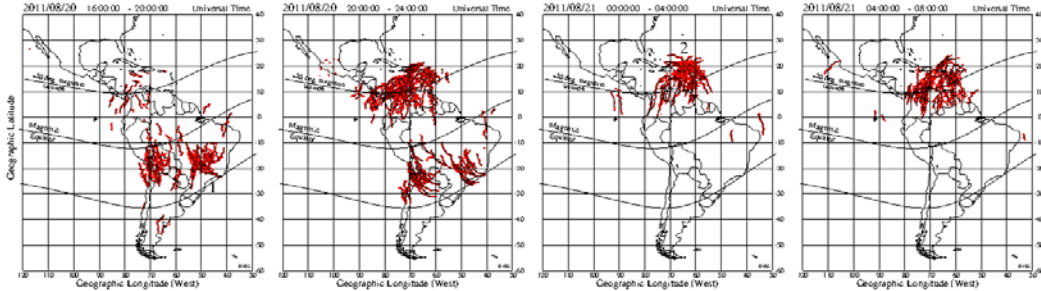


Figure 1. MSTIDs Measured between 16 UT on August 20 and 08 UT on August 21, 2011

Figure 2 displays dTEC perturbations associated with a train of MSTIDs that were detected by one cluster of 11 GPS receivers between 19 and 24 UT on August 20, 2011. These receivers are located in northern Colombia. The dTEC values were derived using signals from the GPS satellite PRN=17. The station's 4-letter name, the latitude and the longitude are indicated in the right margin. Note also that the amplitude of the dTEC is printed at the middle right side and it is equal to 5 TEC units.

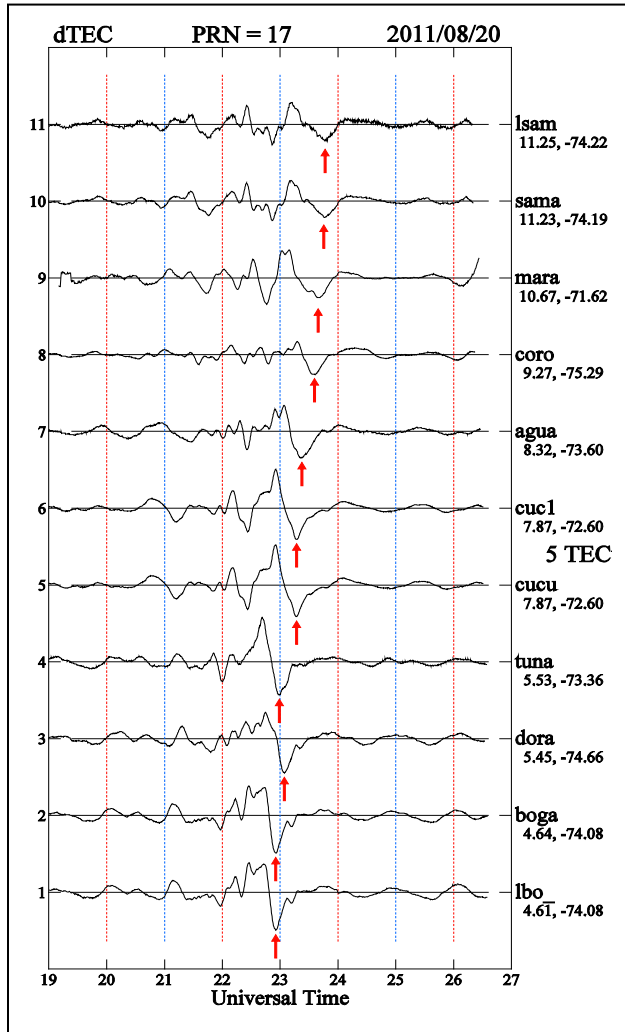


Figure 2. dTEC Values Measured by 11 Stations in Colombia and Venezuela

From top to bottom the stations are organized following their geographic latitude, starting at the top with the station placed further north, Santa Marta (lsam) and ending with Bogota (lbo). This display arrangement helps us to discern the propagation direction of the MSTID. We select a conspicuous feature within the dTEC traces, like the largest minimum or maximum, and determine how this feature time shifts at different sites. Red arrows indicate the time when the largest minimum occurs for each of the eleven traces of Figure 2. As this feature appears at earlier times at sites that are placed further south, it is concluded that the MSTIDs observed on August 20, 2011 in northern Colombia are propagating northward.

Regional Maps of MSTIDs Velocity for August 20-21, 2011

Figure 3 compiles the MSTID's velocity information from the majority of the GPS clusters. Red vectors indicate northward velocities and blue vectors depict velocities with a southward component. The velocity field was decimated a factor of 8 to avoid cluttering the figure. The main characteristic of the plots is the general trend of the velocities: they are principally directed northward or southward. Although, there exist some exceptions and the MSTID velocity can have a small westward or eastward component during the early evening and early hours of the day. On August 20, 2011 at 16 UT, the velocities over South America vary between 200 - 500 m/s. At this time the MSTID's velocities are mainly directed northward with a $\pm 20^\circ$ directional variability. The following frame corresponding to 20-24 UT shows the velocities directed northwestward in the northern part of South America. These velocities intrude into Central America reaching values as high as 400 m/s. There also exists a region near Puerto Rico, where velocities are directed southeastward reaching 420 m/s. The next frame, corresponding to August 21, 2011 at 00-04 UT, displays velocities over the eastern side of the Caribbean region, where the flow is ~ 200 m/s and it is directed southwestward. Downstream in eastern Colombia, the MSTID's velocities were also pointing southwestward, but the velocity magnitude was ~ 300 m/s.

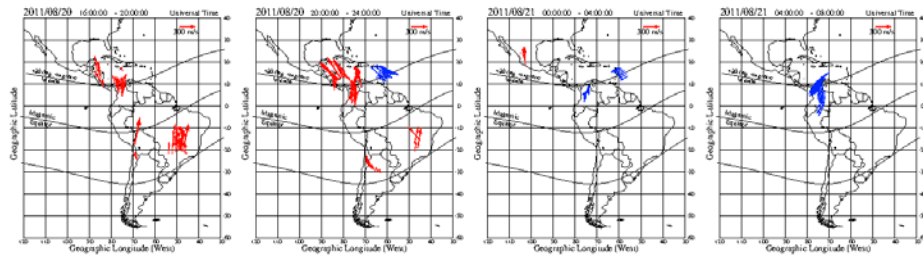


Figure 3. MSTID's Phase Velocities Calculated using the Cross-Correlation Method (CCM)

GOES-12 Infrared Images

The Geostationary Satellite system (GOES) mission provides weather monitoring and forecasting operations, and aids research to understand land, atmosphere, ocean, and climate interactions. GOES-12 was launched in 2001, and has been in standby orbit most of its lifetime. However, during a few months in 2011, GOES-12 operated in the GOES-EAST position, providing coverage of the east coast of the United States and South America.

The satellite measures the temperature of the clouds and the surface of the Earth with an infrared sensor. This allows for the detection of changes in the temperature of clouds during the day and at night. The temperature of the clouds also indicates how tall clouds are since temperature is inversely proportional to height in the atmosphere. Red color indicates the

appearance of temperatures as cold as -80° C and clouds extending up to 11,000-12,000 meters. Several authors have pointed out that the type of clouds that prevail in Central and South America consist of convective plumes able to trigger gravity waves that propagate through the troposphere and mesosphere, which dissipate in the thermosphere (or mesosphere) and create body forces that are able to generate secondary gravity waves that can reach F-region altitudes. Figure 4 shows an image taken with the infrared sensor on-board GOES 12 August 20, 2011 at 23:45 UT.

A few hours later this tropical depression became organized enough to be classified as tropical storm Irene. Figure 4 shows Irene transiting through the Caribbean region before it became a category 1 hurricane. This frame displays a cluster of convective plumes that extended through the southern part of Peru and western Brazil. This frame also provides evidence for the presence of another region of very cold temperatures located to the east of the southern tip of South America and close to Antarctica. This region persists for many hours until 14:45 UT on August 21, 2011.

Conclusions

This analysis has provided regional maps of TEC perturbations associated with the MSTIDs that circulated throughout South and Central America and the Caribbean region on August 20 and 21, 2011. Similar plots can be constructed for other continents such as Africa and Asia to further our understanding on the longitudinal differences that exist in different regions of the Globe.

Calculations of the phase velocity and the scale size of MSTIDs and regional images of tropospheric temperature brightness recorded by the GOES-12 satellite were used to assess the role of a tropical storm and clusters of tropospheric convective cells on the initiation of MSTIDs in the South America continent. A group of MSTIDs, observed in the Caribbean region between 0 and 06 UT on August 21, 2011, were likely associated with primary AGWs. These waves were triggered within the region of TS Irene. These MSTIDs were moving eastward at 140 m/s and had a scales size of 250 km.

MSTIDs associated with primary and secondary AGWs were identified and an estimation of their place and time of origin was calculated using plots of the TEC perturbations in a travel-distance versus universal time format.

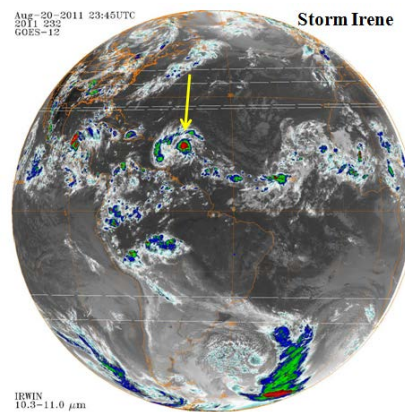


Figure 4. Image Observed by GOES 12 on August 20, 2011, 23:45 UT

3.1.2 Near Midnight TEC Enhancements over South America. Near-midnight TEC enhancements (N-MTECE) consist of sudden increases in TEC that occur after sunset at low latitudes on 30% of the days (during solar minimum conditions). These TEC enhancements last for several hours and can have amplitudes between 1 and 50 TEC units. On March 11-12, 2011 the largest TEC enhancement was observed in South America at times when the Jicamarca incoherent scatter radar operated and observed peak densities above 10^6 el/cc at 300 km altitude. It is suggested that a combination of zonal electric fields and meridional neutral winds are able to redistribute the plasma along the field lines and create regions of enhanced TEC.

Observations of TEC Enhancements

Figure 5 shows the TEC values measured at Huancayo on March 11-12, 2011. This station is located close to the magnetic equator. The important feature is the sudden increase in the local TEC occurring 2-3 hours after sunset and extending for a few hours before and after midnight. However, TEC enhancements can also be observed at magnetic latitudes as high as 10° . The different traces seen in this figure correspond to the TEC values observed using signals from different GPS satellites. At low latitudes, GPS receivers commonly track and lock to signals from 8 to 12 GPS satellites simultaneously. In this research, it was suggested that near-midnight TEC enhancements are produced by the transport of plasma along field lines from latitudes between 15° and 25° to equatorial latitudes. It was also indicated that the presence of a meridional wind can modify the final location of the region of enhanced TEC values.

The TEC enhancement seen on March 11-12, 2011 is the largest N-MTECE ever recorded in South America using GPS receivers. It is expected that during periods of maximum solar activity of the present solar cycle, much larger TEC enhancements will be detected. The color scheme of the TEC values observed between 21 and 24 LT on March 11, 2011 indicates that the peak of the TEC enhancement occurs south of Huancayo and at a geographic latitude equal to 17° S.

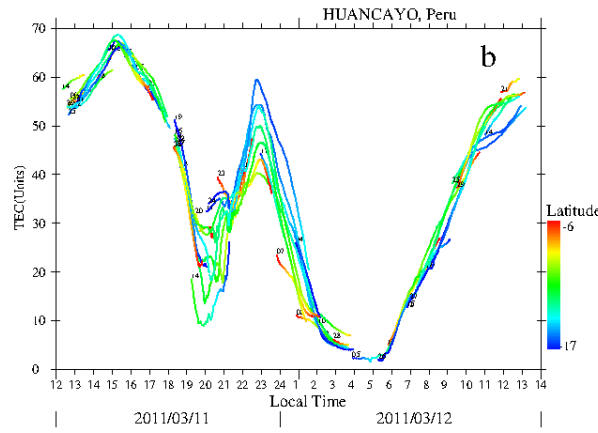


Figure 5. TEC Measured with the LISN GPS Receiver at Huancayo on March 11-12, 2011

Regional Plots of TEC Corresponding to March 12, 2011

Figure 6 shows the temporal variability of TEC measured over South America between 01 and 05 UT on March 12, 2011. Both March 11 and 12, 2011 were magnetically disturbed with a K_p value equal to 5 at the time of the TEC enhancement. Each frame of Figure 6 shows the anomaly exhibiting a sharp longitudinal variability near 58° W. Panels b and c indicate that

the crest of the anomaly decreases by 30 TEC units between 65° W and 50° W. The sequence of TEC images makes it evident that both crests of the anomaly move equatorward between 01 and 04 UT. Figure 6d indicates that the southern crest becomes more intense and outlives the northern crest. This effect is likely the result of a meridional wind that supplies plasma across the magnetic equator.

To quantitatively assess the longitudinal and temporal variability of the anomaly, we extracted TEC values along three latitudinal cuts parallel to the magnetic field lines that cross the magnetic equator at 70° , 60° and 50° W geographic longitude. Figure 7 shows the results of this analysis in which TEC is represented as a function of geographic latitude and universal times between 18 UT on March 11, 2011 and 06 UT on March 12, 2011. The horizontal white lines in each frame indicate the geographic latitude of the magnetic equator that varies from 12° S in the top frame to 4° S in the bottom panel. We used the IGRF model containing coefficients for 2010 to calculate the position of the magnetic equator and the location of the field lines. Figure 7 confirms the existence of a prominent longitudinal variability of the anomaly and the TEC in general across South America. At 00 UT, it is observed that the TEC crests decrease from 60 TEC units in the top panel to 40 TECu at the bottom. The maximum latitudinal separation of the anomaly, which occurs near 01 UT and almost simultaneously in all frames, is about 17° , 17° and 13° from top to bottom. The width of the crests of the anomaly also varies in longitude and it is wider in the western part of the continent.

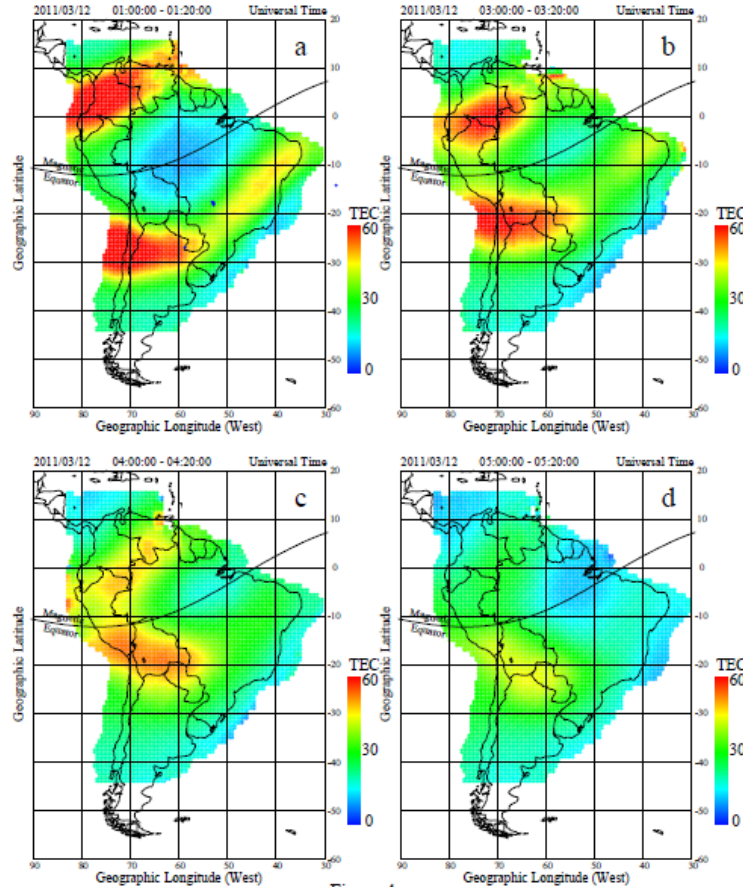


Figure 6. Regional Maps of TEC Values Measured over South America on March 12, 2011

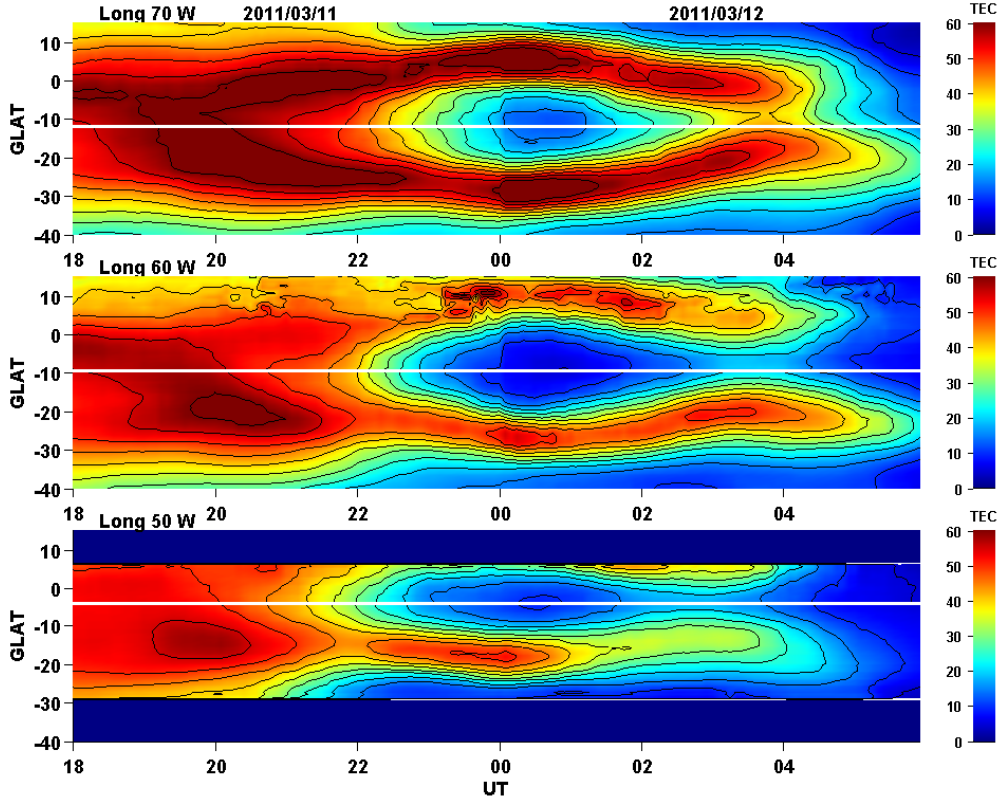


Figure 7. TEC Values along Three Latitudinal Sections Parallel to the Magnetic Field Lines within the South American Continent

Jicamarca Incoherent Scatter Radar Measurements on March 11-12, 2011

Figure 8 shows density profiles measured by the Jicamarca incoherent scatter radar (ISR) on March 11-12, 2011. This figure displays the number density measured as a function of local time (5 hours earlier than UT) and altitude. Coherent echoes were observed briefly in the F-region bottomside between 19 and 21 LT and later at all altitudes between 04 and 06 LT. Figure 8 indicates that the F region elevates from a peak altitude of 400 km at 17 LT to above 600 km at 20 LT. The rise of the F-layer and its subsequent lowering has been described in terms of the pre-reversal enhancement (PRE) of the vertical drift and the post-sunset vortex. During periods of an elevated F-region or a significant PRE, it is common to measure ESF that obscures any attempt to measure the F-region densities. However, during these observations no ESF echoes were observed between 2230 and 0400 LT, therefore, the Jicamarca ISR radar was able to detect the resurgence of the F region near midnight local time hours. In fact, the density over Jicamarca reached a value above $1.4 \times 10^6 \text{ cm}^{-3}$. This value is higher than the peak density (10^6 cm^{-3}) observed at 17 LT. It is also significant that the density profiles between 2230 and 0030 LT show the F-region peak descending in altitude. This observational feature is in agreement with the reverse fountain effect that is driven by a descending F region near the magnetic equator. The observations presented here consist of TEC values measured with the LISN GPS receivers (45) and several other networks of GPSs and density profiles measured with the Jicamarca radar. These data sets offer the possibility to diagnose the formation and decay of TEC enhancements on a regional scale. We have also shown that the TEC enhancements have a limited longitudinal extension, not more than 20° in longitude on March 11-12, 2011 and $\sim 10^\circ$ on October 14, 2008.

It is also indicated that the existent GPS receivers over South America can indicate the locations where N-MTECE occur in a daily basis.

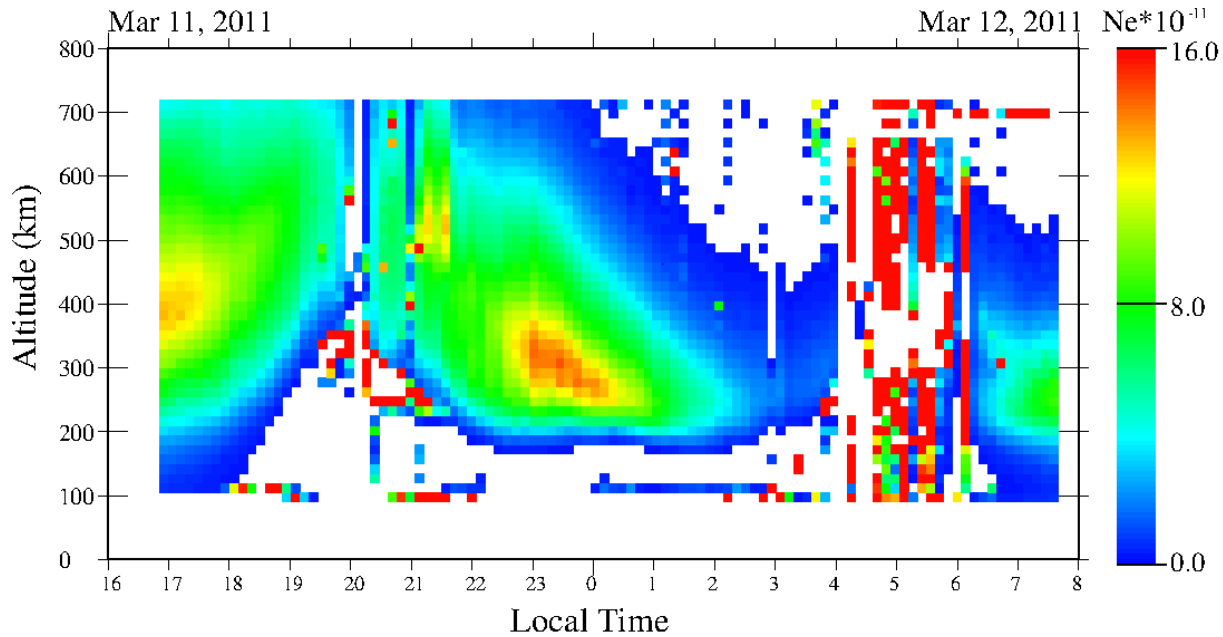


Figure 8. Density Profiles Measured by the Jicamarca ISR on March 11 and 12, 2011

Conclusions.

TEC measurements from the GPS receivers in the LISN distributed observatory were used together with several other receivers that operate in South America to gather the regional distribution of TEC enhancements that occur near midnight at low latitudes. It was shown that the N-MTECE of March 11-12, 2011 was formed by a receding equatorial anomaly driven by a reverse fountain effect acting in response to downward vertical drift. It was also suggested that meridional winds produce an asymmetry in the intensity of the crests controlling the final location of the region of enhanced TEC.

3.1.3 Characteristics of TIDs using Small and Regional GPS Networks. This scientific report presents the results of a dedicated experiment that was conducted within the framework of the Low-latitude ionospheric Sensor Network (LISN) observatory to measure the characteristics of medium-scale (hundreds of km) Traveling Ionospheric Disturbances (TIDs) as they transit through the low-latitude ionosphere. A small array of 3 GPS receivers separated by 4-5 km placed in a triangular configuration was installed near Huancayo in Peru possessing several characteristics of a radio-interferometer. During the campaign days, 17-30 July 2008, TIDs were observed daily. On July 20, 2008 between 22 and 24 UT several TIDs moved across the small array of GPS receivers with a velocity near 130 m/s, were directed northward and had wavelengths close to 450 km. Other GPS receivers that were operating hundreds of km away from Huancayo show also similar TEC traces and provide a phase velocity equal to 150 m/s. This value was measured using the GPS at Piura, Cuzco and Huancayo. Based on this positive result, we conclude that small and/or regional arrays of GPS receivers can be used at low latitudes to study the role that gravity waves may have on seeding plasma bubbles.

TID Observations

A one-month campaign was conducted in South America aiming to characterize the local time, duration, and wave properties of GWs that are transiting near the magnetic equator in the Peruvian sector. We installed two GPS receivers near the city of Huancayo (12.042° S, 75.321° W) due to its proximity to the magnetic equator, the existence of a permanent GPS receiver in that city and the presence of nearby towns. The additional GPS receivers were temporarily installed, one at the town of Chupaca (12.061° S, 75.292° W) and the other at Sicaya (12.021° S, 75.282° W). All 3 GPS receivers of the small network of GPS receivers consist of GSV4004B Novatel GPS using geodetic antennas. Similarly, Novatel GPS receivers were also installed in the cities of Piura and Cuzco.

Each of the frames of Figure 9 present TEC values measured by all 3 GPS receivers that operated near Huancayo on July 20, 2008. The TEC values from different receivers have been color coded to differentiate them and to indicate their similarity. The thin black line, displayed in each frame of Figure 9, indicates an estimate of the background or unperturbed TEC values. This estimate takes into account the typical daily variability of the TEC values that is a function of the local time variability produced by solar EUV radiation, changes in tides, presence of external electric fields and more importantly the TEC variability introduced by the motion of the GPS satellites that continuously samples different latitudes and longitudes. The following figures show the results of an analysis method based on the difference between the measured and the estimated background “unperturbed” TEC values. This differential value is called TEC perturbations (TECP).

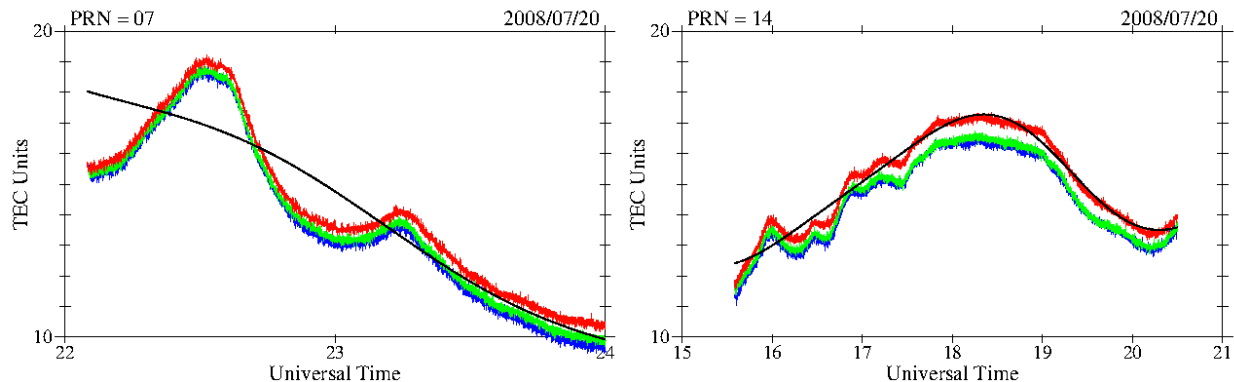


Figure 9. TEC Measured by Three GPS Receivers at Huancayo

Analysis of TID characteristics using SADM-GPS Algorithm

The TIDs horizontal phase velocity $V_h(t)$ and the azimuthal propagation direction of the phase front $\alpha(t)$ was calculated using the Statistical Angle of Arrival and Doppler Method for GPS interferometry (SADM-GPS) [Afraimovich et al, 1998].

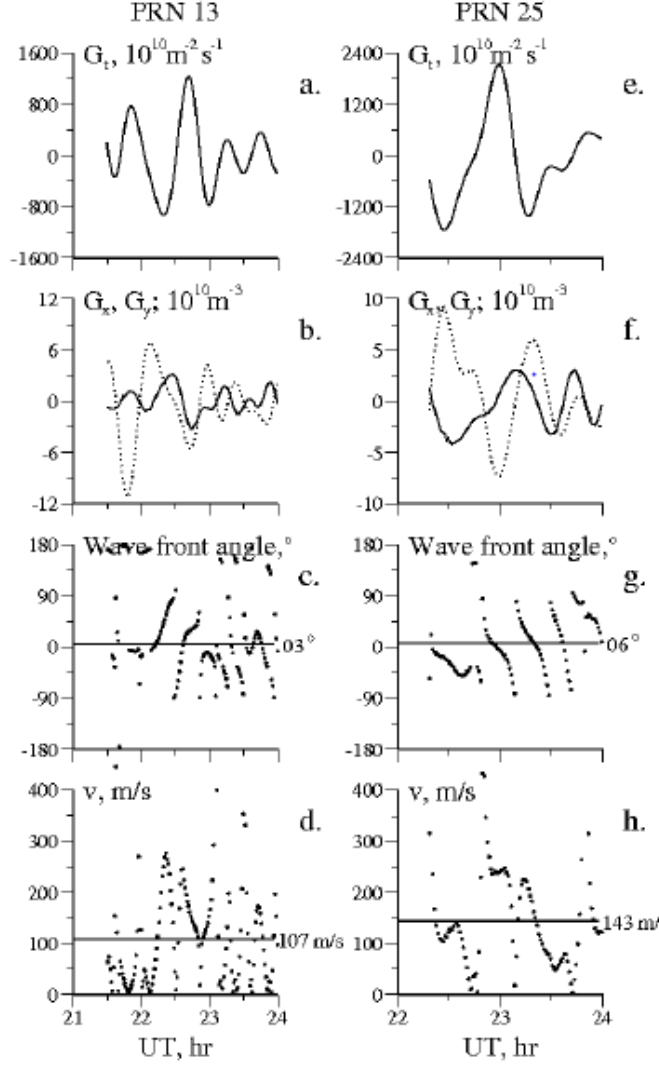


Figure 10. Derivation of Different Parameters used by SADM-GPS for GPS Satellites 13 and 25

This method assumes that the ionosphere changes in a non-dispersive manner due to the passage of the TID or a packet of TIDs. The SADM-GPS represents the TEC perturbations by the form: $I(x,y,t) = \delta(t) \sin(\Omega t - k_x x - k_y y + \varphi_0)$. This expression implies that a monochromatic or a largely dominant TID propagates through the field-of-view of the small receiver network. Using the equation mentioned above, it can be demonstrated that the TID wave parameters can be calculated using:

$$\alpha(t) = \arctan(I'_x(t)/I'_y(t)) = \arctan(G_x/G_y) \quad (1)$$

$$u_x(t) = I'_t(t)/I'_x(t) \quad (2)$$

$$u_y(t) = I'_t(t)/I'_y(t) \quad (3)$$

$$u(t) = \sqrt{u_x(t)u_y(t)}/(u_x^2(t) + u_y^2(t))^{1/2} \quad (4)$$

$$V_h(t) = u(t) + w_x(t) \sin \alpha(t) + w_y(t) \cos \alpha(t) \quad (5)$$

$$G_x = (Y_A(TECP_B - TECP_C) - Y_C(TECP_B - TECP_A))/(X_A Y_C - X_C Y_A) \quad (6)$$

$$G_y = (X_C(TECP_B - TECP_A) - X_A(TECP_B - TECP_C))/(X_A Y_C - X_C Y_A) \quad (7)$$

Where $I'_x(t)$, $I'_y(t)$, $I'_t(t)$ are the spatial and time derivatives of the TECP values. $u_x(t)$, $u_y(t)$ are the propagation velocities of the phase front along the x (east) and y (North) axis in a frame of reference centered at the Huancayo station. $w_x(t)$, and $w_y(t)$ are the x and y projections of the sub-ionospheric intersection point velocity. Note that G_x and G_y symbols used in Figure 10 are equivalent to the $I'_x(t)$ and $I'_y(t)$ derivatives. As the velocity of the sub-ionospheric intersection (80-100 m/s) is comparable to the speed of the GWs, it becomes imperative to subtract this effect from the estimated phase velocity $u(t)$. Equation (5) includes this correction in which the component of the satellite velocity in the direction perpendicular to the phase front is subtracted to determine the true horizontal velocity of the TID.

Figure 10 presents the results of applying equations 1 thru 7 to the TECP values measured on July 20, 2008 between 21 and 24 UT. Panels a and e show the time derivative (G_t) of the TECP measured at Huancayo from GPS satellites 13 and 25 respectively. Panels b and f display the east-west (G_x) spatial derivative using a solid line, and the north-south (G_y) spatial derivatives using dots. Note that equation 6 (G_x) and 7 (G_y) are a function of the TECP values measured by all 3 GPS receivers belonging to the small array. Panels c and g present the angle of the wave front, $\alpha(t)$, that was calculated using equation 1. It is noted that this angle is measured clockwise with respect to geographic north. Panels d and h introduce the phase velocity of the TID calculated using equation (5). The large scatter of the $\alpha(t)$ and $V_h(t)$ values is caused by the non-monochromatic nature of the TECP values. However, the average lines in these frames indicate our best estimate of the TID phase velocity that varies between 3° and 6° . The estimation of the horizontal velocity of the dominant TID falls between 107 and 143 m/s. Comparison of the G_t traces for satellite 13 and 25 (panels a and e) show largely different magnitudes; this is due to the different look angle direction that varies between these two GPS satellites. GPS satellite 13 passed 200 km away from Huancayo and GPS 25 went over Huancayo almost overhead.

Analysis of TID Characteristics using Cross-correlation Algorithm

The cross-correlation method (CCM) aims to calculate the running cross-correlation function using TECP traces originated from any of the GPS satellites, but measured by two different receivers. The cross-correlation function is calculated every minute using segments of TECP data one hour long. We use TECP values from the same GPS satellite due to the motion of the satellite that produces the same temporal delay or advance on receivers placed at relatively close distances. This satellite motion effect can be removed after we calculate the phase velocity. Figure 11 shows the results of the CCM method based on signals from the GPS 13 satellite recorded at Huancayo and Chupaca. The right frame of Figure 11 shows the same analysis using the TECP values measured at Huancayo and Sicaya. The lower panels show the TECP traces for GPS 13 in TEC units observed on July 20, 2008 and between 20 and 24 UT. The lower left frame displays the TECP values measured at Huancayo (blue line) and Chupaca (green line). The cross-correlation functions, displayed in the upper frames, indicate that the

time delay is of order 10 sec. The propagation direction and velocity of the TID was obtained using:

$$\alpha(t) = \arctan((Y_C T_{B-A} - Y_A T_{B-C}) / (X_C T_{B-A} - X_A T_{B-C})) \quad (8)$$

$$V_h(t) = (Y_C \cos(\alpha(t)) - X_C \sin(\alpha(t))) / T_{B-C} + w_x(t) \sin \alpha(t) + w_y(t) \cos \alpha(t) \quad (9)$$

T_{B-A} and T_{B-C} are the time delay between the Huancayo and Sicaya TEC perturbations and the offset time between the Huancayo and Chupaca TECP traces. As in the previous section, $w_x(t)$ and $w_y(t)$ are the projections of the sub-ionospheric intersection point velocity.

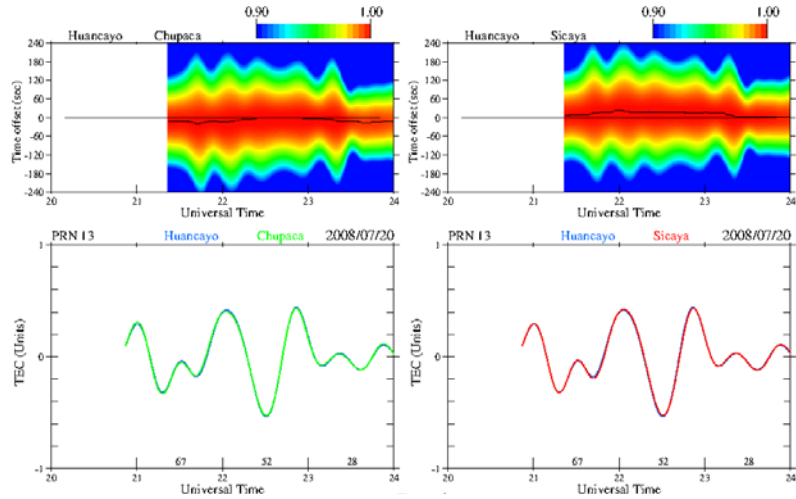


Figure 11. Cross Correlation Functions and TECP Curves for GPS Satellite 13

A quantitative estimation of the TID phase velocity was obtained using equations (8) and (9). Figure 12 shows the magnitude and direction of the TID phase velocity represented by arrows. The size of the arrow is proportional to the phase velocity and the azimuthal rotation of the vector is a function of the propagation angle. It is evident that between 22 and 24 UT, the TID moved toward geographic north. A wavelength equal to 449 km is obtained using the true phase velocity of the TID and the velocity of the satellite sub-ionospheric intersection point. The phase velocity varied between 84 m/s and 144 m/s near 24 UT.

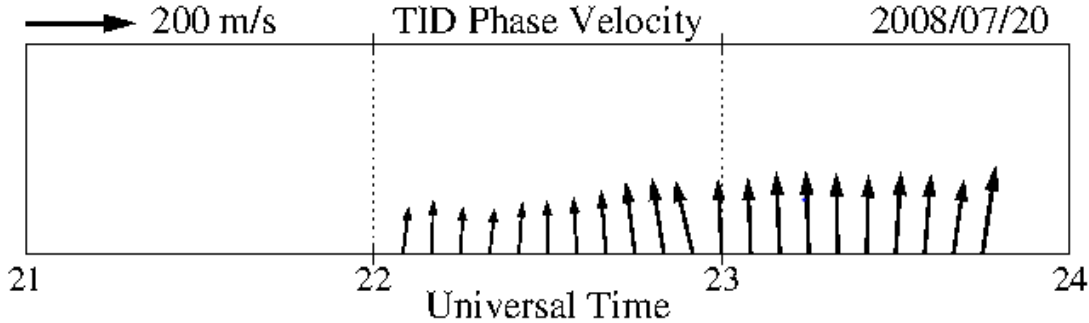


Figure 12. Phase Velocity of the TIDs Calculated using the CCM Method and Based on the Data Collected by the Small Array that Operated near Huancayo

Conclusions.

This research effort presented calculations of the phase velocity, scale size, and angle of propagation of TIDs that are likely originated by gravity waves that are propagating in the north-western side of the South American continent. The values that were obtained using the SADM-GPS and the CCM methods are consistent with values of medium scale TIDs observed by other authors. We calculated that on July 20, 2008, the propagation velocity and the azimuth direction of the TIDs were 140 m/s and parallel to geographic north.

We also applied the CCM method to stations separated by hundreds of km, like Huancayo, Cuzco and Piura. It was unexpected to find a large coherence between the TECP traces from all the adjacent stations, allowing us to determine the morphological characteristics of the TIDs. This result opens the possibility of using measurements of the TEC perturbations by the GPS receivers already deployed in South America to monitor TID activity.

3.1.4 Statistics of TEC Depletions Observed over the South American Continent in 2008.

This work and resultant paper presented the first regional study of TEC depletions derived from GPS observations over the South American continent. The spatial coverage extended over 45° of longitude (i.e., 35° to 80° W). We introduced a new numerical algorithm developed to automatically detect TEC bite-outs that are produced by the transit of equatorial plasma bubbles. This algorithm was applied to TEC values measured by the Low Latitude Ionospheric Sensor Network (LISN) and by receivers that belong to 3 other networks that exist in South America. The general characteristics of the TEC depletions are provided along with their temporal length, local time distribution and depletion depth. The regional day-to-day and seasonal variability of the TEC depletions are also presented for 2008, a year of low solar activity. The regional day-to-day variability of TEC depletions is highly dynamic, but their seasonal distributions follow the longitudinal characteristics of plasma bubbles presented by other authors. It was found that during the equinoxes, TEC depletions are mainly observed on the west coast of South America, and during the December solstice they mostly occur on the east side of the continent.

TEC Depletions

TEC depletions consist of abrupt decreases in the TEC value that last from 10 to 60 minutes. They are commonly followed by a recovery to the TEC value preceding the depletion. The TEC depletions that we are considering are produced by plasma bubbles drifting across the line-of-sight between the GPS receiver and the satellite. Figures 13a and 13b present TEC depletions recorded on the same day, containing similar levels of unperturbed TEC values, at stations located near the magnetic equator but separated by 21° in longitude. The level of Scintillation S_4 index within the depletions varies drastically. Figure 13a shows the TEC recorded at Ancon, Peru for PRN 16 on February 13, 2008. Ancon (11.77° S, 77.15° W) is located near the magnetic equator on the west coast of South America. Two depletions are identified in this pass; no scintillation above the noise level is observed for the first depletion, which may be attributed to the smaller TEC gradients at the edge of the depletion. A moderate scintillation patch of about $S_4 = 0.2$ is observed in correspondence with the second depletion when the satellite elevation angle is more than 60° and has much steeper TEC gradient than the first depletion. It is mentioned that the highest S_4 values were observed on the eastern side of the depletion.

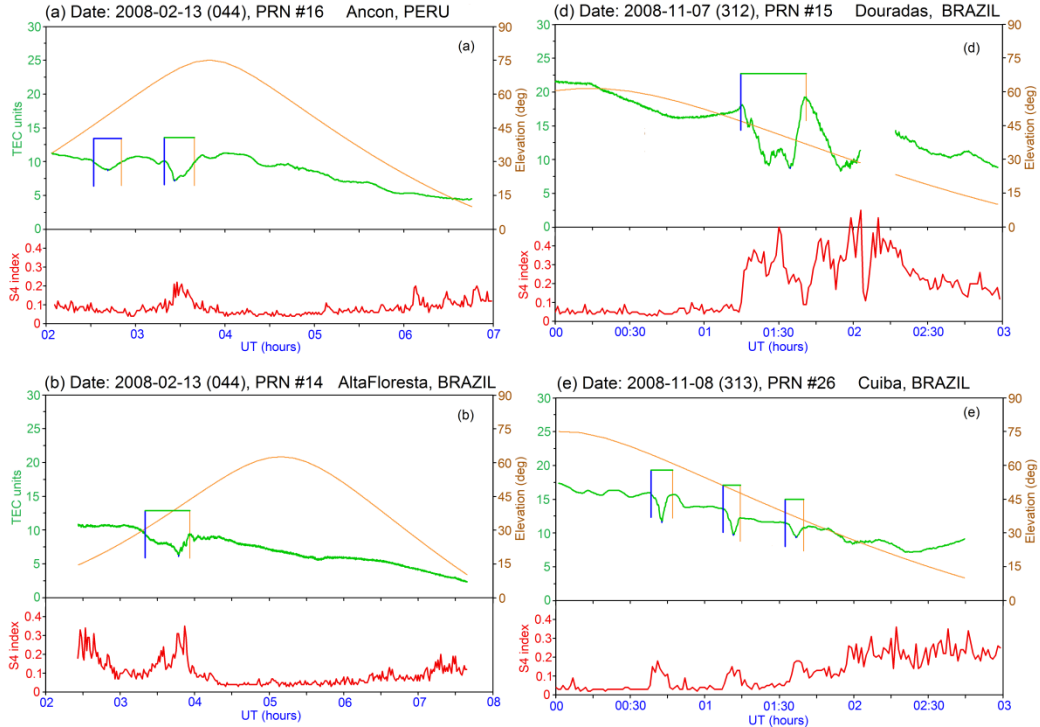


Figure 13. TEC and Scintillations Observed at four South American Locations

The TEC depletions of Figure 13d were accompanied by a stronger level of scintillation than figure 13a and 13b that generated a loss of signal by 25 min. Figure 13d shows an example of a deep depletion and strong scintillations that were observed at the anomaly station of Dourados (22.1° S, 54.9° W). There are two depletions in the TEC data, but just one depletion was detected by the program. The second depletion (UT \sim 02) was not detected due to the loss of L2 signal probably related to the deep fading associated with the high scintillation activity at the second depletion. The first depletion is associated with strong scintillations $S_4 = 0.5$ (>10 dB) at elevation angle of 40° and has large electron density at both edges of the depletion. The second depletion started within few minutes after the first is also accompanied by strong scintillations $S_4 > 0.6$ at elevation angle of about 30° . Due to the depth and length of the second depletion, the receiver lost lock on the L2 signal and TEC was not calculated during this time.

The automatic detection of the narrow (15 min) multiple TEC depletions of Figure 13e are confirmed by the level of scintillations that slightly exceeds the noise level. Figure 13e shows TEC from the anomaly station Cuiba (15.5° S, 56.07° W) for PRN 26 on Nov 8, 2008. Three depletions are detected from this satellite pass, and these depletions have good correspondence with the occurrence of scintillation patches. The scintillation patch corresponding to the third depletion, which is above the elevation angle of 30° shows S_4 index equal to 0.2.

Day to Day Variability of TEC Depletions during Equinoxes

Figures 14a and 14b show the spatial distributions of detected depletions from all the GPS receiver stations in South American region for April 18 and 26, 2008 respectively. The depletions identified in these plots correspond to the time window of 2200 UT to 0700 UT of the following day. This universal time interval covers local time between sunset and few hours after

midnight in the South American longitudes. The colored segments are the GPS satellite tracks at the ionospheric pierce point for the altitude of 350 km. Each segment represents the line joining the start and end points of depletion identified region from each of the GPS satellites. The color coding is done according to the depth of the detected depletion in TEC units as in the color scale. Due to the relatively slow east-west motion of the GPS satellites, we can say that the plasma depletions are traversing a quasi-stationary receiver-satellite link. The depletion duration identified from GPS TEC is a function of the bubble width and the satellite elevation.

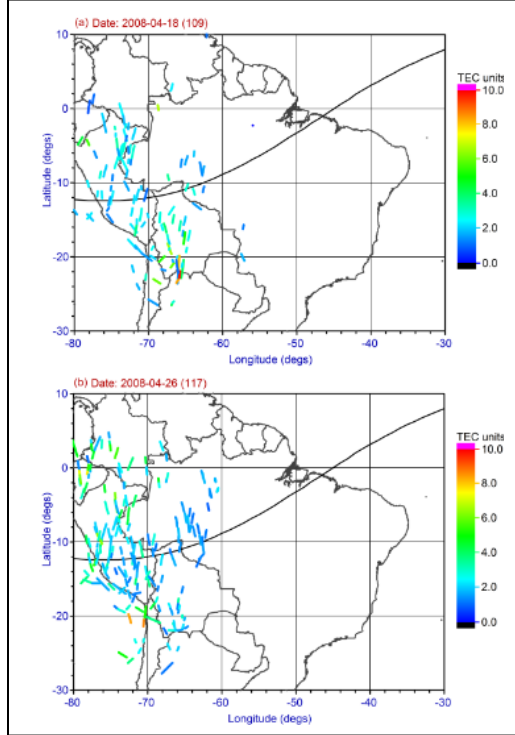


Figure 14. Depletions Detected using all GPS Receivers over South America on 2 Days in April 2008

In Figure 14a, the identified depletions on this day of Apr 18, 2008 have depletion depths falling into ranges of 1 to 4 TEC units, and most of these are along the longitude range of 80° to 60° W. These depletions have the apparent onset times (as observed by the satellite signal) between 2100 to post midnight 0100 hours local time (LT). The onset times were not represented in these figures.

Figure 14b shows the depletions detected on April 26, 2008 with depths varying from 2 to 7 TEC units. The depletions on this day can be identified from two different ionospheric irregularities depending on their onset times. The depletions in the longitude range of 80° to 70° W were detected between about 1930 to 2200 LT; and those in the longitude range of 70° to 60° W have onset times of 2300 to 0100 LT. The depletions with slightly larger TEC depths are concentrated into the anomaly regions. It can be seen from Figures 14a and 14b, that the depletions identified over the South American region are concentrated in the western South American region with no occurrence in the eastern side for these two days. The depletion behavior presented in these figure follows the Tsunoda's 1985 hypothesis of solar terminator – magnetic meridian alignment. But, there are also some days during the equinoxes that do not follow this hypothesis.

Day to Day Variability of TEC Depletions during December Solstice

Figure 15, corresponding to December 3, 2008, show most of the TEC depletions concentrated in the eastern longitudes of the South American region with practically no depletions in the western side. They have the onset times in the range of 2030 to 0030 LT. This behavior follows Tsunoda's hypothesis of the solar terminator – magnetic meridian alignment, which is true for most of the days in December solstice. The depletion depths of these two days are in the ranges of 2 to 8 TEC units. On the day of December 10, 2008 (not shown) there are two concentrated groups of depletions identified which are possibly due to two different irregularity regions with different onset times; the longitudes 45° to 34° W are in the range of 2000 to 2200 LT and the longitudes 58° to 45° W are from 2230 to 0130 LT. Figure 15 represents typical depletion patterns during the December solstice

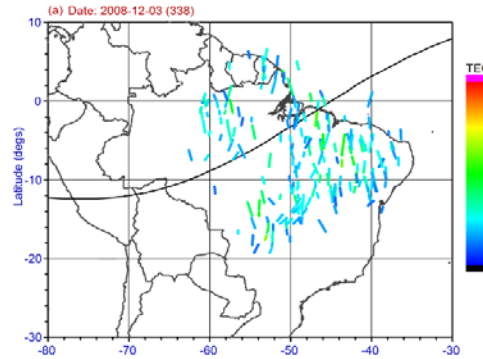


Figure 15. Depletions Detected over South America on December 3, 2008

Spatial TEC Depletion Patterns

Figures 16 a and b present the depletions identified on the consecutive days of February 11 and 12, 2008 showing different patterns of depletion detections in the South American region. On the day of February 11, 2008 (Figure 16a) the depletions are identified in the eastern longitudes of the South American continent, with onset times of about 2130 to 0030 LT, with depletions depths in the range of 1 to 4 TEC units. On February 12, 2008 the depletions are detected in the western longitudes of the South American region with onset times of about 2100 to post midnight 0130 LT, with depletions depths in the range of 1 to 6 TEC units. On the day of February 14, 2008 (not shown) the depletions were identified at all longitudes over South America, the onset times for longitudes between 60° W and 40° W was 2000 to 2200 LT and for longitudes between 80° W to 60° W was about 2100 to post midnight 0130 LT. The range of depletion depths on this day is from 2 to 10 TEC units. Deeper TEC depletions were observed near both anomaly crest regions. The dynamics of depletion occurrence depicted in Figure 16 is a contradiction to the hypotheses of solar terminator alignment as suggested by Tsunoda (1985).

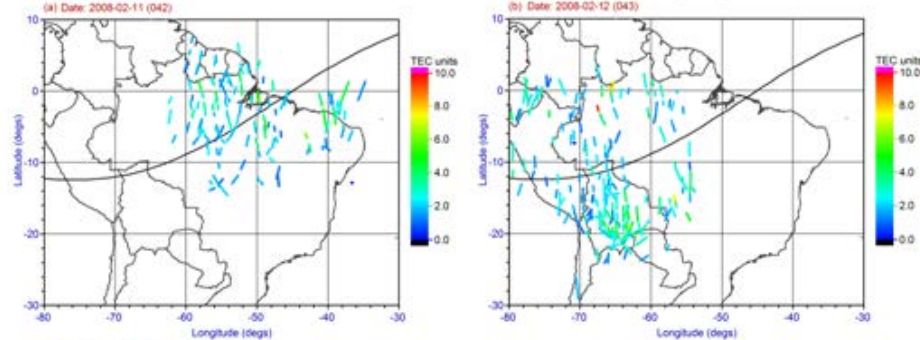


Figure 16. Spatial TEC Depletion Patterns on Two Consecutive Days

Conclusions.

This work resulted in a publication by Seemala and Valladares (2011) that focused on the day-to-day variability of the TEC depletions over the South American continent for the entire year of 2008. Observations of depletions in this year of low solar activity show that the seasonal and longitudinal variability is comparable to that obtained by other authors based on in-situ satellite measurements.

It can be concluded that the climatology of depletions agree with *Tsunoda*'s hypothesis on the alignment of the sunset terminator and the local magnetic field lines. However, the day-to-day variability cannot be easily reconciled with these theories. The statistics of TEC depletions depths show that in 2008, the most probable depths are small in the range of 2 to 3 TEC units and the most likely east-west extents are in the range of 15 to 35 minutes, with maximum local time occurrence falling around 2130 local time hours.

The day-to-day variability that stands out of usual seasonal and longitudinal pattern for the occurrence of equatorial plasma depletions may be explained by the wind-driven gradient-drift instability or a collisional Kelvin-Helmholtz instability. Eastward neutral winds in regions of westward plasma flows, can generate the proper conditions for bubbles to develop. The eastward zonal winds can also drive 10s of km scale density waves with wave fronts tilted 45° to the west during the initial phase of the post-sunset vortex. These waves can serve as seeds for the larger scale plasma bubbles. The collisional shear instability can also seed equatorial spread F based upon the fact that strong shears exists in the bottomside equatorial F region ionosphere around twilight, where the plasma flow in the bottomside reverses from westward to eastward with increasing altitude. Shear flow develops in the equatorial ionosphere beginning around 14 LT each day and intensifies at twilight as the E and valley regions recombine. Several authors have postulated that the gravity waves generated by mesoscale convective systems, which are usually found within the ITCZ are responsible for the seeding mechanisms for plasma depletions. We may assume that the day-to-day variability in the occurrence of TEC depletions may be related to the day to day variability in location of ITCZ with respect to the magnetic equator. This investigation of the possible relationship between the day-to-day variability in plasma depletions and ITCZ requires further study.

3.1.5 The Tropical Ionization Anomaly. Continuous and regional measurements of total electron content (TEC) over the Americas have revealed that quite frequently the largest TEC values reside over Central America. These unexpected and anomalous TEC values have not been reported before. They are observed during the June solstice afternoon hours, last for a few hours, are constrained to regions of eastward magnetic declination and occur at magnetic

latitudes poleward of 20° . During the December solstice, similar TEC enhancements are seen over the southern coast of Brazil, also poleward of 20° , but in a region where the declination is westward. It is proposed and demonstrated using a physics-based model of the low-latitude ionosphere, that the TEC enhancements are produced by the neutral winds blowing at longitudes where the Earth's magnetic declination is different from zero. Due to their anomalous character, the TEC enhancements have been designated as the tropical ionization anomaly.

TEC Data Description

Figure 17 and 18 depict the unique seasonal and spatial characteristics of the tropical ionization TEC enhancements. These TEC regional maps were measured during the June (Figure 17) and the December (Figure 18) solstice seasons. The left frames of Figures 17 and 18 display the actual equivalent vertical TEC values measured by the GPS receivers. The right frames show the results of an interpolation and fitting procedure that provides TEC values every $1/2^{\circ}$ in longitude and latitude. The interpolation is conducted by dividing the continent into several overlapping areas that extend 8° in longitude and 8° in latitude. A 10-term, third order dependence in latitude and longitude is least-square fitted to find only 4 TEC values at the center of the $8^{\circ} \times 8^{\circ}$ square in an area that is only 1° on the side. Accepting or rejecting the fitted results depend on two constraints: (1) 50 or more points and (2) three or more quadrants of the examined area populated with TEC values. A new $8^{\circ} \times 8^{\circ}$ area is considered by successively advancing 1° in latitude and then 1° in longitude. Commonly, a total of 15,000 fitted values are obtained per image.

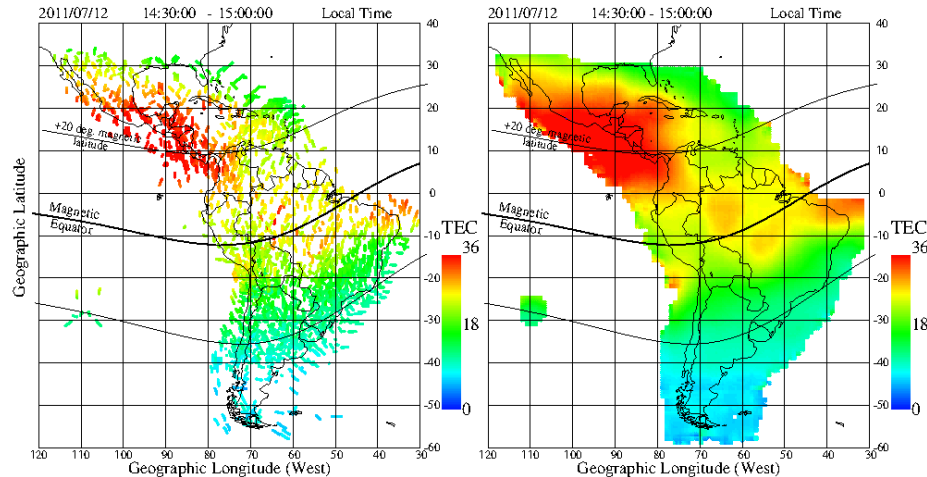


Figure 17. Measured Equivalent Vertical TEC from July 12, 2011 and TEC Resulting from an Interpolation and Fitting Procedure

The prominent feature in Figure 17 is the appearance of high TEC values over Central America and part of the Caribbean region. In fact, TEC values as high as 40 TEC units were observed in Central America between 1430 and 1500 local time compared to 25 TEC units over the magnetic equator. This localized TEC enhancement was observed over Central America mainly during the June solstice seasons. It is worth noting that, during the June solstice, the TEC values over South America are lower than other seasons due to the small amplitude of the equatorial vertical drifts that preclude a full development of the equatorial anomaly. These lower vertical drifts make the daytime equatorial F region hover at relatively low altitudes (<300 km).

Consequently, the low TEC values that were observed on July 12, 2011 are quite typical in the equatorial region. Nevertheless, it was unexpected to find the highest TEC values to reside over Central America and reaching over 20° of geographic latitude.

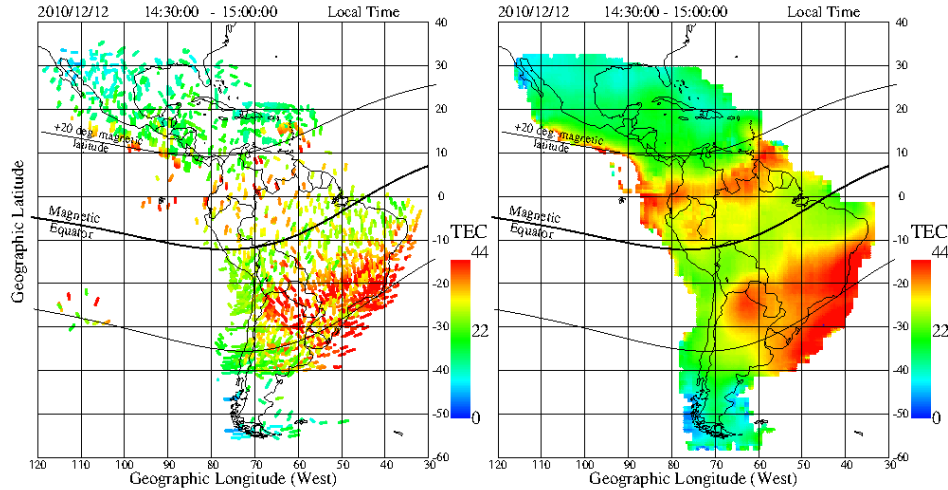


Figure 18. Measured Equivalent Vertical TEC from December 12, 2010 and TEC Resulting from an Interpolation and Fitting Procedure

During the December solstice the equatorial anomaly develops more fully than the June solstice due to the increased magnitude of the equatorial vertical drifts. Figure 18 shows a fully developed equatorial anomaly in which the northern and southern crests are placed $\sim 15^{\circ}$ away from magnetic equator. Close inspection of the southern crest of the equatorial anomaly indicates that there exists another region of high TEC values placed further south than the traditional equatorial anomaly. This enhanced region is also located near the boundary of the tropics at magnetic latitudes poleward of 20° and it is identified as the tropical ionization anomaly developing in the southern hemisphere. In this case, it develops during the December solstice. On some days the tropical ionization anomaly develops close to the southern crest of the equatorial anomaly giving the impression of one broad enhanced region. However, as discussed below, the physical mechanisms that produce the equatorial and tropical ionization anomalies are quite different.

Figure 19 displays a sequence of 12 TEC maps gathered between 12 and 23 LT on June 07, 2011 to show the initiation, lifespan and decay of the tropical ionization anomaly. The thick line crossing at the center of Peru, northern Bolivia and through Brazil indicates the location of the magnetic equator. Both thin lines, on each side of the magnetic equator, point out the locations where the magnetic latitude is 20° . Note the apparent poleward motion of the region of enhanced TEC values over Central America and its subsequent decay near sunset in the plot for 18 LT. A TEC enhancement starts building up near 12 LT; it is fully developed by 15 LT (~ 13 TEC units enhancement) and rapidly decays after 18 LT. Sometimes, as observed in this Figure, a small region of high TEC values drifts eastward and remains in the Caribbean region for a few hours. At 20 LT, the equatorial anomaly can be seen as two symmetric green traces near 12° magnetic latitude.

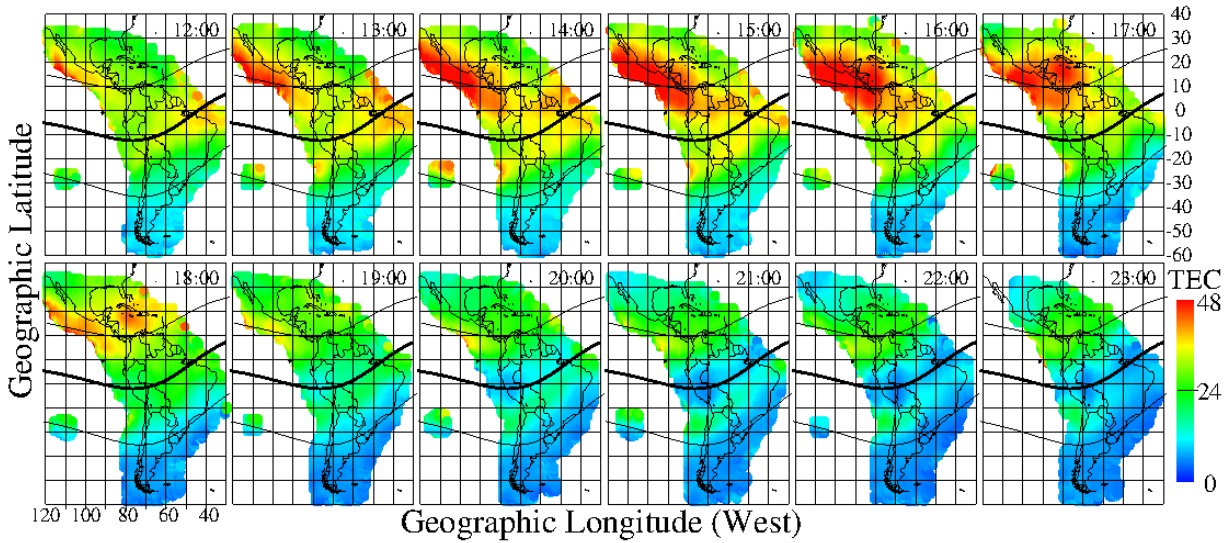


Figure 19. Temporal Evolution of TEC Observed on June 07, 2011 between 12 and 23 hours LT

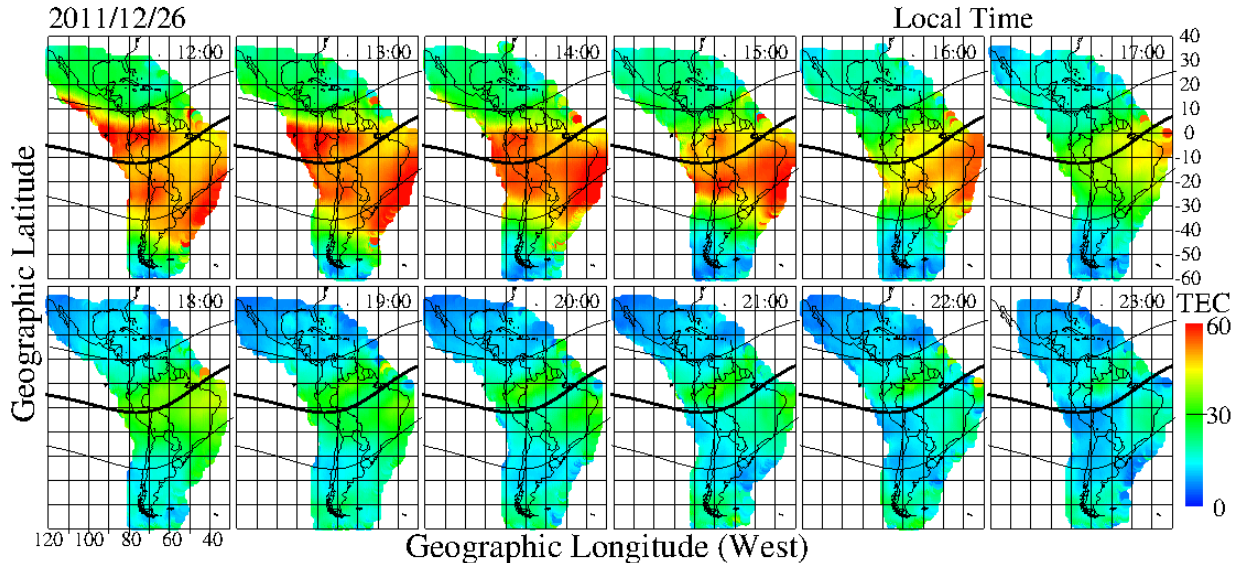


Figure 20. Temporal Evolution of TEC Values Observed on December 26, 2011 between 12 and 23 hours LT

Figure 20 exhibits the development of the southern crest of tropical ionization anomaly over the southern Coast of Brazil that occurred on December 26, 2011. At 12 LT the equatorial anomaly is fully grown, but confined only on the western side of South America. Both crests are symmetric and reside $\sim 15^\circ$ from the magnetic equator. The tropical ionization anomaly starts before 12 LT, and remains until 17 LT when both equatorial and tropical ionization anomalies seem to decay jointly. The TEC enhancement associated with the tropical ionization anomaly is ~ 15 TECu at 13 LT.

The important characteristics of the tropical ionization anomaly can be summarized as follows: The tropical ionization anomaly appears at latitudes poleward of 20° magnetic latitude, extends 10° or more in latitude, and 30° or more in longitude. During the June solstice, it

develops in Central America and its eastern end is at 70° W, where the magnetic declination of the Earth's B field becomes zero. During the December solstice, it grows near the southern coast of Brazil and ends at 60° W. There exists an "apparent" poleward motion of the tropical ionization anomaly. The anomaly rapidly decays before sunset. The amplitude of the TEC enhancement is between 12 and 20 TECu. The tropical ionization anomaly is symmetric: it develops over Central America during the local summer (June) solstice and in the southern east coast of South America during the local summer (December) solstice. It is worth noting that during the summer seasons, in these two regions there exist a larger reservoir of fresh plasma that can be carried by the neutral wind along and up the field lines.

These patterns of high TEC values observed near the boundary between the low and mid-latitudes are mainly restricted to the solstice months. However, on a few occasions, tropical ionization enhancements were observed during the months of April and September. It is suggested, and demonstrated below, that the appearance of the tropical ionization anomaly is produced by the zonal component of the wind system and the variation of the magnetic declination within the American sector (120°-40° W).

Modeling Tropical Ionization TEC Enhancements

To elucidate the role of the neutral wind on the formation of the tropical ionization anomaly, the Low-Latitude Ionosphere Sector (LLIONS) model was adapted to follow closely the unique geometry of the Earth's magnetic field that prevails in the American sector. LLIONS calculates the two-dimensional, time-dependent density distributions of five major plasma constituents (NO^+ , O_2^+ , H^+ , O^+ , e^-) between $\pm 45^\circ$ latitude and 90-4000 km altitude. The plasma distribution is solved along magnetic field lines with many field lines used to construct a regular output 2D grid in magnetic latitude and altitude. The output grid has a resolution of 2 degree magnetic latitude with an altitude resolution of ~ 4 km in the E-region and ~ 20 km in the F-region. A precise representation of the Earth's magnetic field was used to duplicate the effect of magnetic declination on the final distribution of the ionospheric density. LLIONS is a physics-based ionosphere model that provides a specification of the ionosphere along a magnetic surface extending in altitude and latitude and embedding several field lines in altitude. Regional or global modeling is obtained by conducting multiple runs of the LLIONS model for different longitudinal sectors. Inputs to the model are the vertical $E \times B$ drift velocities, horizontal neutral winds, the neutral atmospheric densities and temperatures, and the K_p and $f_{10.7}$ solar flux indices. The MSIS90 provides the neutral atmosphere parameters and the EUVAC photo-ionization model is used for ion production rates. The Titheridge plasma temperature model is used for electron and ion temperatures. The LLIONS code solves for ion chemistry, field-line diffusion with ambipolar electric fields, neutral wind forcing along field lines, and $E \times B$ drift motion of the field lines. The model output includes electron and ion density and temperatures with utilities to calculate TEC, $N_m F_2$ and $h_m F_2$ values.

Two key observational characteristics of the tropical ionization TEC enhancements guided the numerical simulations. First, the enhancements associated with the tropical ionization anomaly were only seen during the afternoon hours, and terminated abruptly near 18 LT. During this time interval the zonal wind is directed toward the west reversing rapidly near 18 LT. This fact suggests that a westward wind may be a necessary condition for the development of the TEC enhancements. Secondly, during the June solstice the tropical ionization anomaly was observed in Central America, a region of eastward magnetic declination and during the December solstice in the eastern-southern part of Brazil, an area of westward declination. In these two regions, the

westward wind is able to carry the ionospheric plasma toward the equator along the field lines displacing the plasma to higher altitudes, where plasma recombination becomes slower. Due to the dominant and important role of the east-west wind, it was decided to increase the magnitude of the zonal wind by doubling the value provided by Hedin's wind model (HWM). It is also noted that the tropical ionization anomaly occurred during the solstices and within regions where the north-south component of the neutral wind can blow plasma up the field lines over Central America during the June solstice and over Southern Brazil during the December solstice. A precise representation of the Earth's magnetic field was introduced into LLIONS using the International Geomagnetic Reference Field (IGRF) model for each longitude sector. At each instant of the model simulation, the neutral wind along the field lines was recalculated using the north-south and east-west winds provided by the HWM model.

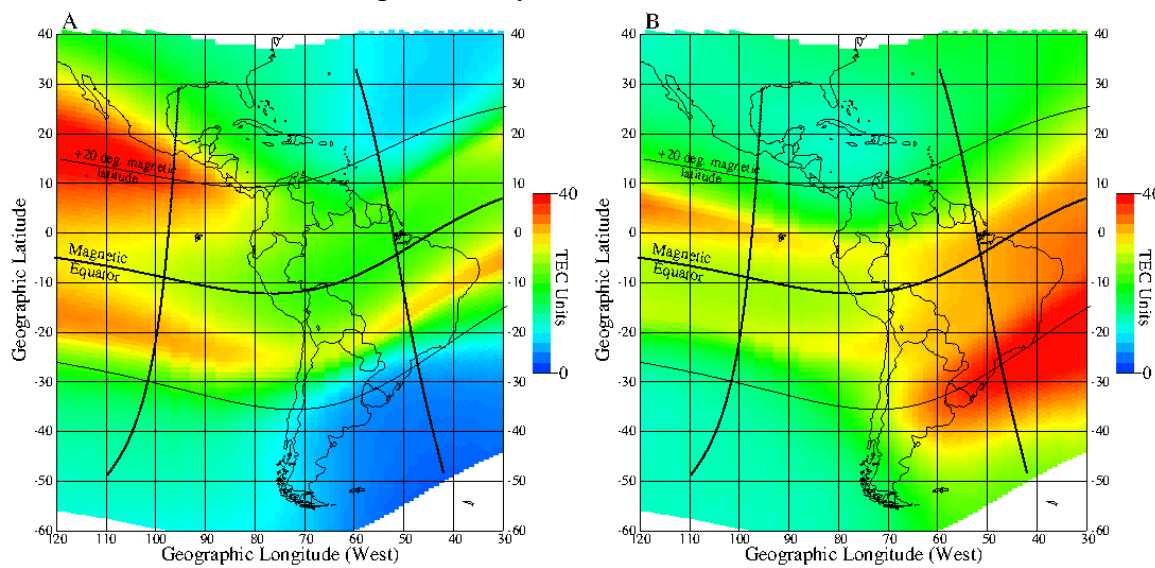


Figure 21. Computer Simulation of the Tropical Anomaly Conducted using the LLIONS Model

Figure 21 presents TEC results of the LLIONS model for 2 periods, one corresponding to the middle of the June solstice (left panel) and the other for the December solstice (right panel). Local times for both frames were selected at 15 hours. It is evident that during the June solstice (left frame), a region of high TEC value develops at latitudes north of 20° and over Central America. Another enhancement is observed over the southern Coast of Brazil, where the magnetic latitude is poleward of -20° . Both structures are in temporal and spatial agreement with the characteristics of the tropical ionization anomaly presented in Figures 1 and 2. The simulations conducted here offer a “proof of concept” that the westward wind provided by the HWM model and the peculiar geometry of the magnetic field in South and Central America can create a region of distinct and anomalously enhanced TEC and plasma density distributions. Certainly, a larger westward wind will displace the plasma further equatorward, increasing the tropical ionization anomaly and augmenting its latitudinal extension.

Conclusions.

TEC values observed over South and Central America and the Caribbean region have shown the unique morphological characteristics of anomalous plasma enhancements that develop over Central America during the June solstice and over the southern part of Brazil during the December solstice seasons. These two anomalous TEC enhancements should be considered as

one type of structure as the physical mechanism that originates them is fundamentally the same. It is postulated and demonstrated by using numerical simulations, that the neutral wind, both the north-south and the east-west components, under the peculiar geometry of the magnetic declination across the South American continent acts accordingly to transport the plasma along the field lines and toward higher altitudes during the afternoon hours. It is known that when the F-region plasma resides at high altitudes the recombination rate slows down, producing an accumulation of plasma density. When the zonal wind reverses direction and starts moving eastward, the tropical ionization anomaly plasma is carried toward lower altitudes, rapidly accelerating its decay and its consequent disappearance. The marked seasonal/longitudinal variability of the tropical ionization anomaly is produced by the strong variability of the background TEC between hemispheres at different seasons. Figure 17 and 18, and also the numerical simulations of Figure 21, display low TEC values over the southern coast of South America in the June solstice and low TEC over Central America during the December solstice. The apparent poleward motion of the tropical ionization TEC enhancements is produced by the continuous accumulation of plasma, increasing the volume of the TEC enhanced region and extending this to higher latitudes as time progresses. The actual plasma motion is toward the equator.

The observations presented here correspond to quiet conditions when neither prompt penetration electric fields nor a super fountain effect are active. In addition, the tropical ionization anomaly occurs mainly during the solstices when the wind system is preferentially trans-equatorial. It is worth to note that several morphological features of the tropical ionization anomaly cannot be explained by the super-fountain effect, among them: (1) the sharp termination of the tropical ionization anomaly where the declination reverses, (2) its rapid decline at ~ 17 LT, (3) its seasonality, and (4) the pronounced inter-hemisphere symmetry of the TEC enhancements. LLIONS results corroborate the key role of the neutral wind and the unique characteristics of the Earth's magnetic field in the American sector on transporting the plasma toward higher altitudes and creating regions of higher density/TEC values. This close association between zonal winds and TEC enhancements opens the possibility of using density or TEC measurements and an assimilation first-principle model to calculate the magnitude and direction of the wind in the region of the tropical ionization anomaly.

3.1.6 Polar Cap Patches Observed During the Magnetic Storm of November 2003. Multi-instrumented measurements of polar cap patches were conducted early during the recovery phase of the major magnetic storm of November 20, 2003 using the Qaanaaq imager and digisonde, the Sondrestrom incoherent scatter radar (ISR), the SuperDARN radars and the DMSP-F13 satellite. A 2D cross-correlation analysis was applied to series of two consecutive red-line images indicating that the magnitude and direction of the patch velocities were in good agreement with the SuperDARN convection patterns. A back-tracing analysis to the patch locations indicated that most of the patches seen between 2041, and 2129 UT were likely transiting the throat region near 1941 UT. Inspection of the SuperDARN velocities at this time indicates spatial and temporal collocation of a gap region between patches and large (1.7 km/s) line-of-sight velocities. The variable airglow brightness of the patches observed between 2033 and 2043 UT was investigated using the numerical Global Theoretical Ionospheric Model (GTIM) driven by the SuperDARN convection patterns and a variable upward/downward neutral wind. The numerical results indicate that variations in the airglow intensity up to 265 Rayleighs can be produced by a constant 70 m/s downward vertical wind.

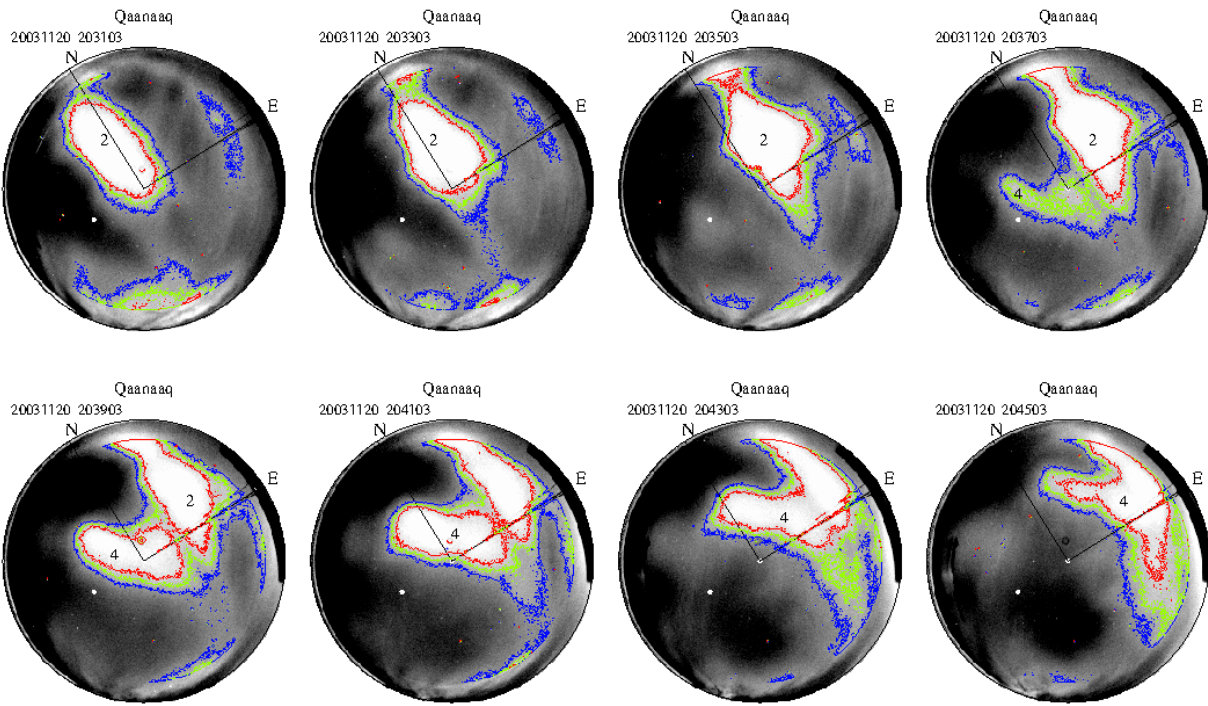


Figure 22. Sequence of Images from Qaanaaq between 2031 and 2053 UT during the Recovery Phase of the Magnetic Storm of November 20, 2003

Each of the 630.0 nm images of Figure 22 was processed by removing the average value of all pixels within the imager field of view and normalizing the intensity with respect to the image standard deviation (σ). To avoid systematic effects a constant σ value equal to 80 Rayleighs was employed to normalize the images presented in Figure 22. Three contour levels serve to indicate the locations where airglow intensities reach the relative levels of 50 R (blue), 80 R (green), and 110 R (red) values. Note also that the contour levels have been restricted to elevations larger than 20° . The image sequence of Figure 22 shows several polar cap patches with atypical morphological characteristics. It displays the “appearance” of new patches, and sudden changes of the patch brightness that have never been reported before. This image shows a small patch (labeled 2) placed at the northern side. Images recorded between 2031 and 2047 UT display the growth, brightening and exit of patch 2 as it transits across the imager field of view. As time progresses, patch 2 is seen to extend further south and occupy a much larger area (2035 UT), then move continuously toward the east, and reach the eastern edge of the imager (2047 UT). It is important to note, as it is demonstrated below, that during this time the SuperDARN convection velocity was directed antisunward (eastward). Nevertheless, patch 2 “growth” was in the southward direction. The images of 2037:03 and 2039:03 UT show the appearance and brightening of a “new” patch (labeled 4) that intensifies near the western side of the patch that developed minutes before. It is shown below that the patch brightening is produced by a lowering of the F-layer due to the downward wind associated with a large scale TID.

Figure 23 shows density contours measured with the Sondrestrom radar projected to a ground plane. The contours corresponding to 5×10^5 and 10^6 cm^{-3} indicate that the radar bisected

the patch, measuring the cross section of a long and east-west elongated patch. This Figure also shows the ground projection (green line with dots) of the 300 and 500 km constant altitude for both scans. Figure 23 also includes the 630.0 nm emissions measured by the Qaanaaq imager, and the DMSP-F13 satellite trajectory (red line) mapped along the B lines from 850 km altitude to the F region and then projected to the ground plane. The right panel shows in-situ densities measured by the DMSP satellite and plotted according to the satellite trajectory as the satellite moved along in the geographic plot. Four density enhancements are displayed in the right frame clearly corresponding to the ISR density and airglow enhancements that were observed at Sondrestrom and Qaanaaq respectively. Notice that the DMSP intersected the Sondrestrom east scan at 2006 UT and later the Qaanaaq imager at 2008 UT. It is evident that the first patch detected by DMSP-F13 at 2006:10 UT corresponds to the density enhancement observed 350 km north and during the radar scan of 2008:57 UT. The DMSP density enhancement at 2007:20 UT is probably related to the density enhancement seen 700 km north of the radar site. And, the long density enhancement of 2008:30 UT is associated with the airglow enhancement seen by the imager. A fourth patch detected by the DMSP satellite was almost outside and northward of the field-of-view of the Qaanaaq imager.

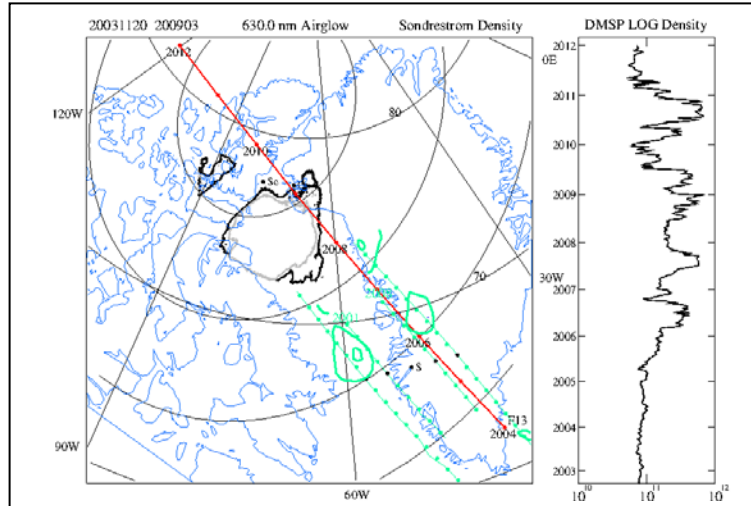


Figure 23. 630.0 nm Airglow Emissions from Qaanaaq Observed at 2009 UT on November 20, 2003 Projected to 250 km Altitude

Analysis of Patch Drift Velocities

This analysis uses images separated by 2 minutes to avoid drastic changes in the airglow view of the patches that may be occurring due to large-scale instability processes, or variations in the altitude of the F region. The method consists of a 2-D cross-correlation algorithm using the image intensities of an area equal to 32×32 pixels and correlates these values with the intensities of an identical region in the image gathered 2 minutes earlier. The full cross-correlation function is obtained by sliding the grid of one image in x and y with respect to the other. The patch velocity is directly proportional to the displacement that has the largest cross-correlation factor. We selected a grid size smaller than the typical patch extension to allow for multiple drift vector estimations within a single patch. The main requirement of this method is that the spatial gradients and the boundaries of the polar cap patches remain coherent between consecutive images. We have also restricted the patch drift calculations for areas above 30° elevation and

consider a reliable estimation of the patch drift velocity when the correlation factor is above 0.95. Figure 24 shows the 630.0 nm image (blue contours) and the patch drifts (red vectors) corresponding to 2037:03 UT displayed in a geographic (left panel) and Corrected Geomagnetic coordinate systems (right panel). The left frame shows the patch velocity vectors directed eastward that become nearly antisunward in a CG coordinate system. The average magnitude of the vector amplitudes is ~ 630 m/s (statistical uncertainty = ± 94 m/s). This frame also includes the SuperDARN potential pattern (black and gray contours) corresponding to 2030 UT and for latitudes poleward of 80° . It is worth mentioning that during the period analyzed here (20-24 UT) of the super-storm of November 20, 2003, plasma structuring within the polar cap was abundant, making it possible for the SuperDARN radars to have numerous measurements of line-of-sight velocity, especially on the dusk side of the polar cap. Close comparison between the patch vectors and the SuperDARN flows indicate an average difference of 87 m/s for the magnitude of the velocities and a 30° average angle difference.

Figure 25 shows the results of a trajectory analysis in which the images of 2041:03 (red), 2101:03 (blue), and 2129:03 UT (green), are used to define the patch boundaries. The top (lower) frames of Figure 25 show the back-traced location of the patches at two instances separated by ten minutes displayed in a Corrected Geomagnetic (geographic) coordinate system. The “red” and “blue” patches delineate regions where the number density is higher than the background polar cap density. The shape of these two patches suggests that they have been part of a much larger entity that was probably “broken up” by a formation mechanism. The location of the patches in the convection pattern of Figure 25 suggests that they originated from the high latitude afternoon sector and were transiting the throat region (above Hudson Bay, Canada) between 1941 and 1951 UT.

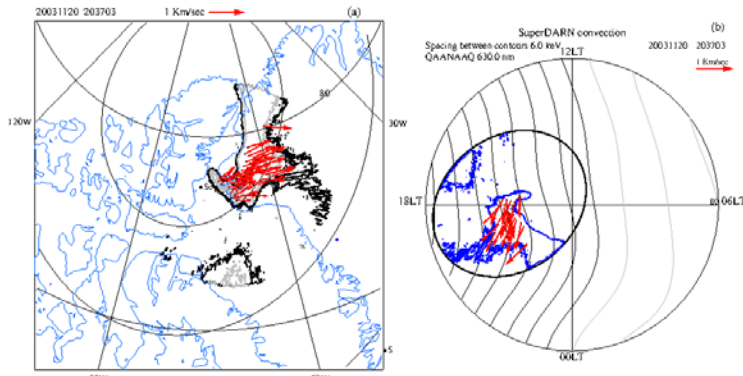


Figure 24. Airglow Images and Vectors of the Patch Drift Velocities Plotted in a Geographic Frame and CG Polar Plot

The velocity measured by the Kapuskasing radar for the periods of 1940–1941 and 1942–1943 UT on November 20, 2003 indicate the presence of velocities directed poleward (antisunward) at all locations over Hudson Bay. The important feature of these two plots is the small region of enhanced velocities (1.7 km/s, green pixels) seen near the center of the radar scan. The left frame shows the enhanced velocity to be below 70° , and to be in close proximity with the location of the gap that is observed between the red and blue patches in the lower frames of Figure 25.

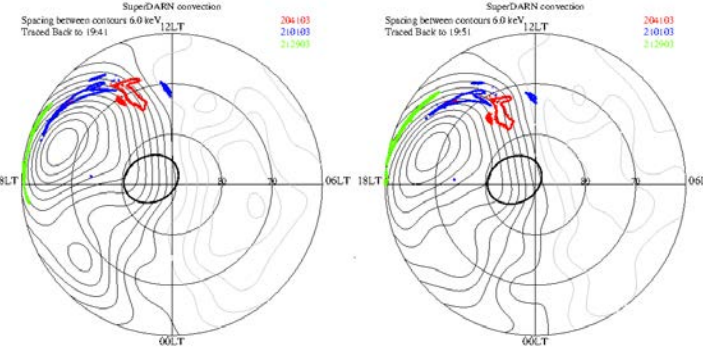


Figure 25. Trajectory Analysis of the Patches Observed at Qaanaaq on November 20, 2003 at 2041, 2101, and 2129 UT

Modeling of Patch Brightness

The high latitude GTIM model is a 1-D ionospheric model that calculates the ion density by numerically solving the time-dependent O^+ continuity equation along a fluxtube. However, the model can attain a 3 dimensionality by repeating the calculations along several fluxtube. GTIM includes the effect of ionization by solar EUV radiation and electron precipitation, loss through charge exchange with N_2 and O_2 , transport by diffusion, neutral winds, and $E \times B$ convection drifts. The MSIS and Hedin's wind models supply neutral densities and winds, respectively; and an option to specify a value for the vertical wind was added to see its effect on density profiles. We also modified the GTIM model by including a parameterized model of soft electron precipitation, a calculation of the $E \times B$ plasma drift based upon the SuperDARN convection patterns, and a first-order approximation of the NO^+ density based on chemical equilibrium.

We modeled the ionospheric density along flux tubes that transited over Qaanaaq between 20 and 21 UT on November 20, 2003. The simulation was initiated by tracing backward in time these flux tubes until they were passing over the dayside throat region. At these locations, densities along the flux tubes were made equal to the density profile measured by the Millstone Hill (53° CGLAT) radar. The model proceeds by conducting a full solution of the GTIM model along a forward tracing of the convection path. Although the path calculation is restricted to the limits of the SuperDARN data (60° - 90° CGLAT), this initial profile is probably a reasonable one given the overall magnetic storm condition and the fact that we are not trying to closely reproduce the densities observed at Qaanaaq, but to study the effect that a vertical wind makes on the emission rates associated with polar cap patch densities. However, we noticed that doubling the amount of atomic oxygen provided by the MSIS model increased the F-region peak altitude to values closer to the values measured by the Qaanaaq digisonde. To assess the effect of a burst of vertical wind, we introduced a nominal 70 m/s downward vertical wind that lasts between 2010 and 2030 UT. This wind produces a downward component parallel to the nearly vertical magnetic field lines and causes the peak altitude to descend few tens of kilometers. We also noticed that the number density at 300 km altitude increased from 2×10^4 to 2×10^5 cm^{-3} and the shape of the F-region bottomside varied when the vertical wind was applied. The new density profiles over Qaanaaq were used to estimate the 630.0 nm column emission rate, J_{6300} , in Rayleighs due to dissociative recombination using the expression (10).

$$J_{6300} = \int \frac{A_{6300} \gamma_1 n(O_2) n(O^+) dz}{A(1 + d(z)/A)} \quad (10)$$

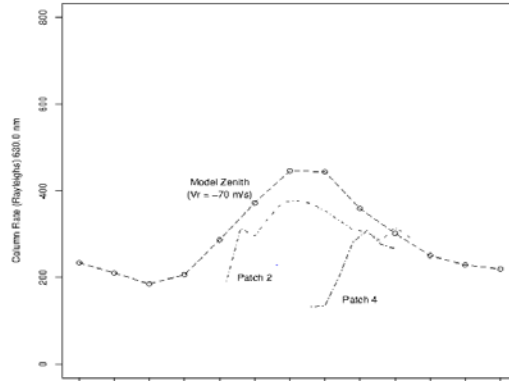
Where γ_1 is the O^+ and O_2 rate coefficient, A is the radiative transition coefficient for the 1D term, and $d(z)$ is the quenching frequency given by:

$$d(z) = S_{N_2} n(N_2) + S_e n(e) \quad (11)$$

S_{N_2} and S_e are the quenching coefficients for quenching on N_2 and electrons, respectively.

The dashed line of Figure 26 shows the count rate as a function of time calculated using expressions (10) and 11). A maximum increase equal to 260 Rayleighs was obtained during the simulations. Figure 26 also shows the relative brightness of patches 2 and 4 (see Figure 22) as they transited across the imager field of view. It is observed that the patch 2 brightened by ~ 200 Rayleighs and patch 4 located further sunward (westward in geographic coordinates), increased by 170 Rayleighs.

To strengthen our claim on the presence of a downward motion of the ionosphere, we present Figure 27 that shows the line-of-sight (LOS) velocities measured by the Sondrestrom ISR on November 20, 2003 when the radar was pointing along the magnetic field (up B). This Figure displays alternating bands of upward (red) and downward drift velocities (blue) with a 40-60 min periodicity. Plasma drifts reaching values up to ± 50 m/s were observed between 1950 and 2300 UT. It is well known that when the ISR antenna is pointed parallel to B, the radar is able to measure the magnitude of the component of the neutral winds along the magnetic field. We suggest that the upward, and then downward neutral wind motions are due to the passage of a train of large-scale gravity waves.



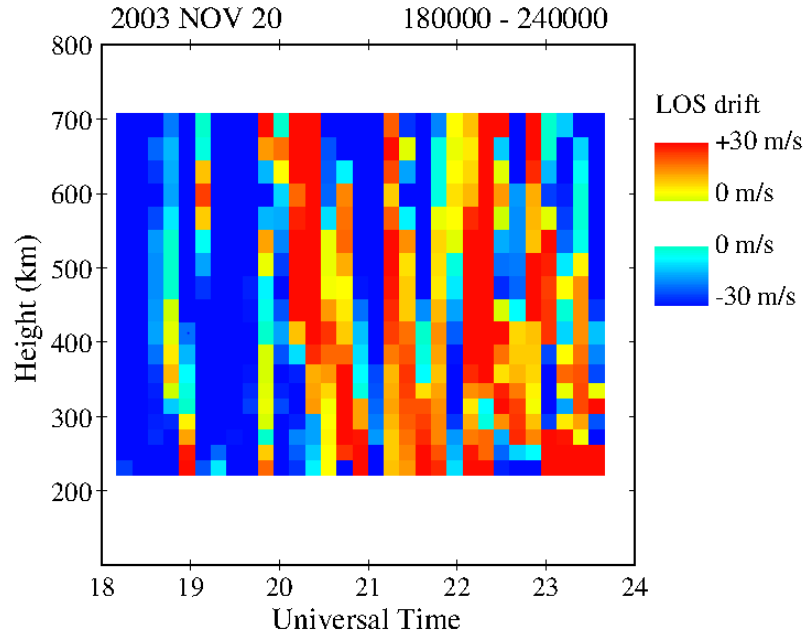


Figure 27. Line-of-Sight Velocities Measured by the Sondrestrom Radar on November 20, 2003

Conclusions.

The following lists the main conclusions of this research:

- (1) The polar cap patches observed during the recovery phase of the large geomagnetic storm of November 20, 2003 showed that their 630.0 nm airglow intensities can vary as much as 250 Rayleighs as they transit across the imager field of view. We used the GTIM model to investigate whether a downward neutral wind associated with a train of large-scale gravity waves could be responsible for the variable intensity of the 630.0 nm airglow emissions.
- (2) The GTIM code was modified to accept Super DARN derived polar convection patterns and a variable value of the vertical component of the thermospheric wind. We were able to calculate that a 70 m/s downward vertical wind acting on the same field line for 20 min could produce an increase of 250 Rayleighs in the 630.0 nm airglow emissions.
- (3) The development of a back-tracing trajectory analysis algorithm allowed us to investigate the origin of the polar cap patches. We concluded that during the interval under study, most of the patches entered the polar cap from the afternoon sector.
- (4) Continuous measurements conducted by the Kapuskasing SuperDARN radar provided evidence for the presence of enhanced velocities (>1.7 km/s), on November 20, 2003. The use of a tracing algorithm able to step backwards in time permits us to examine the ionospheric condition when the patches were in the dayside region. This algorithm can be applied to other patch events to study the formation mechanism of polar cap patches when the ionosphere is in a non-storm condition.

(5) A method to calculate plasma drift velocity that uses a 2-D cross correlation algorithm has been developed based on the property of the patches to drift with the background polar cap convection. We used the Super DARN polar convection to validate our drift results.

3.2 Analysis, Modeling and Simulation of Scintillation Effects on DoD Systems

3.2.1 Simulating the Impacts of Scintillation on Radar. The effects of the ionosphere on a space radar system can be categorized into two basic types. The first type consists of effects caused by the ionospheric background such as refraction, polarization rotation, group delay, and phase advance. These effects can be largely mitigated if a suitable model for the background ionosphere is employed during radar processing or, better still, if the radar itself can measure Faraday rotation [Roth et al., 2010]. The second type consists of effects caused by small-scale ionospheric structures (on the order of the Fresnel scale) which cause scintillation of the radar radio wave. These small-scale structures are generated by plasma instability processes which act predominantly in the polar cap and equatorial zone at night, the effects being more pronounced during periods of high solar activity [Aarons, 1982]. As radio waves traverse these small-scale structures, they scatter randomly in different directions and travel paths of different distances, resulting in spatial variations in signal phase. These phase variations cause mutual-interference as the radio wave propagates past the ionosphere through free-space causing a diffraction pattern on the ground with spatial variations in both amplitude and phase. These signal fluctuations are intensified as the reflected wave traverses the ionosphere a second time during the return path to the space radar. Ionospheric effects increase dramatically as the operating frequency of the radar decreases, such that the impacts can be performance limiting for radars operating at L band and lower frequencies [Chapin et al., 2006]. Amplitude and phase fluctuations which decorrelate across the synthetic aperture of the radar reduce the effective resolution of a SAR image [Xu et al., 2004], and alter critical differential phase relationships between images collected during satellite revisits that are required by InSar and change detection applications.

Simulating Scintillation Effects on Tracking and Foliage Penetrating (FOPEN) Radars

Beginning in 2005, the Air Force Research Laboratory (AFRL) has carried out experiments designed to mitigate the effects of the ionosphere on wideband systems dependent on radio wave propagation through the ionosphere with ALTAIR, a two-frequency (VHF/UHF) tracking radar located at the Ronald Reagan Ballistic Missile Defense Test Site on Kwajalein Atoll. The joint U.S.-UK effort, known as the Wideband Ionospheric Distortion Experiment (WIDE), makes use of data from ALTAIR tracking scans of calibration spheres with diameters ranging from approximately 0.4 to 1.1 m in low-Earth orbit (LEO). Since the radar transmits at two-frequencies, its differential phase measurements can be used to infer the total electron content between the radar and the calibration sphere being tracked. We make use of the phase-derived total electron content (TEC) from ALTAIR tracking scans to construct a phase screen through which we can simulate the propagation of a radio wave, and compare the results with the actual radar returns. Of course ALTAIR is a tracking radar, not a foliage penetrating radar, but both systems operate in the UHF frequency range where ionospheric effects are similar. As such these simulations are also useful for assessing the impact of scintillation on FOPEN radar systems.

The application of the phase screen technique to the propagation of electromagnetic waves through random media was originally developed by Ratcliffe [1956] as a solution to the

parabolic wave equation. The technique assumes that the infinitesimally thin screen imposes only a phase perturbation on the wave as it crosses the screen. For propagation through the ionosphere, this phase perturbation is proportional to the integral of the electron density fluctuations, or the TEC variation ΔN_T , along the radar line of sight:

$$\varphi(z) = -\lambda r_e \Delta N_T \quad [12]$$

where r_e is the classical electron radius and λ is the radio wave frequency. The complex wave amplitude $A(x, z)$ obtained on a ground-based receiver, a distance z from the phase screen, for a one-way satellite link, typical of communication and navigation systems, results from the calculation of Fresnel diffraction under the assumption of forward scattering [Beach et al., 2004]:

$$A(x, z) = \frac{1}{r_F} \int_{-\infty}^{\infty} A_0(x') \exp \left[i\pi \frac{(x-x')^2}{r_F^2} \right] dx' \quad [13]$$

where $r_F = (\lambda z)^{1/2}$ is the Fresnel radius and $A_0(x) = \exp(i\phi)$ is the complex amplitude of the plane wave directly below the phase screen. The advantage of the phase screen technique is that the method applies in both the weak and strong scattering regimes. One limitation of this technique is the assumption of variation in the screen in only one direction, in other words; we are using a 1-D phase screen.

Utilizing these modeling tools with space surveillance radars requires extending the phase screen technique to account for two-way propagation of the transmitted wave to a space-based target and back to the receiver. Because the wave moves at the speed of light, for ranges to objects in Earth-centered orbits, the transmitted and scattered waves can be assumed to propagate through the same ionospheric channel for a monostatic radar system using the same antenna for transmission and reception. In other words, the medium is assumed frozen during the time the radar wave propagates through it in both directions. We have developed a technique for determining the scintillation effects on the radar pulse by dividing the two-way propagation problem into four parts. The first part involves the propagation of the transmitted wave through the phase screen to the target. We can solve for the complex amplitude of the transmitted pulse using the Fresnel diffraction formula as in the one-way case with the propagation distance selected as the range between the phase screen and the target center. The second part concerns the interactions between the resident space object (in our case, a calibration sphere) and the radar pulse arriving at the target to produce the scattered wave. For the current example, we assume that the target is a frequency-flat point scatterer with unity reflectivity located at a horizontal distance x_1 [Knepp and Brown, 1997]. Under this assumption, the complex amplitude of the scattered wave $A_s(x, z)$ becomes

$$A_s(x, z) = A(x, z) \delta(x - x_1) \quad [14]$$

where $\delta(x)$ is the Kronecker delta function. The third part of the problem involves the propagation of the scattered wave from the target to the phase screen. Because the simple target model only selects one horizontal component, this step is trivial to implement. The last part is to determine the effects of Fresnel diffraction caused by the phase screen as the scattered wave, $A_s(x, z)$, propagates back to the receiver.

Results from this two-way radar propagation tool are shown in Figure 28, where we display data from a tracking scan of RIGIDSPHERE-2 (LCS-4, object ID 05398) on 5 October 2006 (DOY 278). The observed and simulated RCS from ALTAIR returns during this scan are shown for VHF and UHF, respectively, in plots a) and b). Also shown for comparison is the simulated and observed 10 second S_4 (bottom). The phase-derived TEC was used as input to the two-way phase screen model along with the effective scan velocity of the radar across the observed irregularities (more specifically, the velocity component perpendicular to the local magnetic field and in the plane of the screen). While the simulated RCS does not provide a one-to-one correspondence with the observed RCS, the statistics of the fluctuations in both time series do match each other quite well, as can be seen in the two-way S_4 scintillation index comparison.

Structured ionospheric irregularities over Roi-Namur on this evening resulted in a scan in which the radar beam passes in and out of disturbed regions. As described by Fremouw and Ishimaru [1992] and observed by Knepp and Houpis [1991], the RCS on monostatic paths can be enhanced, as well as diminished, in the presence of scintillation due to backscatter. Evidence of the RCS enhancement is seen in the VHF and UHF ALTAIR observations presented in Figure 28 (top) where the RCS fluctuates significantly near the beginning and end of the tracking measurement. The RCS fluctuations are much smaller while the radar scans between the two discretely spaced ionospheric irregularity structures.

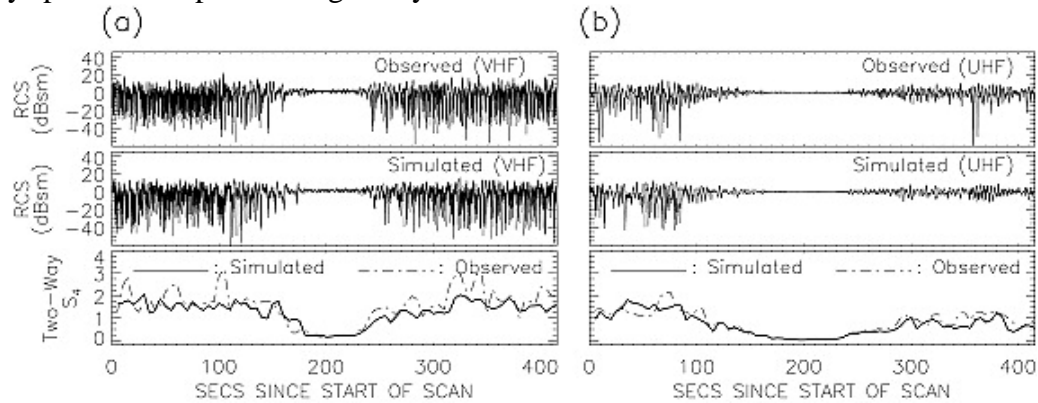


Figure 28. ALTAIR Observations and Phase Screen Simulations of Radar RCS for a Tracking Scan of RIGIDSPHERE-2 on 5 October 2006 Beginning at 1020:45 UTC

We conducted phase screen simulations of other ALTAIR radar scans as well. The validation results for these examples are described in [Caton et al., 2009].

Simulating Scintillation Effects on Synthetic Aperture Radar

We analyzed SAR data collected by the Phased Array type L-band Synthetic Aperture Radar (PALSAR) on board the Japanese Advanced Land Observation Satellite (ALOS). Due to its operating frequency in the L band (1270 MHz) where ionospheric effects are important, a wide variety of ionospheric effects on PALSAR images have been reported in the literature [e.g. Pi et al., 2011 and the references therein]. We are principally concerned with the impacts due to scintillation, which are manifest in ALOS/PALSAR images of low latitude terrain as streaks that appear to be approximately aligned with the magnetic field [Shimada et al., 2008].

To assess the impact of ionospheric scintillation on SAR image formation and interferometry we developed a new phase screen model called the SAR Scintillation Simulator (SAR-SS). This simulator consists of a phase screen generator and a radio-wave propagator. The

screen generator creates a 2D random realization of spatial phase fluctuations resulting from the traversal of small-scale irregularities in the ionosphere. The irregularities are specified statistically in terms of a power spectral density that depends on 1) the vertically integrated strength of turbulence, 2) the phase spectral index, 3) the outer scale, and 4) the anisotropy ratio of the irregularities along and transverse to the local magnetic field direction. The screen generator accounts for the motion of the radar platform, the drift of the ionospheric irregularities, and the oblique angle of propagation, all of which determine the scale sizes of the irregularities sampled by the radar beam. The statistical parameters specifying the irregularities can be input to the simulator manually, or provided by the Wideband ionospheric scintillation model (WBMOD), a global climatological model of scintillation constructed from an extensive database of observations [Secan et al., 1995].

The propagator of the SAR-SS model solves the 3D parabolic wave equation (PWE) using the split-step technique [Rino, 2011] to compute the transfer function for two-way propagation through the ionosphere. This transfer function is used to modulate the SAR signal due to terrestrial features in order to assess the ionospheric impact on SAR image formation. We note that SAR-SS is similar to an existing phase screen model called SAR-TIRPS [Rogers and Cannon, 2009], except that the later was constructed using a 1D phase screen. The SAR-SS model uses a 2D phase screen, which is necessary for simulating SAR images in the general case where the radar propagation path intersects the magnetic field direction at arbitrary angles.

To demonstrate the technique, we begin by showing examples of PALSAR imagery during two revisits of the ALOS satellite over the same terrain in Brazil. Figure 29 shows a PALSAR sub-look image of a scene in Brazil on 25 December 2007 at 03:20 UT during quiet ionospheric conditions. Figure 30 (left) shows a sub-look image of the same terrain on 26 March 2008 at 03:19 UT when the ionosphere was disturbed. The local time for these passes is 22:48 LT, which is after local sunset. Note the prominent streaks in the 26 March image oriented along the direction of the horizontal magnetic field, which is indicated by the arrow. These streaks are inclined at -5.7° from the radar along-track direction, which is the radar magnetic heading at this location.

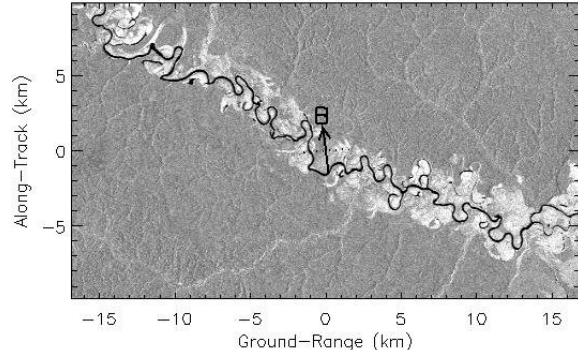


Figure 29. Observed PALSAR Image for 25 December 2007 at 03:20:30 UT during Quiet Ionospheric Conditions

We applied the SAR-SS model to the PALSAR data on 25 December 2007 by calculating the ionospheric transfer function based on the radar location and magnetic field parameters at the ionospheric penetration point (IPP), and then modulating the SAR signal to account for two-way propagation through the disturbed ionosphere. The resulting image is shown in **Figure 30** (right). The following radar and geophysical parameters were used in the simulation: pulse repetition frequency 2.1413275 kHz, pulse sampling frequency 32 MHz, off-nadir angle 34.3° , radar

heading 348° , magnetic declination -5.7° , and magnetic inclination 14.4° . The parameters specifying the ionospheric screen used were: turbulent strength $CkL=1.25 \times 10^{35}$, outer scale $L_0=5$ km, phase spectral index $p=9.0$, screen altitude 350 km, and anisotropy ratio $a:b=50:1$. The drift velocity of the plasma is small relative to the IPP velocity for a satellite in LEO orbit and has been neglected. The similarity between the observed and simulated PALSAR images suggests the SAR-SS model can reproduce the field-aligned streaks in PALSAR images caused by small-scale structure in the equatorial ionosphere.

The full details of this study have been published in [Carrano, et al. 2012a].

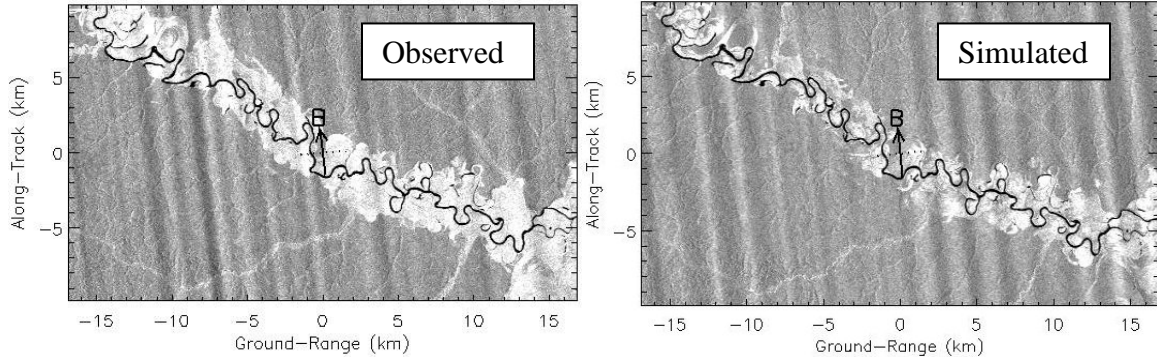


Figure 30. Observed and Simulated PALSAR Images for 26 March 2008 at 03:19 UT

Conclusions

We have developed and validated phase screen techniques to model the effects of ionospheric scintillation on tracking / FOPEN radars and synthetic aperture radars (SAR). To simulate scintillation impacts on tracking / FOPEN radars, we used 1D phase screens inferred from TEC measurements obtained from VHF/UHF ALTAIR observations of calibration spheres in low Earth orbit. In principle, any source of TEC measurements (such as that provided by GPS) may be used to specify the phase screen to simulate the RCS fluctuations caused by scintillation. To simulate scintillation impacts on SAR, we used 2D stochastic phase screens with parameters adjusted manually to reproduce the field-aligned streaks observed in affected SAR images. In both cases, we obtained excellent agreement between observed and simulated scintillation impacts.

3.2.2 Importance of Decorrelation Time for Modeling Scintillation Impacts on GPS.

Rapid fluctuations in the amplitude and phase (scintillation) of the GPS satellite signals caused by scattering from ionospheric irregularities can degrade GPS performance in a number of ways. Severe scintillations may result in loss of lock on the satellite signals, and even when lock is maintained, they may cause errors decoding the GPS data messages and corrupt estimation of the ranges to the GPS satellites. Several previous attempts to model the effects of ionospheric scattering on GPS performance have focused on the depth of signal fading, as quantified by the S_4 index, as the appropriate parameterization to use for the ionospheric perturbation of the signal [Datta-Barua et al., 2003; Carrano et al., 2005; Akala et al., 2012]. The S_4 index may not always be the best parameter for this purpose, however, because it is limited in several respects. Firstly, the S_4 index is independent of the rate of signal fading which has a direct impact on the stress of the GPS tracking loops. Secondly, under strong scattering conditions the S_4 index saturates to a value near unity, irrespective of the strength of the ionospheric perturbation. On the other hand, the decorrelation time characterizes the rate of signal fading and continues to vary with the

strength of the ionospheric perturbation once when the S_4 index has saturated [Carrano et al., 2010].

The Air Force Research laboratory conducted a campaign to monitor GPS scintillations at Ascension Island during the solar maximum period 5-19 March 2002. One of the several GPS receivers operated during the campaign was an Ashtech Z-XII survey grade model with a choke ring antenna. This receiver reported samples of C/No and carrier phase for the L1 and L2 carrier signals at 20 Hz. Intense scintillation activity ($S_4 \sim 1$) was encountered on all nights except one (March 6 was quiet), and severe impacts to GPS tracking performance and positioning accuracy were observed.

The S_4 index is directly related to the probability that signal fades will reach a particular level [Basu et al., 1987]. Loss of lock is more likely to occur when the GPS signal level drops below the fade margin of the receiver's internal tracking loops. Therefore, it is not surprising that the S_4 index is closely related to the probability of losing lock. Figure 31 (left) shows a scatter plot of S_4 versus time for all GPS satellites in view above 30° for all nights of the campaign. On average, the scintillation activity began approximately 1.5 hours after local sunset, and persisted for about 5-6 hours (roughly until local midnight). The data samples in the plot are colored red if a loss of lock event occurred and green otherwise. It is clear from the figure that the density of loss of lock events increases with increasing S_4 . Figure 31 (right) shows the likelihood that the error in the horizontal position reported by the receiver reached a particular level. For example, the error in horizontal position error was less than the green curve 50% of the time, less than the blue curve 75% of the time, and less than the red curve 95% of the time. To generate these statistics, we took the 1 Hz samples of the position reported by the receiver and computed the horizontal deviations from the median position over the campaign. These deviations were binned into 60 second intervals and then sorted. The percentile of occurrence was obtained by sampling the sorted deviations at the desired percentile of occurrence. Brief excursions exceeding 80 meters were observed on a couple of nights, the largest and most frequent excursions occurring on 16 March. It is clear in the plots that GPS position errors were largest when loss of lock occurrences were the most frequent.

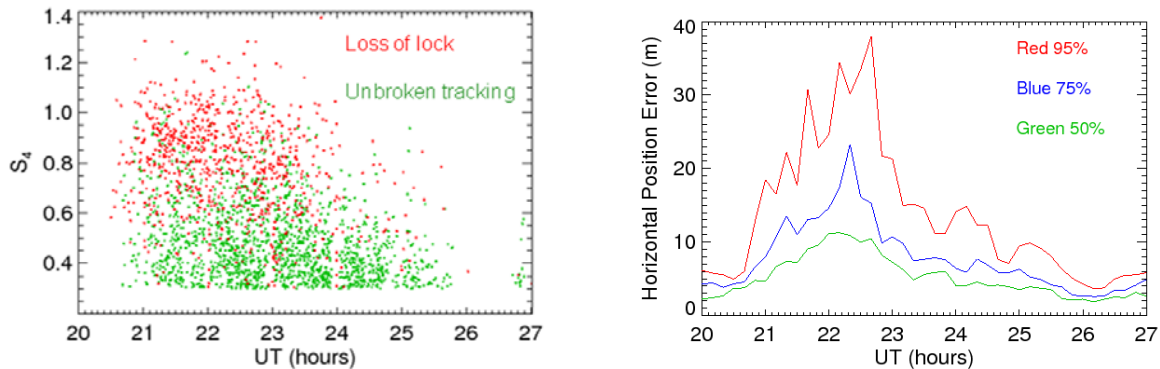


Figure 31. Scatter Plot of L1 S_4 versus Time and 50th, 75th, and 95th Percentile Horizontal Error in the Receiver Reported Position versus Time

Figure 32 (left) shows a histogram of the S_4 index values shown in the previous figure. The blue shaded bars indicate the number of samples associated with loss of lock, while the red bars indicate the total number of samples. Figure 32 (right) shows the ratio of these two

populations, which gives the probability of losing lock as a function of S_4 . The solid curve is a least squares fit to the data of an empirical function of the form:

$$P(x) = \frac{1}{2} \left[1 + \text{Erf} \left(\frac{x - c_3}{c_4} \right) \right] \quad [15]$$

where x is the data to be fit (S_4 in this case), Erf is the standard error function and c_3 and c_4 are parameters to be determined. The values of S_4 which correspond to 50% and 90% probability of losing lock are 0.70 and 0.97, respectively. As expected, when S_4 is low very few loss of lock events are observed. As S_4 increases to the point to saturation, loss of lock becomes highly likely.

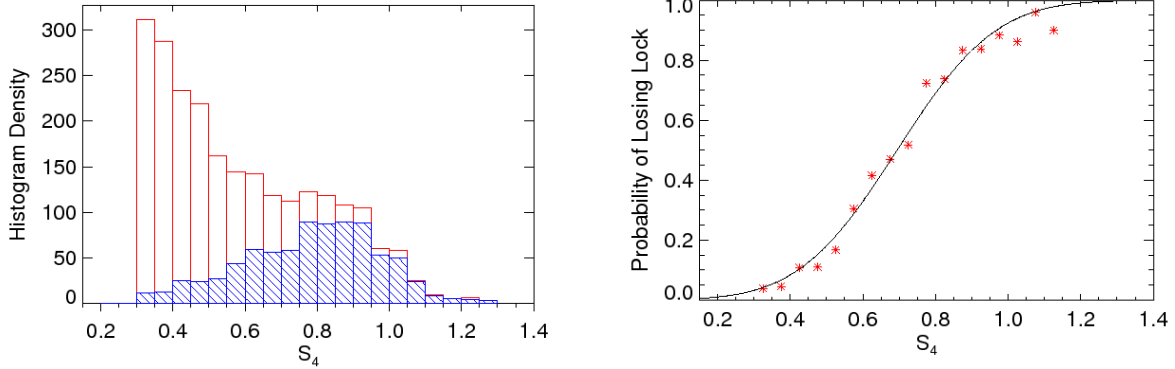


Figure 32. Occurrences of S_4 Associated with a Loss of Lock Event together with the Probability of Losing Lock versus S_4

Figure 33 (left) shows a histogram of the intensity decorrelation time τ_I where, as before, the blue shaded bars show the number of samples associated with loss of lock, while the red bars indicate the total number of samples. Figure 33 (right) shows the ratio of these two populations, which gives the probability of losing lock as a function of τ_I . The solid line shows an empirical fit of the model to these probabilities, using $x=\log_{10}(\tau_I)$ in this case. When the decorrelation time is long, very few loss of lock events are observed. As τ_I decreases, the number of loss of lock events increase.

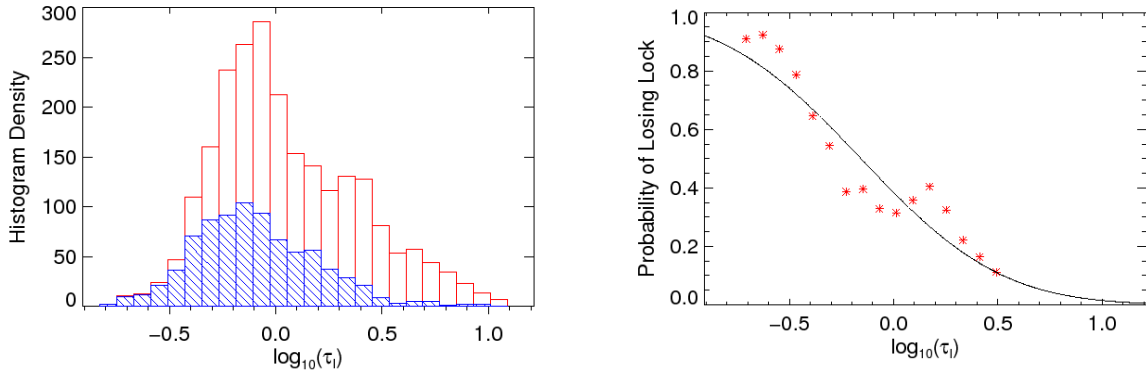


Figure 33. Occurrences of τ_I that are Associated with a Loss of Lock Event (blue) and all Samples (red) with Probability of Losing Lock versus τ_I

Thus far, we have expressed the probability of losing lock as functions of S_4 and τ_I independently. Considering the probability of losing lock as function of τ_I alone is somewhat misleading, however, since the rate of fading will have minimal impact on loss of lock occurrence if the level of fading is low. Therefore, it is informative to consider the joint probability of losing lock, as a function of both S_4 and τ_I together (Figure 34 left). Generally speaking, we found that for each fixed level of S_4 the probability of losing lock increases as τ_I decreases (except, perhaps, for the very largest values of S_4 , for which we may have insufficient samples for reliable statistics). To more clearly quantify this observation, we binned the observations into moderate ($0.3 < S_4 < 0.6$), strong ($0.6 < S_4 < 0.9$), and very strong ($0.9 < S_4 < 1.2$) scintillation conditions and then computed the probability of losing lock as a function of τ_I (Figure 34 right). For moderate to strong scatter the probability of loss of lock increases as the decorrelation time decreases. This trend may not hold for the strongest scattering conditions, for which the probability of losing lock appears to be roughly independent of τ_I .

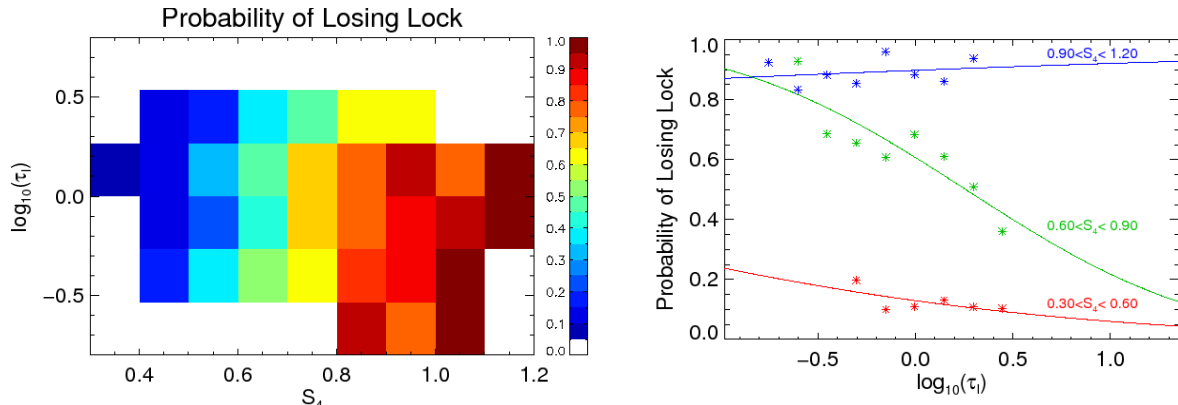


Figure 34. Probability of Losing Lock versus both S_4 and τ_I (left); Probability of Losing Lock versus τ_I for three Different Ranges of S_4 Values (right)

The result of this analysis demonstrates that the rate of GPS signal fading, as quantified by the decorrelation time, is an important factor leading to loss of lock, in addition to the depth of fading (the latter still being the more important effect of the two, however). Since the fading rate is related to the effective scan velocity through the ionospheric irregularities, which is predictable *a priori*, we can anticipate which satellites the receiver is likely to lose lock on more frequently by virtue of the satellite's motion with respect to the magnetic field and plasma drift. While the probabilities of losing lock we determined are specific to a particular GPS receiver model and tracking loop design, our observations that these quantities depend on the velocity of satellite motion with respect to the magnetic field and plasma drift is a general result (i.e. receiver independent).

We note that shortly after this work was completed, other authors noted the relevance and importance of the decorrelation time for modeling GPS performance in the presence of scintillation [Humphreys et al., 2010]. This parameter has since become widely recognized to be a significant factor in determining receiver performance under disturbed ionospheric conditions. Several follow-on investigations of the impacts of ionospheric scintillation on GPS performance involving phase screen simulation [Carrano et al., 2011; Carrano et al., 2012d] were subsequently published in [Carrano et al., 2012b; and Carrano et al., 2014].

Conclusions.

We have analyzed a dataset collected with an Ashtech Z-XII survey grade GPS receiver at Ascension Island during the solar maximum year of 2002. This campaign exhibited some of the most disturbed ionospheric conditions under which high-rate GPS observations have been systematically analyzed. We noted that the rate of fading, as quantified by the decorrelation time, is an important factor in causing loss of lock on GPS signals, in addition to the depth of fading. Since the fading rate is related to the effective scan velocity through the ionospheric irregularities (which is predictable *a priori*) we can anticipate which satellites the receiver is likely to lose lock on by virtue of the satellite's motion with respect to the magnetic field and plasma drift.

3.2.3. Interpretation and Multi-frequency Scaling of Strong Scintillation. Earlier during this contract, we demonstrated that ionospheric turbulence parameters may be inferred from amplitude scintillations well into the strong scatter regime [Carrano et al., 2012c]. This technique, called Irregularity Parameter Estimation (IPE), uses the strong scatter theory and numerical inversion to estimate the parameters of an ionospheric phase screen (turbulent intensity, phase spectral index, and irregularity zonal drift) consistent with the observed scintillations. The optimal screen parameters are determined such that the theoretical intensity spectrum on the ground best matches the measured intensity spectrum in a least squares sense. We found that IPE analysis of the VHF and L-Band scintillations, which exhibited very different statistics due to the wide frequency separation, yielded a consistent description of the phase screen parameters that specify the disturbed ionospheric medium. This discovery motivated a new technique for extrapolating scintillation measurements from one frequency to another (even if the observed scintillations are fully saturated).

We use this technique to interpret scintillation measurements collected during an AFRL campaign at Ascension Island (7.96°S , 14.41°W) in March 2000. Geostationary satellites broadcasting radio signals at VHF and L-band were monitored along nearly co-linear links, enabling a multifrequency analysis of scintillations along (nearly) the same propagation geometry. The VHF data were acquired using antennas spaced in the magnetic east-west direction, which enabled direct measurement of the zonal irregularity drift. The geometry of the experiment was as shown in Figure 35. The two geostationary satellite links were located nearly overhead. The ionospheric penetration points for the two satellite links were separated in the magnetic east-west direction by only 38 km, so the links were almost co-linear.

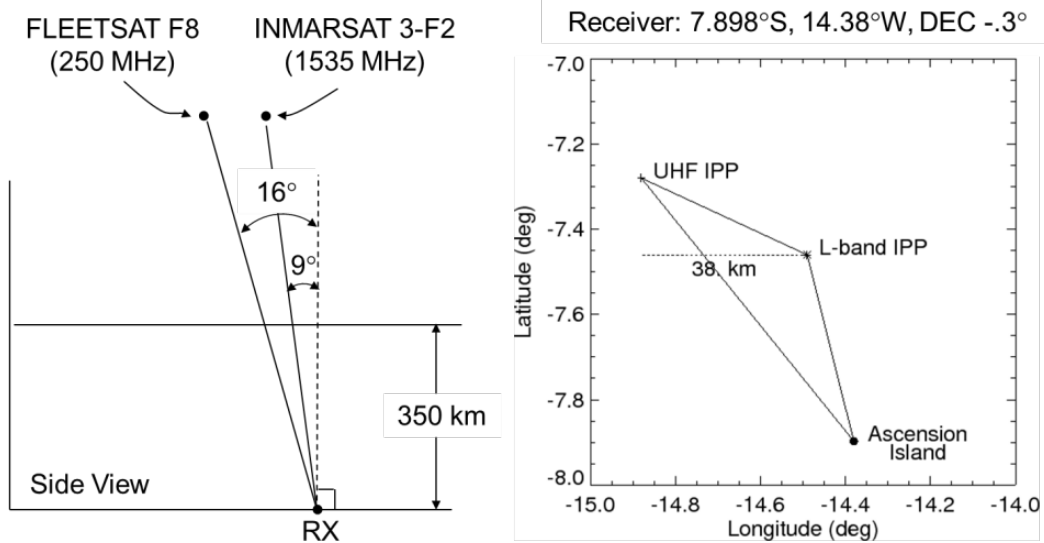


Figure 35. Geometry of the UHF and L-band Links to Geostationary Satellites FLEETSAT-8 and INMARSAT 3-F2

Figure 36 shows the received signal power at the UHF and L-band frequencies during the evening of 22-23 March 2000. The intensity fluctuations are shown in black and the intensity decorrelation times are shown in red. The UHF scintillations are in saturation throughout the evening. The L-band scintillations are saturated early in the evening and become progressively weaker as the evening progresses. Also shown (in red) are the decorrelation times at UHF and L-band.

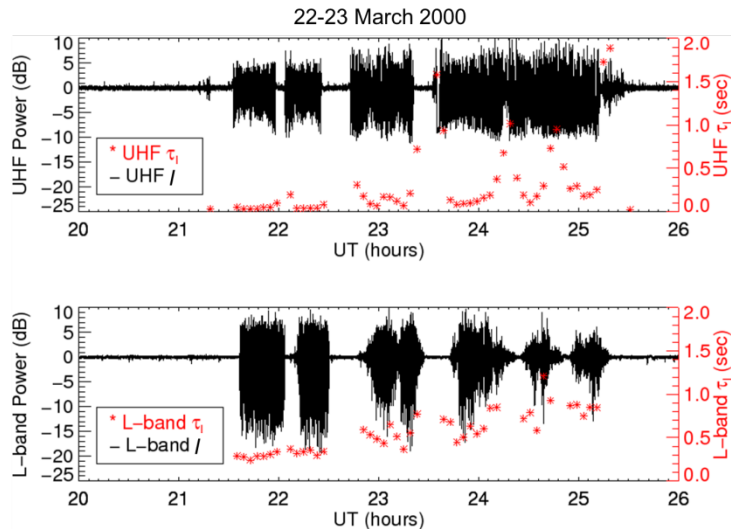


Figure 36. Received Power and Intensity Decorrelation Time on the UHF and L-band Links at Ascension Island during the Evening of 22-23 March 2000

We measured the average zonal drift and the characteristic velocity using standard spaced-antenna techniques [Vacchione et al., 1987; Spatz et al., 1988]. The results are shown in Figure 37 using the spaced-receiver technique one can measure the drift only when irregularities are present, but the irregularities were so strong in the post-sunset sector that the intensity correlation length was shorter than the baseline of the two spaced antennas. Therefore, it was not

possible to measure the drift early in the evening. Since the drift velocity is needed throughout the evening to apply the IPE technique, we fit it with an exponential over the course of the evening. We used this drift to map the measured scintillation time series to a spatial series, and we advanced the L-band data by 38 km to approximately align it with the UHF data (this was necessary because the two signals originated from different satellites). Note that late in the evening, we observed S_4 values greater than one. Also shown in Figure 37 are the exponential fit to the drift measurements (black) and the UHF S_4 (blue). This is a refractive scattering effect associated with strong focusing by large scale irregularities. In general terms, we noted a progression of S_4 values starting around unity early in the evening progressing to values larger than one as the evening progressed. This effect has been observed by previous authors e.g. Bhattacharyya et al. [2003].

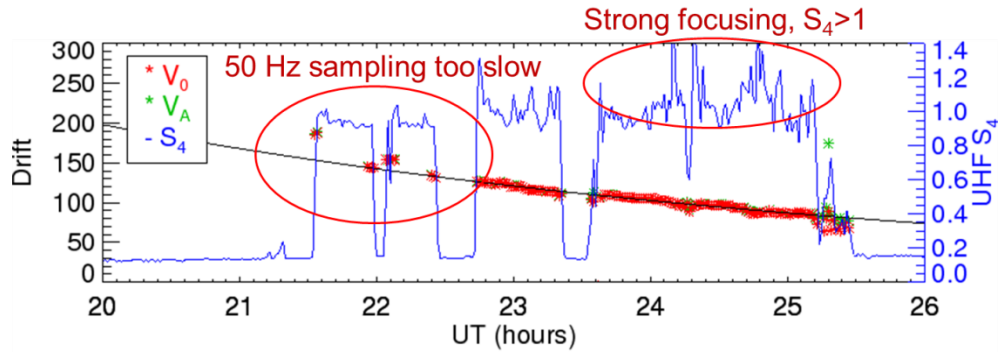


Figure 37. Average and Characteristic Zonal Irregularity Drift at Ascension Island during the Evening of 22-23 March 2000

We interpret the scintillations at UHF and L-band using the theory of strong scatter. Given a statistical description of the random ionospheric medium, the scintillation statistics for any frequency may be obtained by solving the 4th moment equation governing the statistics of intensity fluctuations. We assume the interaction of the medium with the wave can be described as the traversal of a plane wave through a thin phase-changing screen. The strong scatter theory can be expressed in a universal form such that different combinations of perturbation strength, propagation distance, and frequency produce the same results [Rino and Carrano, 2013]. The strength of scatter is parameterized in terms of a universal scaling parameter U . Mathematically, U is the phase spectral density function normalized by the Fresnel scale, and then evaluated at the Fresnel scale. Values of U less than one correspond to weak scatter, whereas values of U greater than one correspond to strong scatter.

Figure 38 illustrates the behavior of S_4 and the normalized intensity correlation length as a function of the scattering strength U . Each curve shown corresponds to an unmodified power law with a different value of the phase spectral index, p . If the phase spectral index is shallow ($p < 3$), then S_4 increases to a saturation value close to unity with little overshoot. Once saturation occurs, S_4 ceases to provide useful information about the scattering or irregularity strength. On the other hand, if the spectral index is steep ($p > 3$), then S_4 will approach a quasi-saturation state with a value exceeding unity. The presence of an outer scale will mitigate this quasi-saturation state and drive S_4 from its local maximum back down to unity as the scattering strength continues to increase. Hence, the curves for S_4 shown in Figure 38 can be thought of as upper bounds for the values that can be attained for a physical random medium with an outer scale. The bottom two plots show the intensity correlation length normalized by the Fresnel scale. For

shallow slope spectra ($p < 3$), there is little change in the correlation length when the scatter is weak ($U < 1$). Once saturation occurs the correlation length begins to decrease with increasing scattering strength. This provides a mechanism for measuring the scattering strength (and with foreknowledge of the Fresnel scale, also the irregularity strength). If the phase spectral index is steep ($p > 3$) the variation is somewhat more complicated, but still the strong scattering theory allows us to infer the scattering strength by measuring the intensity correlation length.

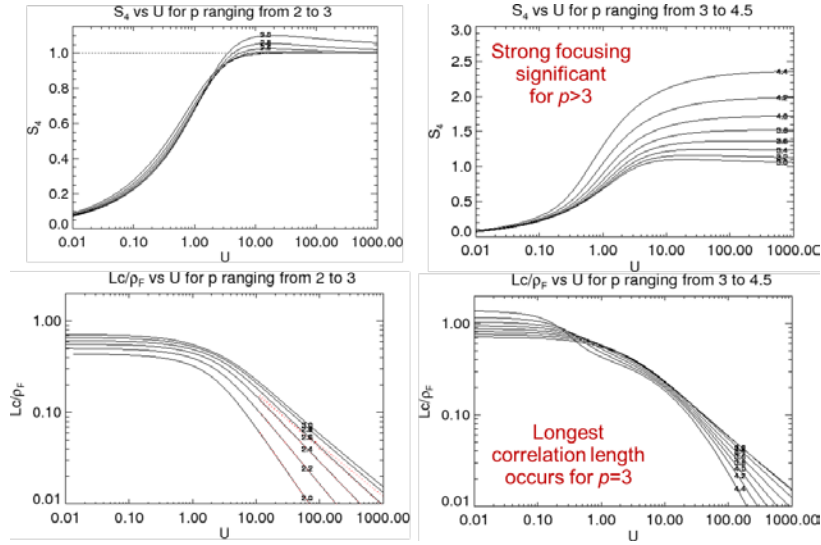


Figure 38. S_4 and Normalized Intensity Correlation Length as a Function of the Scattering Strength U for Shallow Spectra with $p < 3$ (left) and Steep Spectra with $p > 3$ (right)

The observation that the intensity correlation length decreases with increasing strength of scatter once saturation is achieved inspired us to develop a technique we call “Correlation Length Mapping” (CLM). Figure 39 shows the UHF S_4 and the intensity correlation length, which is the decorrelation time multiplied by the zonal drift. Inside the bubbles the correlation length is short early in the evening (<10m), and it increases as the night progresses (to over 100 m). To apply the CLM technique the phase spectral index must be known. We assume a value of $p=2.5$, which is the default value used by the Wideband Scintillation Model (WBMOD) at low latitudes [Secan et al., 1995]. From the correlation length at UHF and knowledge of p we can look up the scattering strength at UHF (e.g. using the lower-left panel of Figure 38). This can readily be scaled to the scattering strength at L-band. From the scattering strength at L-band we can look up the S_4 at L-band (e.g. using the upper-left panel of Figure 38). These predicted S_4 values are compared with the S_4 measurements in the lower panel of Figure 39. The predicted values well-delineate the bubbles (note, in particular, that the method correctly predicts the subdivision at L-band of what appears to be a single bubble at UHF). However, the predictions consistently underestimate the measurements. We can show that no matter what value of spectral index we choose for a one-component spectral model, the predictions using the CLM still underestimate the measurements.

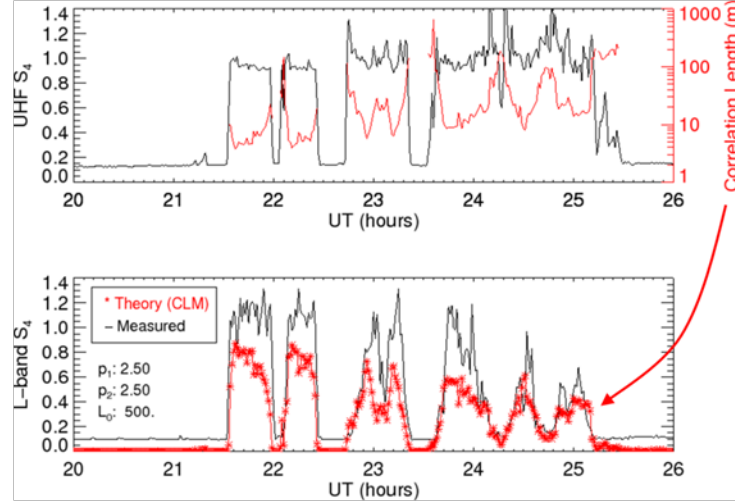


Figure 39. Measured S_4 at UHF and Intensity Correlation Length for UHF (top) with Measured S_4 at L-band and Predicted S_4 at L-band from the Intensity Correlation Length at UHF using an Unmodified Power Law Irregularity Model with $p=2.5$.

This observation led us to consider the possibility that the medium might be better characterized by a two-component irregularity spectrum. We experimented with a two-component spectrum with low frequency slope $p_1=2.5$ and high frequency slope $p_2=3.8$ with a spectral break at $L_b=500$ m. Figure 40 shows the variation of S_4 and correlation length for UHF as a function of scattering strength using this two-component model with $p_1=2.5$, $p_2=3.8$, and $L_b=500$ m (solid) for the irregularities. Curves for unmodified power laws with $p=2.5$ and $p=3.8$ are shown for comparison (dotted). Because the Fresnel scale for UHF lies in the shallow portion of the irregularity spectrum in this case, the S_4 development behaves as if the medium were a single component law with $p=2.5$, but the correlation length is increased substantially for large U .

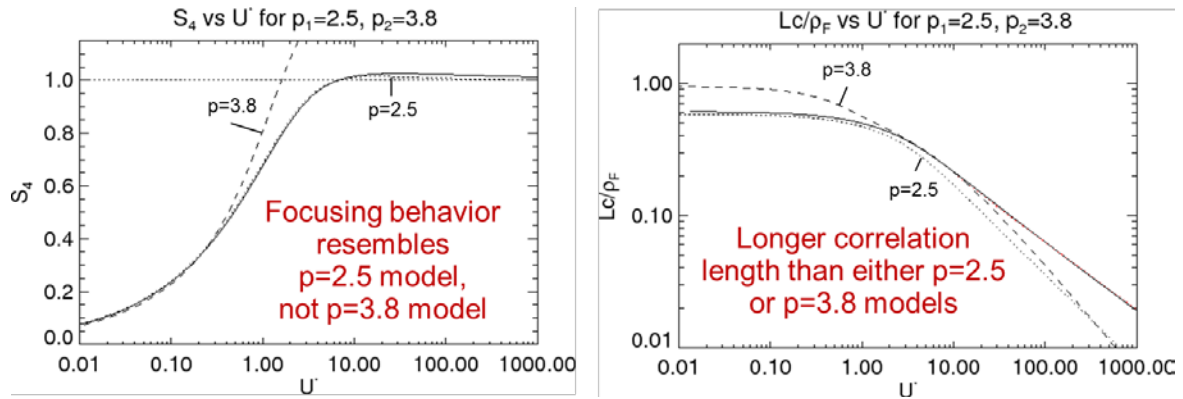


Figure 40. S_4 and Correlation Length for UHF as a Function of Scattering Strength for a two-component Power Law

When a two-component irregularity model is assumed, the CLM does much better at reconciling the level of scintillation at UHF and L-band (Figure 41). Previous authors have also noted that a two-component irregularity model may be required to reconcile scintillations at UHF and L-band at Ascension Island [Franke et al., 1985]. We note that the CLM technique is simple and fast to apply (suitable for real-time applications) and should satisfy a long-standing need of

the Air-Force to reliably map scintillations observations at one frequency (even if they are saturated) to scintillation at other frequencies. The agreement between the predictions and measurements are not perfect, however, partly because we have assumed the spectral shape remains fixed over the course of the evening, which unlikely to be the case.

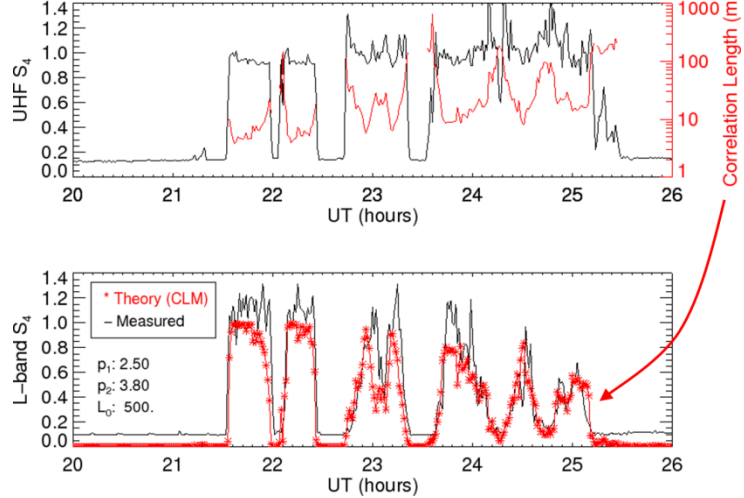


Figure 41. Measured S_4 at UHF and Intensity Correlation Length for UHF (top) with Measured S_4 at L-band and Predicted S_4 at L-band from the Intensity Correlation Length at UHF

The principal limitation of the CLM technique is that the correct spectral indices and break scale are not known *a-priori*. To overcome this limitation, we developed a more power technique, which we call Irregularity Parameter Estimation (IPE). In the IPE technique we fit the intensity spectrum predicted by the strong scatter model to the intensity spectrum that we actually measure. In this way, the scattering strength and parameters of the irregularity model (in this case p_1 , p_2 , and L_b) are inferred directly from the spectral density function of the observed intensity fluctuations. The IPE technique can be applied to each signal (UHF and L-band) independently. In this case, however, we actually fit both UHF and L-band spectra simultaneously, in order to find the set of irregularity parameters that best reconcile the observed scintillations at both frequencies.

Figure 42 shows an example of the IPE technique applied to scintillation data early in the evening, when UHF and L-band are saturated with S_4 close to unity. The data shown is for 22.38 UT, early in the evening. The scintillation characteristics are clearly very different at the two frequencies, even though the S_4 values are the same (unity). The break scale estimated by the fit was about 600m, which is consistent with earlier in-situ observations. The spectral indices for the low and high frequency portions of the irregularity spectrum are close to 2 and 4, respectively, which are also similar to previous in-situ observations. Note that there is a significant departure in power law behavior in the intensity field when the scatter is strong. Nevertheless, one can still infer the irregularity parameters using this least-squares fitting technique.

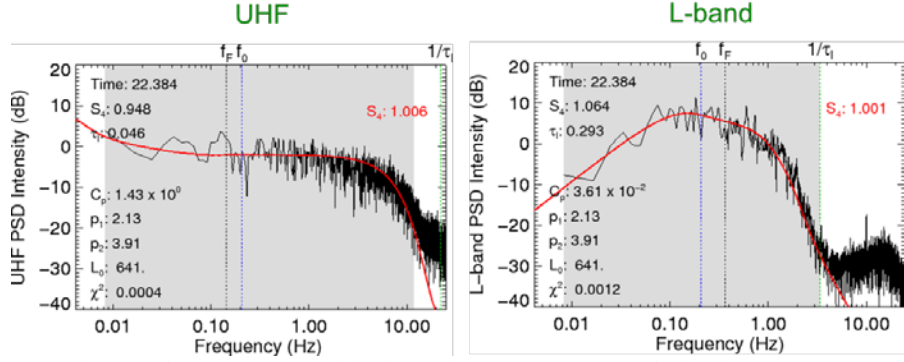


Figure 42. Measured Intensity Spectrum (black) and Least-Squares Fit by the Strong Scatter Model (red) for UHF and L-band at 22.38 UT

Two hours later, scattering conditions have changed substantially (Figure 43). The data shown is for 24.38 UT, late in the evening. The UHF signal is now experiencing strong focusing effects with S_4 equal to 1.4, while the L-band signal is experiencing weak scatter conditions with S_4 equal to 0.2. The break scale has lengthened significantly to 2 km. In this case, the spectral break essentially functions as an outer scale.

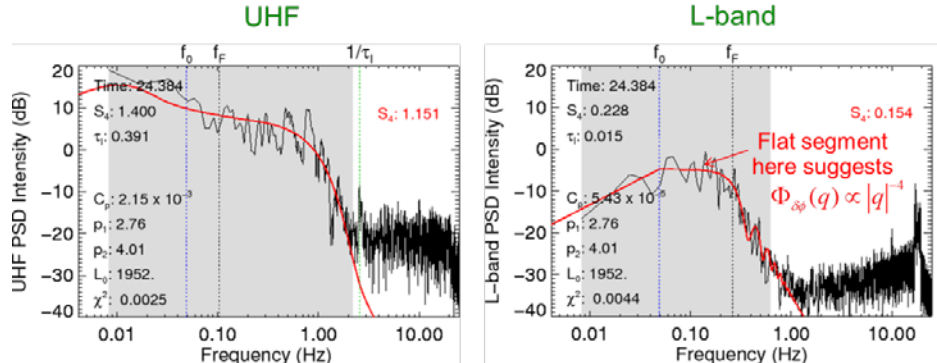


Figure 43. Measured Intensity Spectrum (black) and Least-Squares Fit by the Strong Scatter Model (red) for UHF and L-band at 24.38UT

Next we present the variation in the fit parameters over the course of the evening. We perform the model fit every two minutes and update the irregularity parameters with this cadence. Figure 44 shows the measured and predicted S_4 values, in black and red for UHF and L-band, respectively. The fit is excellent because the two-component irregularity model is generally able to reconcile the scintillation observations at the two frequencies. Some spectra cannot be fit well and a high chi-squared results, for example, if the irregularities are not fully developed or are highly non-stationary. In this case, this data are discarded. We did not have to discard much data on this evening.

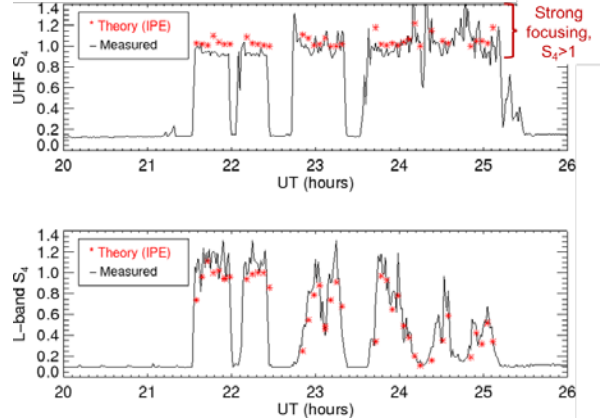


Figure 44. Measured and Predicted S_4 using the IPE Technique for UHF and L-band

Next we show how the irregularity parameters varied over the course of the evening (Figure 45). The points in green show the variation in the low frequency slope of the irregularity spectrum, p_1 . This value shows some variation but remains close to 2.5 the entire evening. The high frequency slope p_2 (shown in red) steepens a little, from 3.5 to 4 or 4.5 in the course of the evening. The median value was 3.8 and also does not change dramatically over the course of the evening. Conversely, there is a significant and systematic increase in the break scale L_b . The break scale starts around 500 m and over the course of the evening it migrates to larger scales, on the order of 1-2 km. As this migration occurs we observe stronger focusing effects at UHF. The S_4 value at UHF (blue) is shown for comparison.

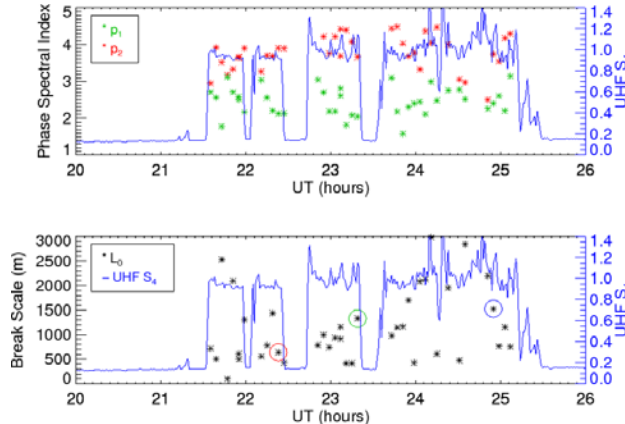


Figure 45. Irregularity Parameters Estimated with the IPE Technique

Next we present the scattering strength U , which is the normalized phase spectral power at the Fresnel scale. This parameter (which depends implicitly on p_1 , p_2 , and L_b) dictates the development of the intensity fluctuations. When it exceeds unity strong scatter conditions prevail, and when it is less than unity weak scatter conditions prevail. Figure 46 shows that initially the scattering strength at UHF is 1000 times larger than unity (deeply into the strong scatter domain) and then drops by about 2 orders of magnitude over the course of the evening. Even still, the UHF signal remains in the strong scatter domain at the end of the evening. At L-band the scattering strength is a small multiple of unity (2-5), and shortly after midnight recedes into the weak scatter domain for the rest of the evening. In weak scatter conditions, the scattering

strength parameter is proportional to the square of S_4 . The S_4 values at UHF and L-band (blue) are shown for comparison

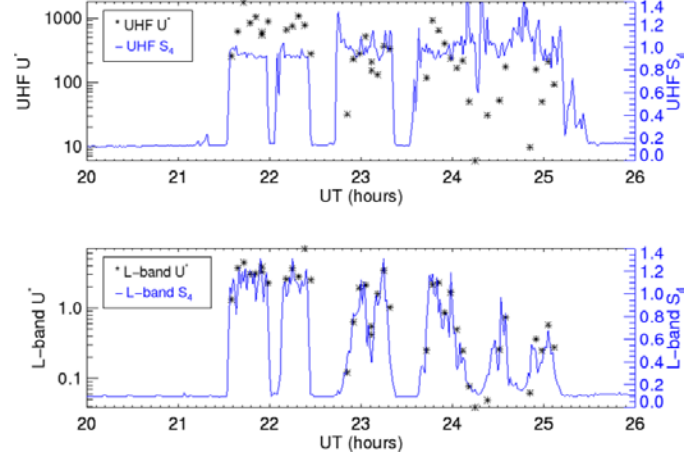


Figure 46. Scattering Strength Estimated with the IPE Technique at UHF and L-band

At this stage we can comment on the evolution of irregularity structure during this campaign at Ascension Island. First, we found that a two-component spectral model is required to reconcile the scintillation observations at UHF and L-band. Second, we found that the spectral slopes do not change dramatically, but the break migrates significantly from small scales to larger scales over the course of the evening. We summarize the results in Figure 47. Early in the evening the UHF Fresnel scale falls in the shallow-sloped portion of the irregularity spectrum (which does not admit strong focusing), but as the break migrates to larger scales later in the evening the UHF Fresnel scale lies in the steeply sloped portion of the spectrum (which does admit strong focusing). It is the migration of the break scale to larger scales which creates the conditions under which strong focusing predominates at UHF late in the evening.

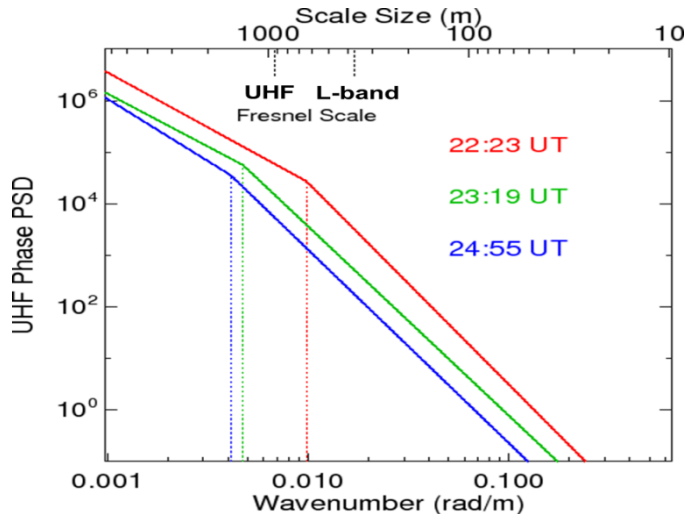


Figure 47. Phase Spectrum at Three Times during the Evening

Conclusions.

We have developed two new techniques to reconcile multi-frequency observations, the correlation length mapping technique (CLM) and irregularity parameter estimation (IPE). We found that in order to reconcile these UHF and L-band measurements at Ascension Island a two-component spectral model is needed. We have leveraged these techniques to understand how the irregularities responsible for strong scatter conditions at low latitudes decay in time, and how the migration of the spectral break to larger scales promotes strong focusing later in the evening at UHF. We believe this is the first time the details of irregularity evolution have been inferred directly from ground-based scintillation measurements.

3.3 Ionospheric Sensor Installations

This contract also addressed the installation and operation of two ionosondes. These ionosondes were purchased and deployed under Contract #FA8718-04-C-0055. They were transferred administratively as Government Furnished Property to the current contract under P00031. These two ionosondes were deployed to Addis Ababa, Ethiopia and Maseno, Kenya.

This contract also supported the installation of a third ionosonde in Tupiza, Bolivia. Support consisted of personnel to prepare the site and initiate continuous operation of the ionosonde.

These ionosondes are currently operational and providing routine measurements for ionospheric studies of relevance to this contract and to Air Force interests. The ionosonde hardware is the Vertical Incidence Pulsed Ionospheric Radar (VIPIR) developed and built by SCION Associates. The VIPIR is a fast operating fully digital pulse radar with a frequency range of between .3 and 25 MHz. It features a 4kW solid state power amplifier to achieve sufficient SNR (signal to noise) ratio to provide reliable measurements under a variety of ionospheric conditions. The operation and initial data management is made with the use of two Linux-based computers integrated in the system.

The VIPIR ionosonde consists of the following major parts:

1. Electronic units (Receiver, Reference, Exciter, Front End, Balun, Control Computer and UPS)
2. Transmit antenna (Inverted delta)
3. Receive antenna array (8 cross-dipole antennas nominally)

Two VIPIR ionosondes were installed in East Africa in 2011 and 2012 under the auspices of contract #FA8718-04-C-0055. The first instrument was installed near Addis Ababa, Ethiopia (9°N, 38.6°E), and the second one in the vicinity of Maseno University, Kenya (0°S, 34.6°E). The ionosondes were made operational under this current contract. The ionosonde in Kenya was placed in a routine operation on October 23, 2012, and Addis Ababa system began routine operation on June 5, 2014.

The Tupiza ionosonde was installed in late 2012.

3.3.1 Maseno, Kenya Ionosonde. Figure 48 shows an aerial photo (from Google map) of the field site on the land property of Maseno University with the shelter and antenna locations. This field is located approximately 1 km north of the Maseno campus precisely at geographic equator. The electronic units are hosted inside the shelter which was built in the frame of this project by Maseno University group. An air conditioner installed inside the building provides temperature

regime suitable for the system operation. The field site is sufficiently flat and reasonably large to host a transmit antenna with ~70m separation between the masts. The height of the transmit antenna masts is 26m, and the height of receive antennas is 3m. All eight receive antennas were installed in the field. The transmit antenna and the center of the receive antenna field are approximately 40m away from the shelter. Electric power is taken from the university grid. The cables to antennas inside flexible conduits are dug-in to a depth of about 1m. The field is surrounded by a fence and watch guard is constantly present. Figure 49 shows the system installation with the antenna field on the left and the air conditioned building (right) hosting the electronic unit, USB power sully and the wireless network.



Figure 48. Ionosonde Field Site at Maseno, Kenya



Figure 49. VIPIR System Installation in Maseno, Kenya

Maseno Ionosonde Measurements

The Maseno VIPIR ionosonde started routine operation on October 23, 2012. It operated continuously until the Christmas time break (12.24.12) when the power was shot down for the entire university. Figure 50 shows examples of daily variations of foF2 values (i.e., peak electron density) recorded with Maseno sounder on October 30 and October 31, 2012. Sunrise and sunset times are indicated with open and closed circles correspondingly. The periods of spread-F are indicated with vertical error bars, foF2 values for those times are estimated. It is

worth noting that during the night of October 30/October 31 spread-F was observed twice: shortly after the sunset (18-20 UT) and much later at night (23-01UT).

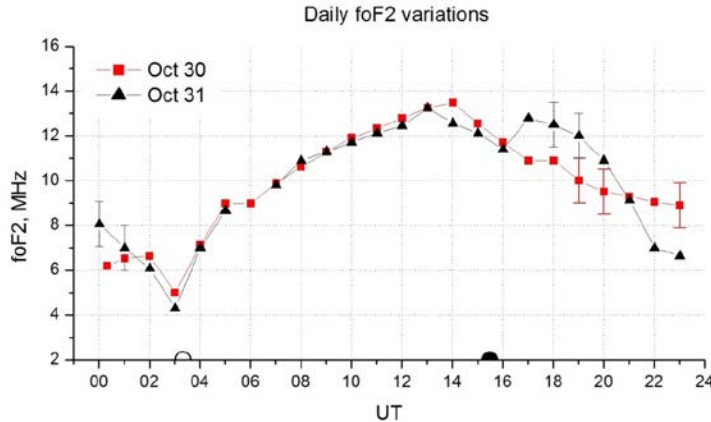


Figure 50. Daily foF2 Variations Recorded at Maseno on October 30, 31 2013

It is remarkable that during the daytime the foF2 trends measured on two days were almost identical, with the notable difference observed only during the night time. On both of the days the spread-F conditions were observed which are indicated in plot with vertical error bars (with arbitrary length). It is very interesting that on the night of October 30/October 31 spread-F conditions were observed twice during the night: shortly after the sunset (18-20 UT) and much later at night (23-01UT). The intensities of all observed spread-F conditions were approximately similar. The presence of the late night spread-F is similar to the observations of late-night ionospheric scintillations made at Nairobi GPS TEC SCINDA receiver. It will be very interesting to investigate this phenomenon in further details and try to determine what geophysical conditions in this region are responsible for the formation of the equatorial spread-F during several hours after the sunset.

In 2013, however, it was discovered that one of the electronic units, namely the IQMux card of the receiver chassis has developed a serious problem which was not possible to fix on site. Therefore, the entire receiver chassis was taken to the US where the faulty IQMux card was replaced by the manufacturer of the VIPIR sounder. The new IQMux card was installed in November 2014 making the system operational, however, in December 2014 a power surge destroyed a UPS unit which is critical for the system operation under the conditions of bad quality of 230 V main power line. In March 2015 a new UPS unit was purchased and delivered to Maseno, Kenya. The sounder is currently operational and makes routine ionospheric measurements. Internet connection to the sounder was established via 3G wireless subscription. An internet bundle for several month of operation was purchased, however, continuous communication of 3G connection requires more funding.

Figure 51 shows availability of the measurements made in 2015 after the system repair. Denser shading indicates measurements with higher cadence. From July 14 to July 24, 2015 the instrument was making ionograms every minute.

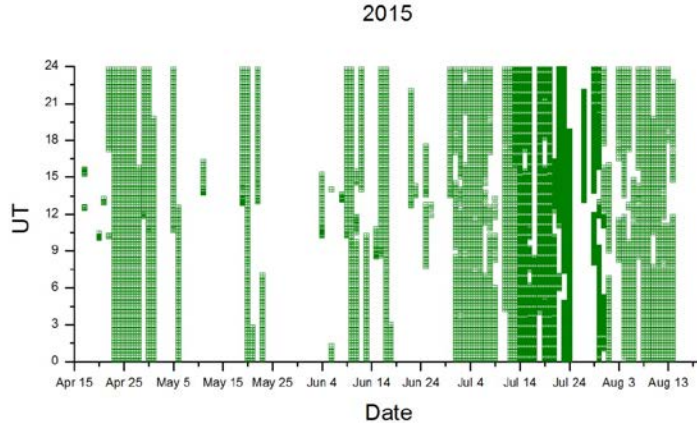


Figure 51. Maseno Ionosonde Data Availability

The data quality of the measurements made by Maseno sounder is very high quality. Despite the relatively short period of a stable operation, we have been able to observe a number of interesting phenomena which will need further study to reveal the underlying physical processes. Figure 52 shows two consecutive ionograms recorded on July 20, 2015 with very unusual Es layer stratification. We plan to investigate and to model possible plasma distribution which can give rise to such features in the ionograms.

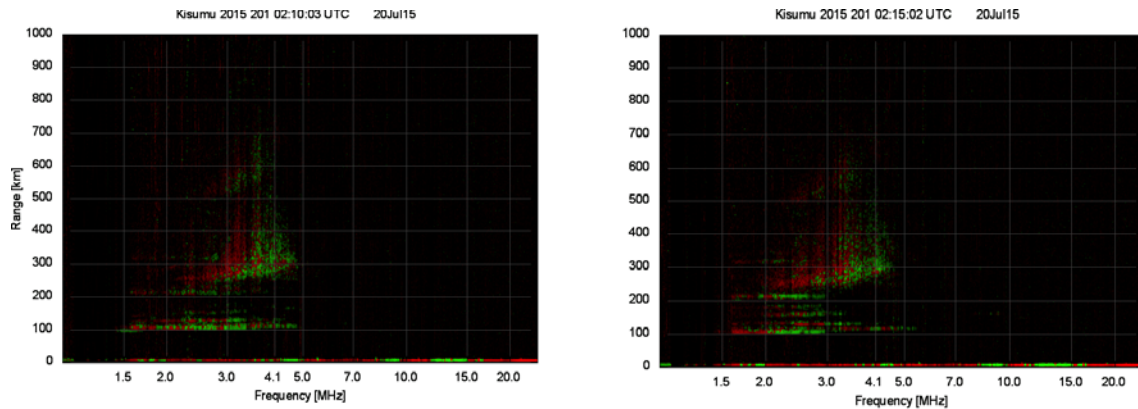


Figure 52. Consecutive Ionograms Recorded at Maseno with Unusual Es Layer Stratification

Figure 53 illustrates the the quality of the measurements after the recent repairs with a sequence of ionograms made every 5 min on July 14, 2015. The plot shows signal strengths in dB for ordinary (red) and extraordinary (green) waves. The ionograms demonstrate the high quality of the measurements: high frequency and range resolution, clear separation of the O and X traces, high signal-to-noise ratio, and high transmit power indicated by the presence of multiple reflection echoes. The sequence shows a highly dynamic behavior of the F1 region of the ionosphere, which is normally assumed to be rather stable. Note an appearance of the second reflection near 6 MHz at 11:15 UT. This signature does not fit into the usual explanation of the gravity wave propagation because of its localized appearance on the trace ad rapid vertical motion.

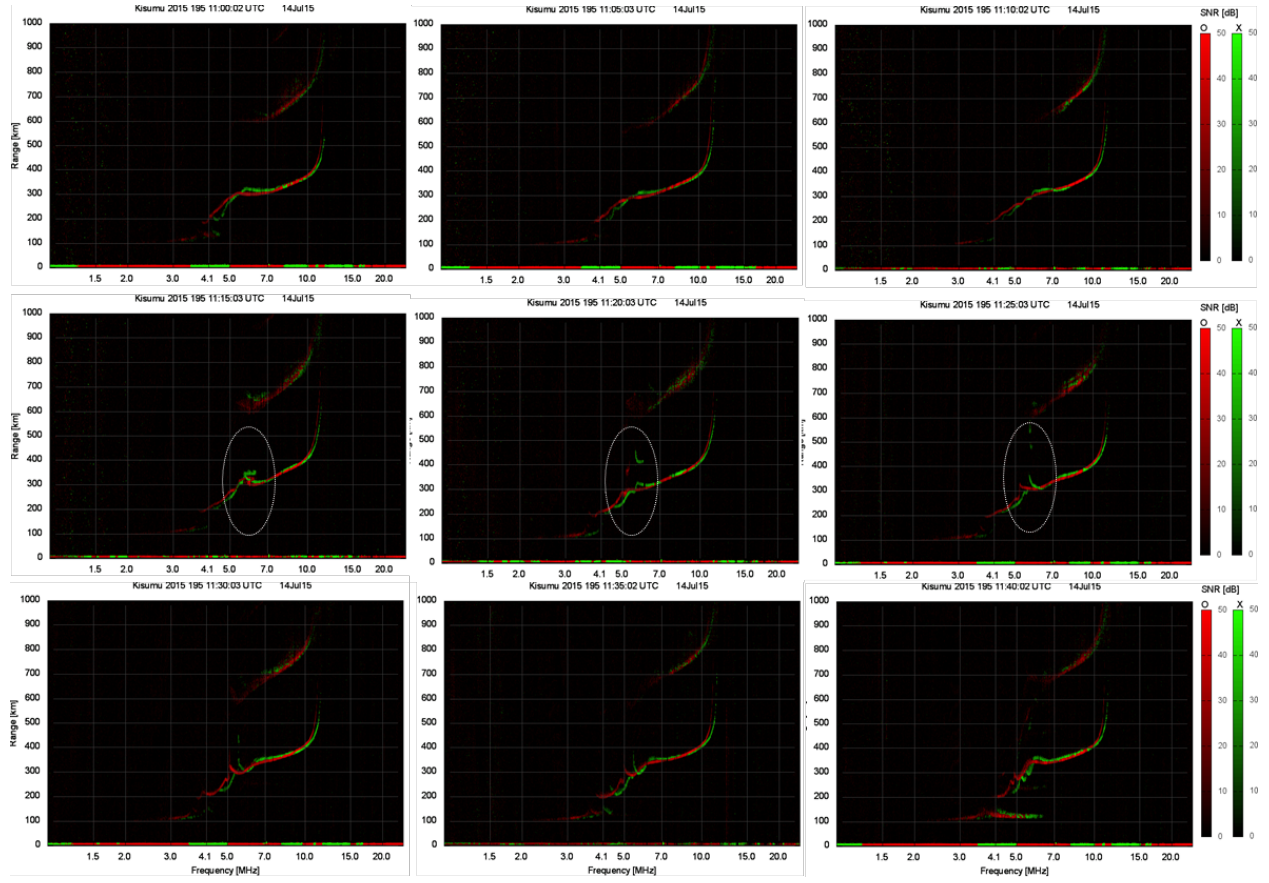


Figure 53. Recent Measurements at Maseno, Kenya after Several Repairs

3.3.2 Addis Ababa, Ethiopia Ionosonde. The system in Addis Ababa has an overall installation layout similar to Maseno sounder, with the transmit antenna being about twice smaller in size. In May 2014 Addis Ababa University connected a local power grid to the sounder, completed a security fence around the installation and also erected two brick building for permanent hosting of the system (control and operation units). One of the buildings is shown in Figure 54 together with the VIPIR electronic unit. A second building (not shown) will be used for overnight stays of students and personnel visiting the site.



Figure 54. VIPIR System Installation at Addis Ababa, Ethiopia

Addis Ababa Ionosonde Measurements

After the connection to the local power grid, the system was put in a full functional mode as of May 30, 2014 and began routine operation on June 5, 2014. On August 1, 2014, the system stopped working because of the failure of the local power transformer. The Ethiopian power company was able to fix the transformer in April 2015. The system is currently being put in operation by Addis Ababa university team. Figure 55 shows example of ionosonde data from Addis Ababa system recorded on July 29, 2014. Note the second hope reflection (above 900km) indicating a good signal to noise ratio of the ionogram.

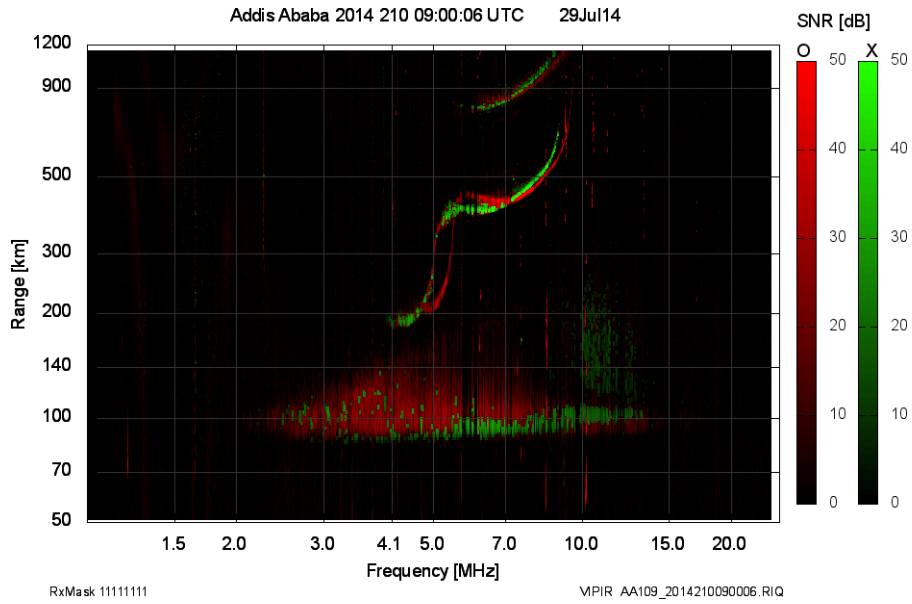


Figure 55. Ionogram Recorded by Addis Ababa VIPIR Ionosonde on July 29, 2014

Figure 56 illustrates the daily trend of foF2 recorded at Addis Ababa on 20 June 2014. Note the difference between the day time (06-10 UT) and night time (18-06 UT) values.

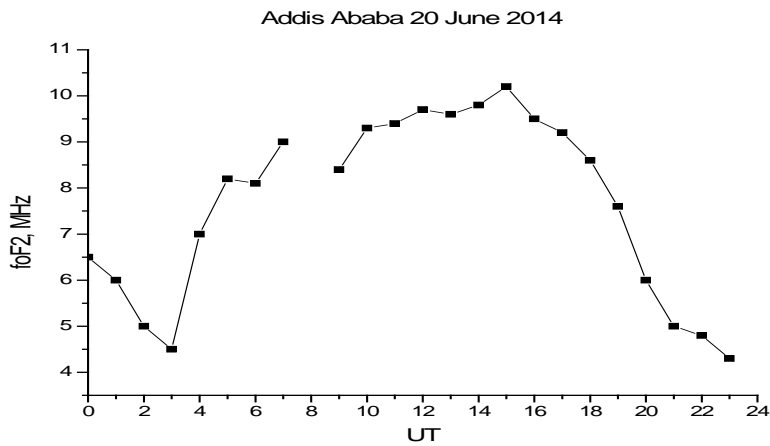


Figure 56. Daily foF2 Variations Recorded at Addis Ababa on 20 June 2014.

Remote connection to the sounder is implemented via wireless 3G network. Continuous access to the system requires regular purchasing of data bundles.

Web data repository

Boston College has also established a repository for storing the data collected with the African systems and implemented a corresponding web interface. Web access and image display of the data makes possible a quick analysis of the data availability and data quality as well as verification of system conditions.

At present, all the data collected by Maseno and Addis Ababa ionosondes are stored in Boston College web repository. Addis Ababa data for year 2014 are also available on NOAA server:

<http://ngdc.noaa.gov/ionosonde/data/AA109/individual/2014/>

3.3.3 Tupiza, Bolivia Ionosonde. A VIPIR ionosonde was installed in the southern Bolivian city of Tupiza ($21^{\circ} 26' S$; $65^{\circ} 43' W$; altitude = 3011 m) making it possible to have simultaneous measurements with 2 ionosondes that are closely placed along the same field line. A world class 4-tower, log-periodic transmitting antenna was erected with a superb sensitivity at low frequencies. A new shelter was built near the antenna to house the equipment, and a power line was extended to provide electricity to the system. Eight receiving antennas were placed using underground cabling protected by PVC conduit to avoid any damage due to the extreme rainy conditions and small predatory animals. Two fences were constructed. The first inner fence was placed to protect the antenna feeder from stray animals and the outer fence consisting of barb wire to deter trespassers entering the field site. The system is also protected by hills in the southern part and a small vigilant security shelter on the west side. This post is constantly guarded by enlisted military men. Intense system debugging and testing had to be conducted due to the fact that several cards were disconnected during the trip from Boston to Tupiza. The system started continuous operations on November 1, 2012 and has been operating since then.

Figure 57 shows the pictures from the VIPIR system installation at Tupiza, Bolivia. The two photographs correspond to the transmitting antenna field and some of the receiving antennas and the shelter of the site at Tupiza. The photograph on the left shows 2 of the towers that hold the transmitting antenna and the photograph on the right display one of the receiving antennas and the shelter behind this antenna. The photo on the right shows the shelter that was constructed to house the VIPIR instruments. The field was cleaned from bushes and leveled to assure perfect transmitting conditions. A power line was extended to the shelter site to provide more reliable and continuous electricity. Internet connection was also included using cellular phone lines.

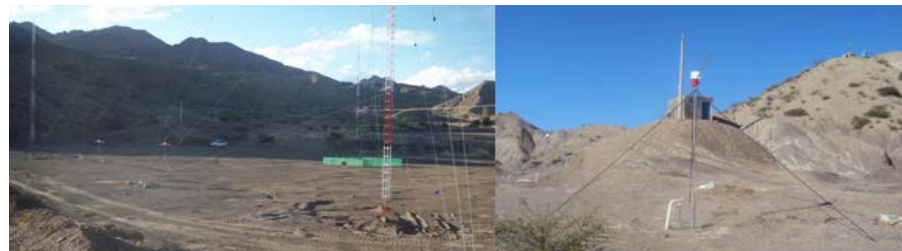


Figure 57. VIPIR System Installation at Tupiza, Bolivia

The following two plots shown in Figure 58 show 2 sample ionograms that were obtained in November 2012 and January 2013 respectively. The left Figure corresponds to the passage of a TID that was observed on November 16, 2012. The right Figure was obtained during the initiation of an equatorial spread F event that happened at 0335 local time. Prior to this time, there was no spread F events or bubbles within the field-of-view of the ionosonde. Multiple layers were seen inside the beam of the radar indicating a high degree of large scale structuring. Frequency-type ionograms were observed in the following ionograms that last for a few hours. At the present, we have accumulated ionograms data corresponding to 2 years of operations and are conducting studies of the variability of the density profiles using ionograms from the other VIPIRs in SA.

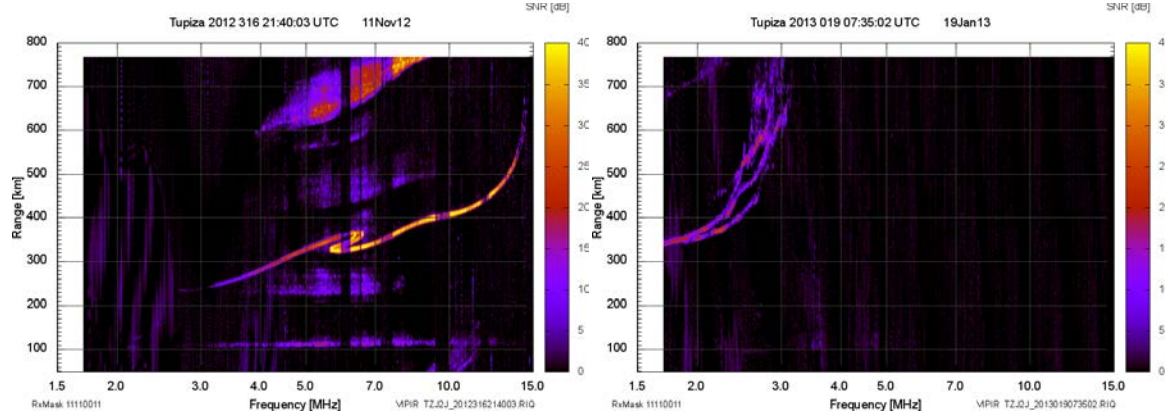


Figure 58. Ionograms Recorded by the Tupiza VIPIR Ionosonde in November 2012 and January 2013

Access to the Tupiza ionosonde data is available from the LISN website (<http://lisn.igp.gob.pe>).

Summary

Installation of VIPIR sounders at the equatorial region in Africa had provided a unique opportunity for monitoring ionospheric dynamics with the high-resolution. This region is very interesting from the geophysical point of view, but so far has been largely devoid of the routine ionospheric measurements. Despite the logistical challenges presented by sub-Saharan Africa, because of the vast acquired experience, only minimal funding is required to maintain the uninterrupted operation of the VIPIR instruments. A rough estimate would be \$3-4K per sounder per year which will cover travel expenses, real-time internet connection and site maintenance.

The Tupiza ionosonde is also operational and providing near real time data.

3.3.4 Coherent Backscatter Radar in Bahir Dar, Ethiopia. Under this contract, Boston College also supported the development and installation of a 50 MHz coherent backscatter radar in Bahir Dar, Ethiopia. The primary purpose of the so-called Blue Nile Radar (BNR) is to investigate longitudinal differences in equatorial bubble structures; similar systems operate in the American (Jicamarca, Peru; Sao Luis, Brazil) and the Pacific (Christmas Island, Kiribati) sectors. Longitudinal differences in bubble features and scintillation patterns have been noted previously from both ground- and spaced-based sensors and the radar will provide detailed characterization of bubble parameters in Africa for unambiguous comparison with the American and Pacific sectors. The joint radar deployment team consisted of two government personnel, two BC staff

members, and one materials provider. The team enjoyed the support of an even larger contingent of students and staff from Bahir Dar University. An entire month was dedicated to the installation process in the last year of the contract. The antenna array had been surveyed previously and the antenna base anchors were already installed when the team arrived on site. The allocated time was adequate but not excessive.

The system consists of an array of 64 custom-built yagi antennas arranged in an 8 x 8 “staggered” array configuration as shown in Figure 59. A total peak transmit power of 16 kW is provided by an 8-channel x 2 kW Tomco power amplifier operating at 49.9 MHz. The system operates monostatically by transmitting and receiving through all antennas via an ATRAD passive T/R switch with additional transmit/receive isolation provided by an active switch/low-noise amplifier front end component designed by AFRL. Manuals for the amplifier and T/R switches were delivered with the components themselves on site.

NEC modeling prior to installation showed that the staggered spacing between adjacent rows reduced the severity of grating lobes during beam-steering. Steering is achieved by adjusting the phase of each row, which is controlled by 8 independent two kW transmitters each feeding a row of 8 antennas. Each transmitter is controlled by a USRP X300 software defined radio that provides both the amplitude and phase of the pulses provided to the high power amplifier and also samples the received data stream. Each radio is capable of controlling and sampling two complex channels. A system diagram illustrating the primary components and connections is shown in Figure 60. A high-power coupler (not shown in the Figure) allows the system to sample the transmitted pulse as well which enables unambiguous decoding for complex waveforms. The phase in the N-S direction is shifted by a sequential fixed offset of 30° on consecutive antennas to induce a fixed beam tilt of approximately 10° to the north to maintain perpendicularity to the magnetic field in the ionosphere to maximize sensitivity to field-aligned irregularities. Precise timing and coherence between the independent channels is derived from a GPS-clock providing synchronization signals on eight channels.

Currently the radar is being operated in two modes, one targeting daytime electrojet echoes and another aimed at detecting post-sunset Spread F events. Both employ a 13-bit Barker coded pulse, baud length=20 msec, but the E-region mode uses a 5-msec IPP whereas the Spread F mode uses a 10-msec IPP to sample a greater unambiguous range (up to 1500 km). The internet to the system has not been reliable for a variety of reasons but the system was able to send data intermittently during the period. A few plots are shown in Figures 61-63, highlighting the types of echoes observed, which range from meteors, daytime electrojet, to sporadic E, F-region layers and F-region bubbles. Figure 61 shows types of daytime echoes observed; with electrojet shown on the left and meteor echoes on the right. Note that the electrojet is not seen every day, as expected given the location ~4° MLAT. The plots in each panel show the raw SNR, weighted average Doppler and the integrated spectrum of the SNR data. Figure 62 illustrates post-sunset echoes. Post sunset-echoes frequently show sporadic E and weak F-region bubble signatures; the overall duration of F-region echoes is not as long as expected. Sensitivity may be an issue in the topside (no echoes observed $z > \sim 600$ km). Figure 63 includes additional post-sunset echo types with strong E-layer and quasi-stable scattering layer at ~300 km altitude. We compare the 300 km echoes with observations at Jicamarca where a bottomside scattering layer is frequently involved in association with bubble development. At Bahir Dar, no cases have been observed where the 300 km layer leads to subsequent bubble genesis.

Radar Performance

One concern is the relatively low SNR on F-region bubble echoes and essentially no echoes have been observed above about 600 km. The phasing of the antenna elements may not be as precise as desired and this may be resulting in less gain than calculated. Other issues impacting performance could include transmitter/antenna impedance mismatch and transmitter power below 2 kW per channel. Just a few dB will materially impact the results so we want to optimize the system as much as possible. BC plans to modify the NEC model of the antenna to include the actual measured impedances and phases at each antenna (Field Fox, portable NA) and see how gain and beam forming are affected. Data were collected from the array during the installation period in Nov 2015 and are presented here.

Figure 59 shows the Blue Nile radar antenna configuration. It includes 64 yagi antennas arranged in an 8x8 array with alternating rows staggered by 1.875 meters to improve the antenna pattern and reduce grating lobes during E-W beam steering. The array is fed by 8 low-loss feed cable (LMR-600 from the power amplifier to a power divider at the center of each row (N-S). From the power dividers each antenna is fed through a 17-m length of LMR-400 connected to a variable length of LMR-240 cable that connects directly to the antenna feed points via ring terminals. The length of the LMR-240 (vel. Factor = 0.84) cables increases from the southernmost end of each row to the northernmost end, increasing by 42-cm for each antenna.

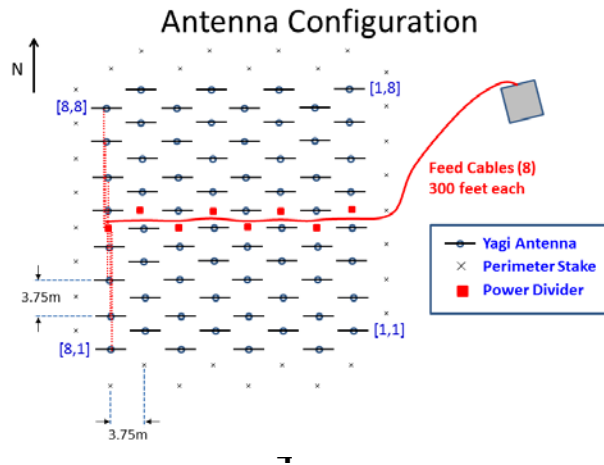


Figure 59. Blue Nile Radar Antenna Configuration

The length is equivalent to a 30° phase shift that tilts the beam approximately 8° to the north where it is perpendicular to geomagnetic field lines, maximizing the scattered return power from coherent field-aligned irregularities associated with Spread F. For purposes of identifying individual antennas, the origin of the array is chose to be the southeast corner where antenna [1,1] is labeled in the figure.

Figure 60 includes the system diagram showing the primary components and connections of the Blue Nile Radar together with a photograph of the installed system in operation. Figures 61, 62 and 63 illustrate daytime and post-sunset echo types observed by the Bahir Dar Radar.

System Diagram

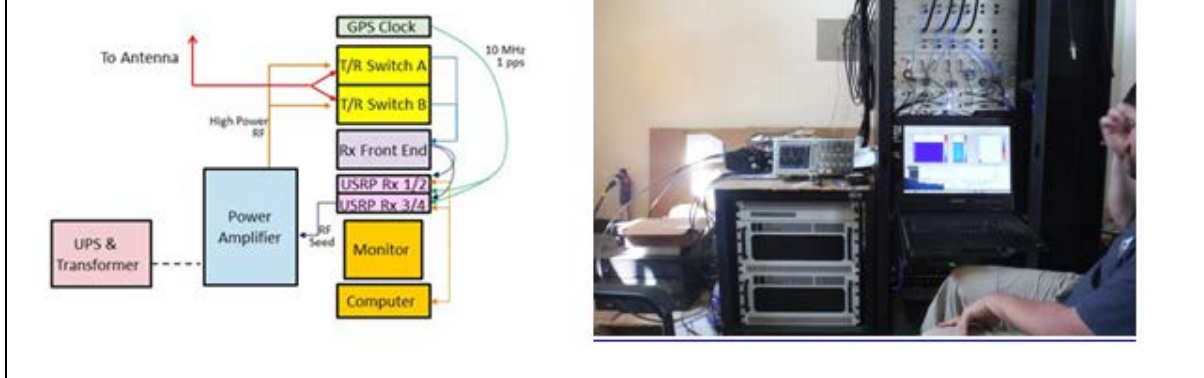


Figure 60. System Diagram and Photograph of the Blue Nile Radar System in Bahir Dar

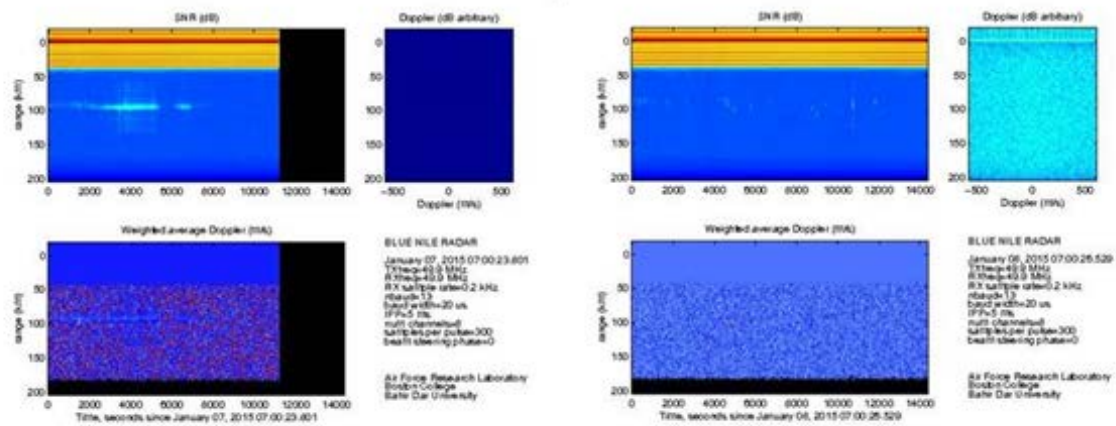


Figure 61. Types of Daytime Echoes Observed by the Bahir Dar Radar

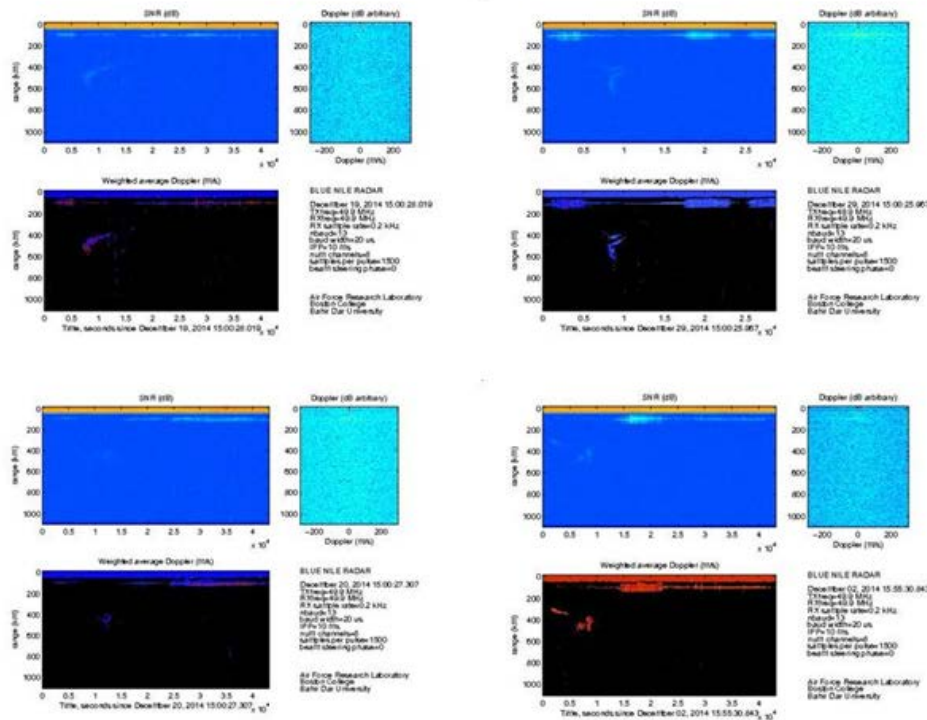


Figure 62. Post-sunset Echoes Recorded by the Bahir Dar Radar

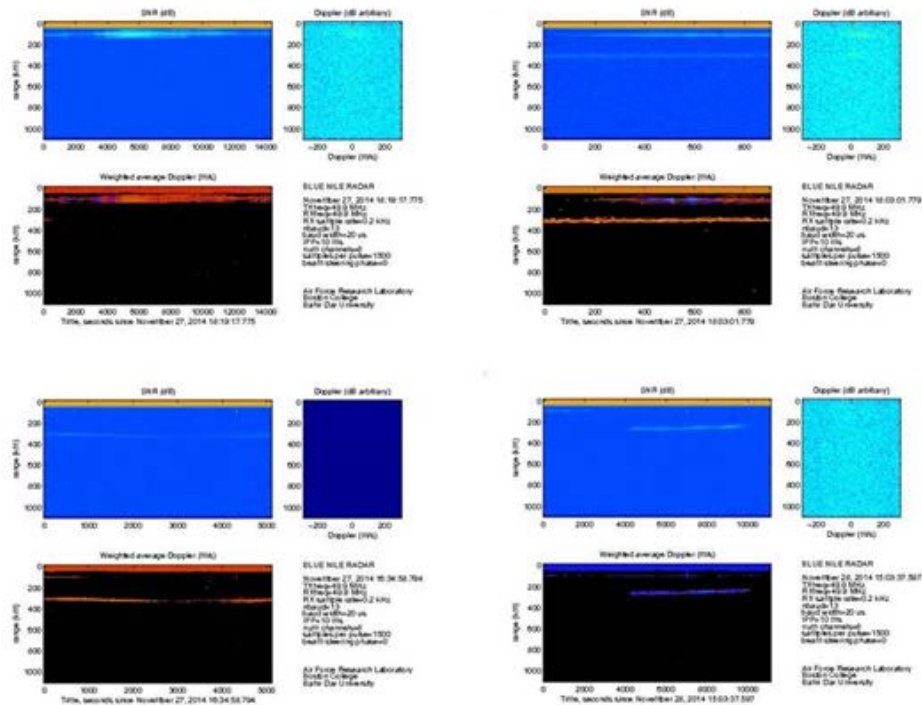
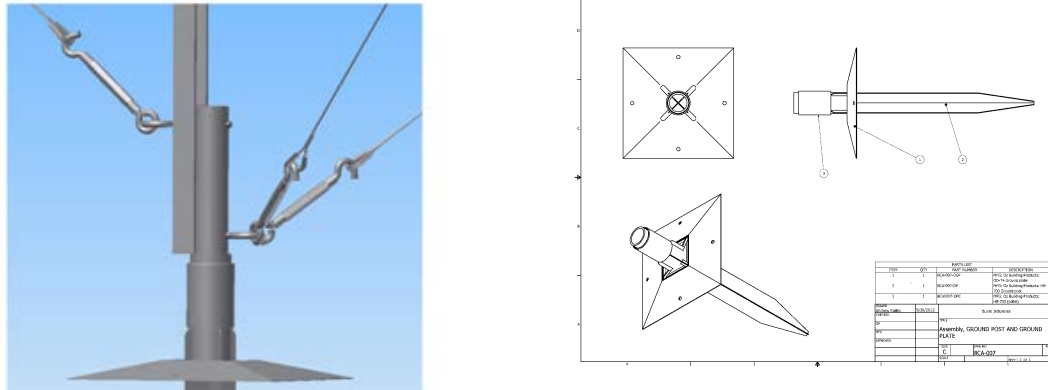


Figure 63. Additional Post-sunset Echoes Recorded by the Bahir Dar Radar

First we consider the performance of an individual antenna. The antennas were custom constructed to AFRL specification by Burns Industries Inc., in Nashua, NH. The specifications were based on the design of a commercial 6-element yagi antenna (Hy-Gain VB66-DX) linearly scaled from an original operating frequency of 50.1 MHz to 49.9 MHz as desired for BNR. A single antenna is predicted to have 12.5 dBi gain. Burns modified the design significantly to improve both manufacturability and ease of construction in the field, reducing the number of individual parts relative to the Hy-Gain unit by nearly a factor of five. More details on the antenna and the anchor/guying system (also designed and provided by Burns) can be seen in Figures 64-67. The left panel of Figure 64 shows the details of guy points and base plate of the antenna. The right panel of Figure 64 shows “Oz post” and cap used as the base for each antenna. Ground conditions in the antenna field vary seasonally from dry to standing water so the stability of the base plates was a significant concern. The antennas are guyed to nearest neighbors except around the perimeter where angle-iron stakes are used as needed. Figure 65 shows the upper guy point details with the side view on the left and the front view on the right. Figure 66 illustrates the antenna elements in the upper panel and the mast dimensions in the lower panel. The diagrams in Figure 67 show the shorting bar in the left panel and the match tube used in the beta match network on antennas.

Base Plates & Guy Points Detail



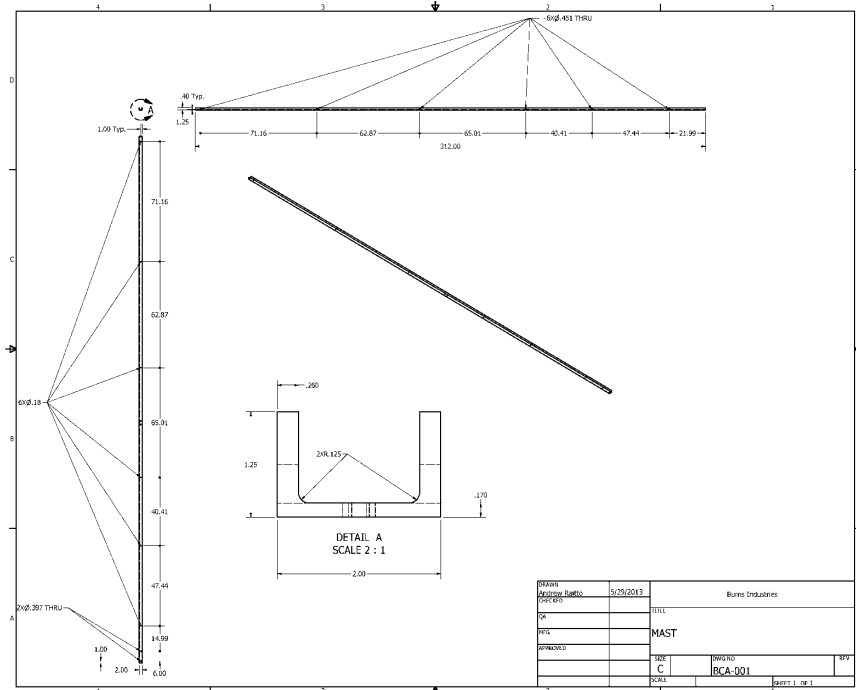
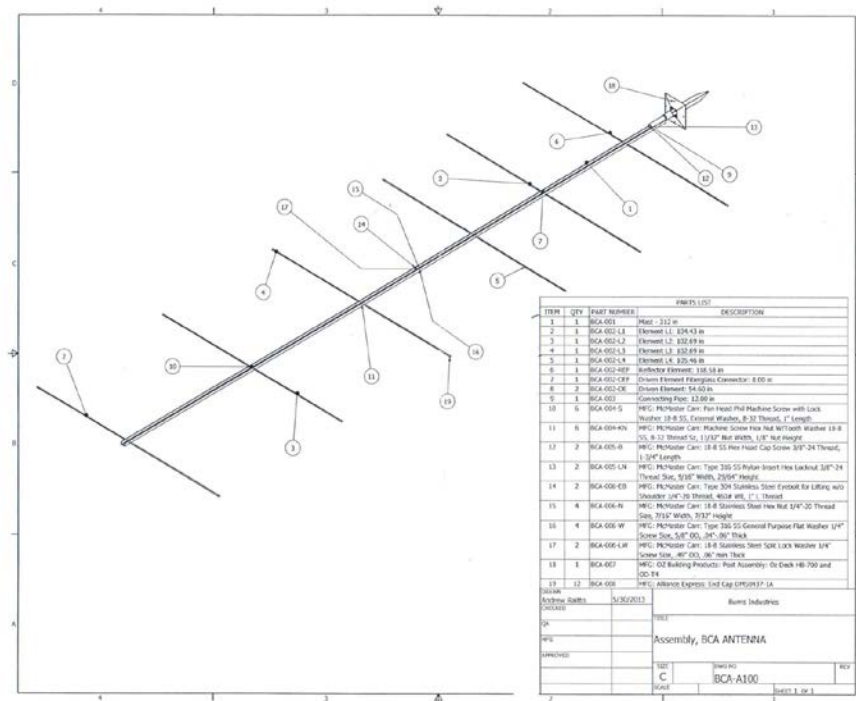


Figure 66. Antenna Elements and Mast Dimensions

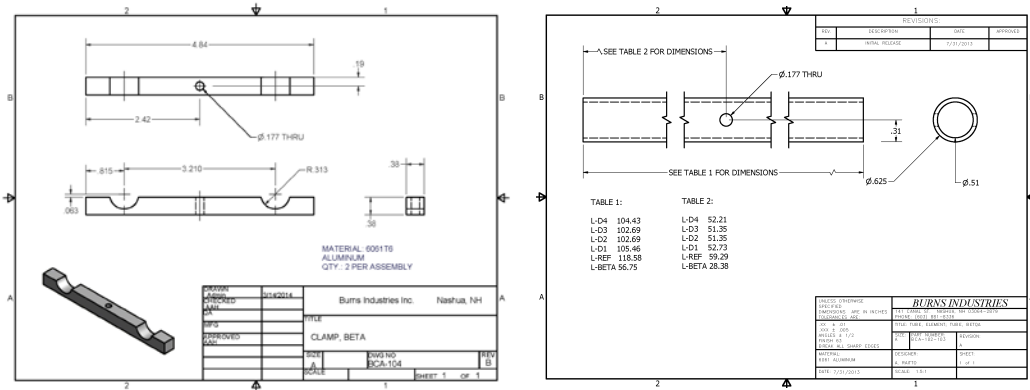


Figure 67. Shorting Bar and Match Tube used in Beta Match Network on Antennas

The electrical properties of an individual antenna are shown in Figure 68. The antenna tested was selected at random from a lot of production antennas at Burns Industries in Hollis, NH. The figure shows the voltage standard wave ratio (VSWR) and the Smith chart representation of the complex impedance measured with a network analyzer over a frequency range of 42.4-57.4 MHz. The match appears to be outstanding with VSWR \sim 2.02 and impedance of $S = 49.3 - j0.1 \Omega$ at the desired frequency of 49.9 MHz; the results were obtained with a shorting bar separation distance of 16.875 inches on the beta match used for the antennas.

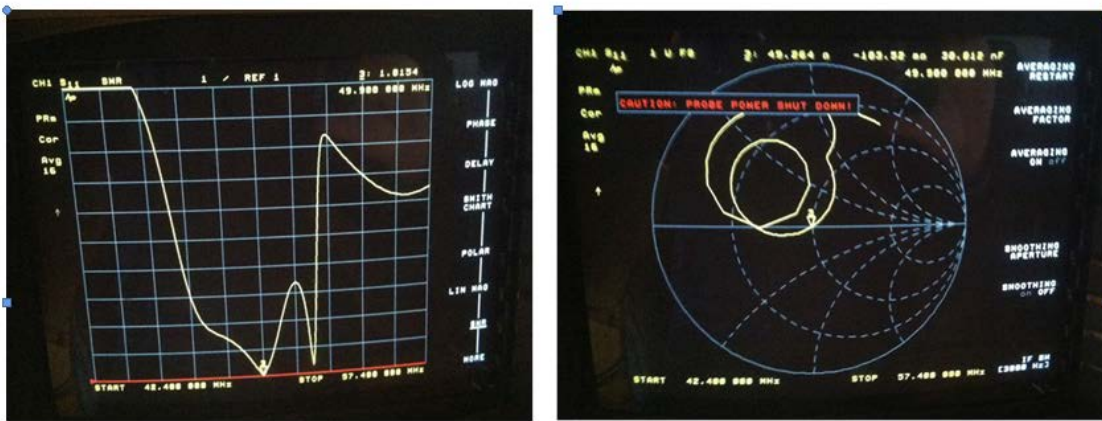


Figure 68. VSWR and Complex Impedance Results for a Production Antenna Tested Prior to Shipping

The impedance of the given antenna will change when other antennas are placed in the near field and the impedance of antennas measured in the Bahir Dar array varied significantly. Using the Field Fox meter LMR-400 test cable at the input to the 8-way power divider that feeds each antenna on a given row; from the power divider a 17-m length of LMR-400 cable then connects to the LMR-240 feed line connected directly to ring terminals on the antenna. Thus the measurements include a variable length cable that increases by $\lambda/12$ effective length with each antenna advancing along a row. The network analyzer will measure phase corresponding to twice the change in effective cable length of course (two way measurement), so the delta between each antenna is effectively $\lambda/6$ radians. If the phasing was done correctly, for example, the 1st antennas in each row should have the same characteristics as the 7th antennas in each row; similarly, the 2nd and 8th antennas in a row should be consistent. Let us now

consider the phases for the antennas measured in the array after installation and depicted in Figure 69. The ridged phase structure evident as one moves across the array corresponds to the physical off-set in alternating rows designed to provide a more uniform antenna pattern when the beam is electronically steered (see Figure 59). The designed phase difference between each antenna on a given row should be 60° when measured in this manner. The measured differences are plotted in Figure 70 which shows that the average phase difference is about 60° . However, there are significant variations from antenna to antenna. Note that to achieve the desired $\sim 8^\circ$ northward tilt, the intended differences should be 60° as measured. As noted in Figure 69, the 4th antenna in row 6 (red arrow) is an outlier.

A number of the phase deviations are on the order of 20° ; this corresponds to a physical cable length difference in LMR-240 of about 14-cm, with some being electrically shorter and some longer by this amount. Since the 17-m LMR-400 cables were cut to an identical electrical length using a network analyzer, the phase differences must arise from the power dividers, the LMR-240 feed cables, the antennas themselves or the connectors. AFRL indicated that they had checked the phase coherence of at least some of the power dividers before shipping. The feed cables, which vary in length from 0.5-m to 3.65-m, were cut and matched by physical length only. However, one would not expect 14-cm electrical variations in cables on the order of 1-m long. In the case of the 4th antenna in row 6 [6, 4], the phase difference is twice as much, approaching 30-cm difference from the expected electrical length of the cable. R. Todd Parris of AFRL checked this antenna and found that the physical feed cable length for this particular antenna was actually correct, 1.76-m as designed. The anomalous phase value measured on this antenna remains unexplained.

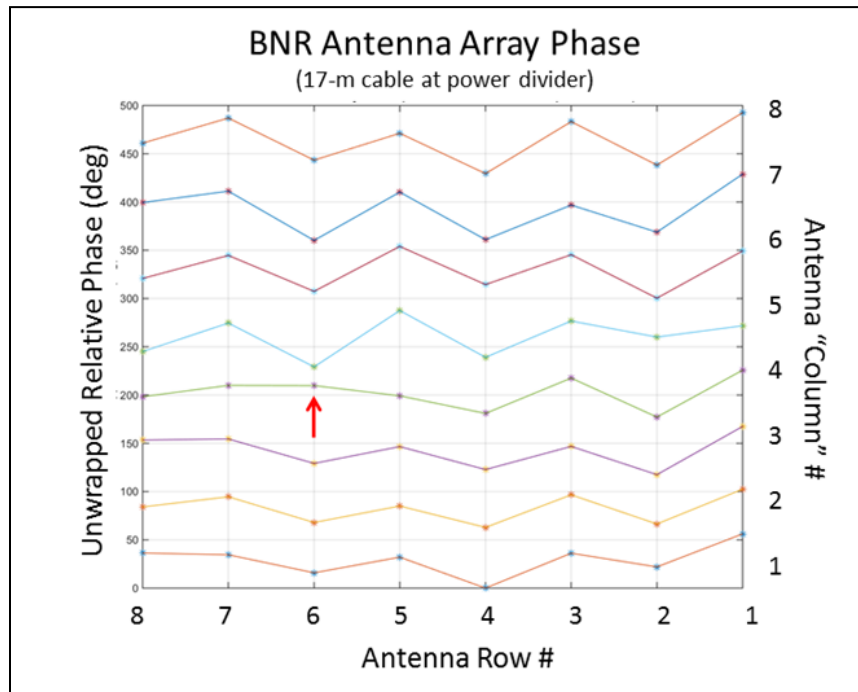


Figure 69. Antenna Phases Measured with a Network Analyzer at the Power Divider Input

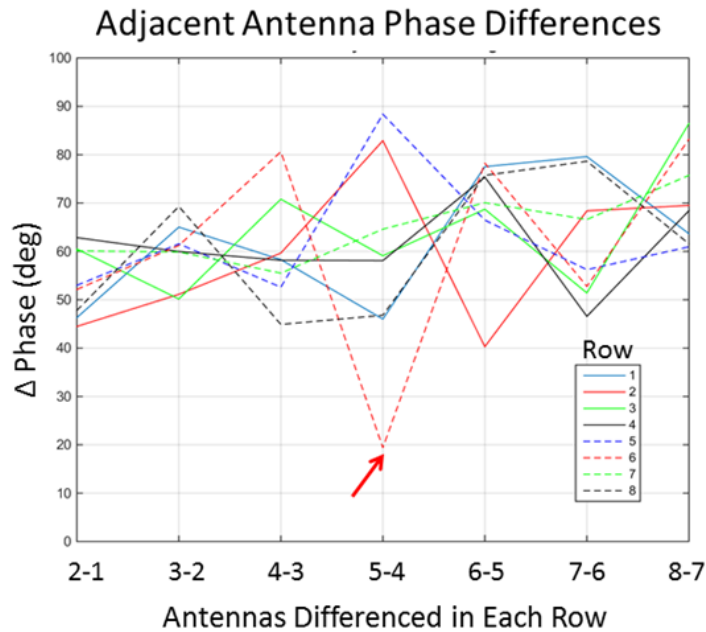


Figure 70. Phase Differences between Adjacent Antennas in the BNR Array

It is difficult to understand how individual antennas could contribute significantly to these phase variations, although installers did note that changes in the tightness of the connections of the feed lines and/or the matching network components could affect impedance measurements. The electrical properties of individual antennas and cables were not tested systematically during the installation period. If some of the variations are associated with the antennas, there are up to six spare antennas at the University in Bahir Dar. First we need to understand the extent to which the observed phase differences impact the antenna pattern of the array. This impacts performance in two ways. First, a random phase variation across the array will have the effect of “spoiling” the beam, essentially broadening and reducing the mainlobe gain. The second, and perhaps more significant, way the phase noise affects performance has to do with directionality. Recall that the 30° N-S phase shift was employed to tilt the beam northward to achieve perpendicularity to the magnetic field lines over a wide range of altitudes. It is extremely important to achieve perpendicularity as the radar cross section of the field-aligned irregularities maximizes near 90° relative to B and decreases >10 dB/degree as the relative beam angle decreases. The return radar power from these irregularities will thus decrease rapidly if the correct tilt is not achieved.

Another issue to consider is the impedance of the antennas when deployed as an array. Near-field interactions will typically modify the impedance measured relative to a “free-standing” antenna; the significance of those interactions depends on numerous factors but most critically the distance between adjacent antennas, 3.75-m along each row (perpendicular to elements; see Fig 59) and 4.2-m separation on center between adjacent rows (Fig 59). Given that the elements themselves are ~2.6-m in length, the tips of the elements on adjacent antennas are separated by only ~2.2-m, less than half a wavelength. The measured real impedance and VSWR for the array are shown in Figures 71 and 72, respectively. The measurements were performed on Nov 25, 2014 with a 15-inch shorting bar separation distance on all antennas; the separation distance was chosen, in fact, to minimize VSWR. (It should also be mentioned that the shorting

bar match assessment was conducted on a single antenna in the interior of the array and all antennas were subsequently adjusted to the same 15-inch separation settings). The measurements were performed at the same time as the phase measurements and thus reflect the inclusion of the varying length feed cables. As a result, the 1st and 7th and 2nd and 8th antennas in each row show similar characteristics as the varying phase path wraps the impedance around the Smith chart. What is clear is that the net impedance at the power divider inputs, fed at 50 Ohms from the transmitter lines, varies from 30-80 Ohms. Not surprisingly, the VSWR (Fig 72) reflects the mismatch. Recalling that a single free-standing antenna showed a VSWR of 1.02 when carefully tuned, the VSWR of the same antennas in the array varies from 1.4 to 1.8. Taking the mean as about 1.6, this implies a reflection coefficient of about 0.23 or about a 2 dB loss in power relative to a VSWR of unity.

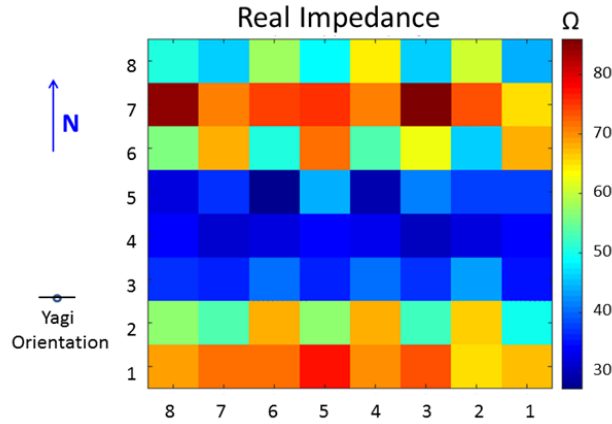


Figure 71. Real Impedance for each Antenna Measured on the BNR Array

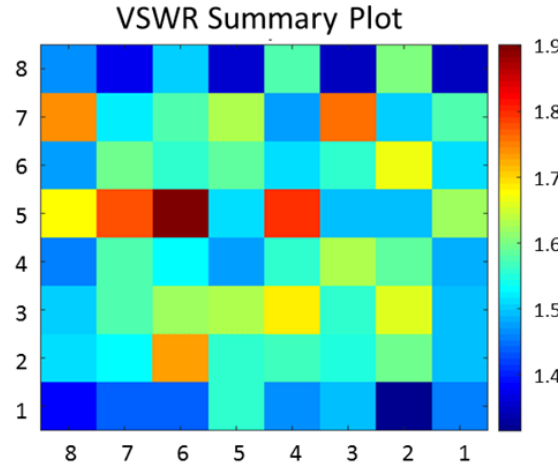


Figure 72. Voltage Standing Wave Ratio (VSWR) of the BNR Array

Another consideration in improving the performance of the BNR is the output power. The Tomco 8 channel x 2 kW (16 kW total) power amplifier input is a low-level signal supplied by the USRP X-300 software defined radios. Nominally the Tomco will provide 2 kW when fed with a 0 dBm signal. The output signal level from the USRP X-300, however, is a bit below that

level, 2.25 dB below on at least one channel. This translates directly to lower output power. The output power from each channel on the power amplifier was measured and the results are shown in Table 1. The total power out is actually less than 10 kW; the transmitted power as a whole is about 2.2 dB below the planned 16 kW.

Blue Nile Radar (BNR) Summary

The Blue Nile Radar installation in Bahir Dar, Ethiopia was successfully completed in November 2015. The radar is a sophisticated new system consisting of an 8 x 2 kW transmitter coupled to an 8 x 8 yagi array capable of E-W beam steering perpendicular to the magnetic field. The transmitted waveforms and receive systems are fully digital and offer a tremendous level of flexibility for complex coding schemes. Like any complex new system a number of issues remain to be resolved following the initial installation period. We have noted here a concern about the sensitivity of the radar for characterizing equatorial plasma bubbles. In fact, there is at present considerably more data available to reduce and analyze than was available at the time this report was written. Thus, the first order of business for developing an improvement strategy is to analyze all available data to assess the overall performance and correlate the results with observed scintillation activity. The second step in assessing expectations for the system would be to understand the impact of the existing defects in the array phase/impedance on the overall antenna pattern. AFRL constructed a detailed description of the array for analysis in the NEC modeling code. BC modified the description to include the actual terrain effects. A further modification is needed to include the observed phase differences in individual antennas. This would inform users about the performance of the current system.

However, it is clear from the measurements that have been done that several issues should be addressed in terms of the tuning the phased array and improving output power. A thorough examination of each component in the RF chain should be done to establish the coherence of the system. This essentially means measuring the phase and impedance of each component including antennas and feed lines carefully and systematically. Particularly the feed lines with ring connectors should be tested. For cases where significant deviations from the expected result are found, remedies should be implemented. In some cases tuning individual antennas may provide relief.

Though quality control processes were employed, numerous people were involved in the construction of the antennas and erection of the antennas. Each step in the complex development and assembly process is subject to errors of perhaps a few degrees of phase; in some cases these errors may be additive and collectively combine to give unacceptable variances from the design. Opportunities for bias may be introduced at this stage depending on differences in individual's application of instructions or techniques. Phase errors in the receive chain may also be present and as yet undetected. The digital receiver (RX) front end, for example, showed relative phase differences of up to 10 degrees across its eight channels. Long term a calibration procedure will be needed.

We should not forget this is a research system, not a mass production radar. Inevitably such a system requires "break-in" time to identify and resolve issues and reach its full operating potential. We have no doubt that this will be the case with the BNR. Unfortunately, resources were exhausted after the initial installation period, and no new support has been available to continue this process and allow this confidence to be realized. An essential ingredient to the process, familiarity through day-to-day use of the system, is sorely lacking. The BNR hosts at Bahir Dar University have both interest and motivation to work with the radar, but they lack

experience with both hardware and software. We hope that both AFRL and Boston College can obtain sponsorship in the near future to continue to develop and improve the BNR to perform exciting science relevant to United States Air Force (USAF) needs.

3.4 Operations and Maintenance of SCINDA

Efforts under this contract also supported the operation and management of ionospheric instruments that have been deployed around the world in support of Air Force Weather Agency (AFWA) interests in ionospheric monitoring and prediction. The work performed by Boston College in support of this effort included the purchase and installation of a number of diagnostic instruments; the initiation and routine operation of remote sites; the set-up for data transmission from remote sites to a server at Boston College on a real time basis; the provision for off-line data backup systems, and data storage and real-time data processing. An important element of this support also included full-time technical support to troubleshoot, repair and replace failed components and equipment. Support was also provided for maintenance of equipment, logistical support for remote hosts and for calibration and validation of the observables collected by the ionospheric instruments. The instruments supported included GPS receivers, software digital radio receivers, triaxial fluxgate magnetometers advanced fully digital ionosondes and other radio and optical diagnostics. These instruments have formed distributed observatories that are able to monitor the ionosphere over large areas of the globe. The non-local multi diagnostic measurements have been used in the scientific report of this contract. They have made it possible to study ionospheric processes such as the equatorial anomaly effects on density distribution and on the stabilization of plasma irregularities and the efficiency of gravity waves on seeding. Numerous studies have been performed with TEC and scintillation from the network of receivers supported under this contract. In addition, these observatories provided new tools to understand the day-to-day variability and stability of the low latitude ionosphere and to make more accurate forecasts of scintillation at key locations in different regions of the world as part of the Scintillation Network Decision Aid (SCINDA) sensor network.

An important function of this network of instruments was to supply real-time data to the Air Force Weather Agency (AFWA) to enable the agency to continue to provide regional specification and nowcasts of scintillation activity. The network that we have supported consisted of at least 50 sites worldwide. All of these sites are equipped with at least one GPS receiver, several are equipped with additional instruments including: UHF SATCOM receiver, a second GPS receiver, software digital radio receiver, triaxial magnetometer, LEO beacon receiver, and all-sky optical camera. A few sites have ionosonde or radar instruments as well. The data from each of these instruments is collected on-site using a personal computer (PC), and delivered in real time over an internet connection to AFRL and/or Boston College where the data is processed and then sent to AFWA. Figure 73 shows the location of the GPS receivers that were operational during the period of performance of this contract.



Figure 73. Location of GPS Receivers Supported under this Contract

The support for this network was continuous and extensive. To operate these instruments and collect data in real time, electrical power and internet services were required. Many of the instruments required extensive cabling to one or more antennas, which were periodically maintained and replaced. While the instruments were designed to operate as autonomously as possible, an onsite person was needed to monitor and provide occasional troubleshooting. Boston College personnel monitored data flow and quality on a daily basis, maintained communication with all onsite hosts of the equipment and assisted with computer maintenance and software upgrades. Some upgrades and repairs were performed remotely if the internet connections were reliable and local Information Technology (IT) policies permitted remote access to the site. Without remote access, BC personnel guided the onsite host to perform the necessary maintenance. Our support also included occasional travel to the remote sites, cost of the equipment, shipment of equipment and customs fees. In all cases, U.S. Export Control Regulations were strictly followed.

Under this contract, a data server was also acquired, set-up and continually maintained to collect the data from the remote sites and to make it available to AFRL and AFWA. Short term outages at remote sites were resolved remotely by providing instructions to on-site support and/or replacing broken or faulty components; data was assessed for quality and archived for future use. Responsibilities for developing, fielding and maintaining this network were truly shared with AFRL during most of the period of performance. This partnership was extremely effective in building an extensive low latitude sensor network around the globe. AFRL and NS jointly developed new sensor technologies. AFRL led the establishment of new sites in the network while BC focused on maintaining and sustaining continuous real-time data flow and product support.

The extent of that partnership is evident in the simplified depiction of the data flow shown in Figure 74. Data was pushed from the sites onto a BC server outside the University firewall. After some processing and formatting, the data were fetched from a dot-mil (NIPR net) server named IVY hosted at Kirtland AFB by AFRL supported by BC. From IVY the data were pushed to the WPMDS-3 front door by special permission from AFWA, who could then ingest the data for real-time scintillation nowcast products. The data transfer approach employed here was very successful for handling the unclassified scintillation and TEC data types.

Operational Data Flow

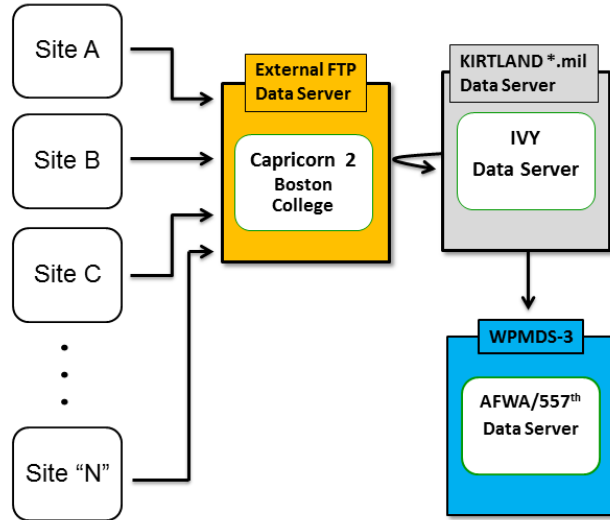


Figure 74. Simplified Diagram Showing Data Flow in the Operational Architecture

3.4.1 Sites and Equipment. The map in Figure 73 includes 55 sites and gives an indication of the locations supported under the contract, but it does not tell the whole story. While some of the sites shown are no longer functioning for a variety of reasons, all of them required some level of support during the period of performance for this task. Moreover, there are approximately 20 Low Latitude Ionospheric Sensor (LISN) sites not shown on the map that are affordably leveraged for operational support. These ancillary sites, primarily located in South America, were established with NSF sponsorship but have since been successfully employed to support AF products at very incremental cost.

As the map makes evident, the sites are frequently located in regions of sub-standard infrastructure relative to American norms, and siting sensors well constitutes a significant challenge. Wherever possible and accessible, US government sites were used to exploit reliable power and network. However, as network certification and accreditation (C&A) controls grew increasingly stringent, the prospects of access to government networks diminished and soon only sites with open network access were sought. These primarily consisted of universities and sometimes foreign government institutions, such as meteorological stations, mapping or space agencies. The primary sensor system, a Novatel GSV 4004B receiver, antenna and data acquisition system was relatively inexpensive at less than \$10K total and the paradigm was to populate as many sites as possible in a given region of interest. The NovAtel GPS system, depicted in Figure 75, is a commercial system GPS receiver system that has been installed at many of the SCINDA sites. Boston College developed custom software for the NovAtel system that enabled the system to operate reliably and robustly – even in a less than ideal environment with minimal on-site support.

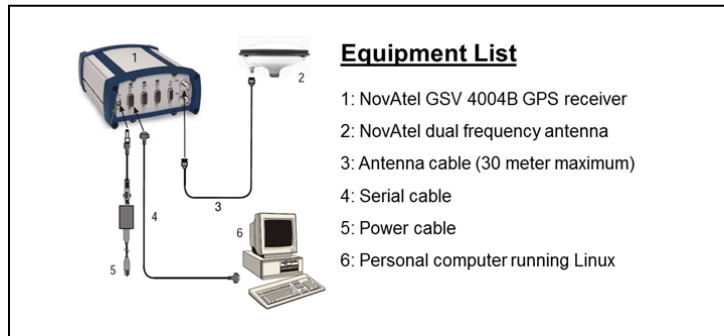


Figure 75. NovAtel GPS Sensor System: Workhorse of the SCINDA Network

A key feature was the development of custom Linux software that improved the quality of the recorded data relative to the commercial-off-the-shelf (COTS) software and further enabled remote network access and control of the system. This achievement was critical to enabling reasonable maintenance of more than 50 remote sites for a few hundred thousand dollars each year. One could not hope to visit each site even once per year (indeed, one would not hope to visit each site annually!), and remote access allowed BC subject matter experts to monitor, troubleshoot and sometimes repair faulty systems. More typically, access enabled BC to issue very specific instructions to on-site personnel to take corrective actions. While the NovAtel GPS systems are by far the most prolific in the SCINDA network, numerous other types of equipment were required to satisfy the needs of the growing network, most notably hardware for geostationary VHF beacon (UHF SATCOM) beacon receivers. A more complete description of the equipment purchased under the subject contract, as well as its last known location, can be found in the Appendix. Of the more than 250 items listed, just under one half were shipped directly to AFRL/RVBX, usually for off-site deployment and further evidence of the close working partnership between AFRL and BC on this task.

3.4.2 Performance. Given the circumstances under which the receivers were deployed—poor infrastructure and limited familiarity with the site host—it was not expected that every site would be highly successful. Whereas the cost of establishing a single robust, reliable site in many locations would be quite high, a low cost “ubiquitous installations” approach yielded cost-effective improvements to the overall performance of the network. Another term for the same concept might be, “Reliability Through Redundancy”. The benefits of this approach are illustrated remarkably well in the sequence of Figures 76-87, which show real-time performance statistics for 2012-14 for station groupings that represent a particular longitude sector. The simple idea is that if one has a few stations in a given region there is a higher likelihood that at least one of them will be operating at any given time than if there is only one station in the same region. Stations with mediocre individual performance statistics might collectively provide a much higher level of coverage under the assumption that their individual outages are not correlated. Thus, while no specific station is guaranteed to be available, monitoring of the region of interest can still be assured for the user.

Figures 76-87 show availability results region-by-region from the last three years of the network’s supported operation. Except for Central Africa, which truly is a dark and difficult place, every longitude sector enjoys at least 90% uptime with respect to regional coverage. This performance is undoubtedly much better than the statistics maintained by AFWA that probably

include sites that were non-viable years ago as they have struggled to remain current with the new sites available in recent years. Nevertheless, we have complete confidence in these assessments as they are derived from the real-time database. The results show that consistency across the globe can be achieved within a reasonable budget; one could easily spend as much trying to maintain a small number of individual sites at high reliability with a fraction of the longitude coverage. However, with the experience BC now possesses we believe that a modest annual investment could significantly improve the performance of 60% of the existing sites, such that overall uptime and coverage would improve. The resolution and reliability of scintillation nowcasts improve measurably when multiple sensors are active in a region, and we believe it is possible to achieve this goal while still satisfying affordability considerations. Hopefully it will be possible to find support to demonstrate these improvements in the near future.

Note that Figure 76, 77 and 78 include sites that are part of the Low-latitude Ionospheric Sensor Network (LISN). Figure 81 shows that Central Africa is particularly disadvantaged. A completely autonomous system, such as one with solar panels for power and 3G data transfer, is the best hope for success. Figure 86 illustrates the benefits good infrastructure and on-site support that is available in the Central Pacific region.

Western South America

Santa Marta	11.25N	285.78E
Bogota:	4.64N	285.92E
Piura	5.17S	279.36E
Ancon:	11.77S	282.85E
Puerto Maldonado	12.58S	290.81E
Antofagasta:	23.68S	289.59E



2012: Santa Marta, Colombia 72.41%	Bogota, Colombia 74.90%	Piura, Peru 67.96%	Ancon, Peru 93.34%	Puerto Maldonado, Peru 63.47%	Antofagasta, Chile 0%	C
2013: Santa Marta, Colombia 5.15%	Bogota, Colombia 76.54%	Piura, Peru 60.91%	Ancon, Peru 63.09%	Puerto Maldonado, Peru 66.97%	Antofagasta, Chile 0%	C
2014: Santa Marta, Colombia 0%	Bogota, Colombia 57.96%	Piura, Peru 86.06%	Ancon, Peru 44.75%	Puerto Maldonado, Peru 53.00%	Antofagasta, Chile 0%	C

Figure 76. Collective Availability for the Circled Sites in Western South America

Central South America

Villegas	35.03S	296.99E
Boa Vista	2.83N	299.31E
Corrientes	27.47S	301.17E
Cuiaba:	15.07S	303.93E
Dourados	22.19S	305.07E
Santarem	2.43S	305.27E



2012: Villegas, Argentina	Boa Vista, Brazil	Cuiaba, Brazil	Corrientes, Argentina	Santarem, Brazil	Dourados, Brazil
78.11%	91.45%	95.97%	80.31%	44.13%	67.11%
2013: Villegas, Argentina	Boa Vista, Brazil	Cuiaba, Brazil	Corrientes, Argentina	Santarem, Brazil	Dourados, Brazil
71.2%	56.92%	72.54%	68.50%	53.88%	80.63%
2014: Villegas, Argentina	Boa Vista, Brazil	Cuiaba, Brazil	Corrientes, Argentina	Santarem, Brazil	Dourados, Brazil
92.41%	68.44%	80.05%	63.74%	70.79%	79.40%

Figure 77. Collective Availability for the Circled Sites in Central South America

Eastern South America

Palmas:	10.28S	311.67E
Brasilia:	15.76S	312.13E
Cachoeira:	22.70S	314.99E
SaoLuis:	2.59S	315.79E
Ilheus:	14.80S	320.83E
Natal:	5.84S	324.79E

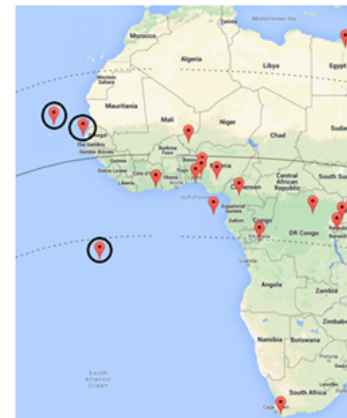


2012: Palmas, Brazil	Brasilia, Brazil	Cauchoeira Paulista, Brazil	Sao Luis, Brazil	Ilheus, Brazil	Natal, Brazil
54.76%	49.45%	30.19%	85.64%	98.85%	94.02%
2013: Palmas, Brazil	Brasilia, Brazil	Cauchoeira Paulista, Brazil	Sao Luis, Brazil	Ilheus, Brazil	Natal, Brazil
0%	28.51%	86.81%	76.82%	78.67%	97.03%
2014: Palmas, Brazil	Brasilia, Brazil	Cauchoeira Paulista, Brazil	Sao Luis, Brazil	Ilheus, Brazil	Natal, Brazil
0%	83.13%	95.75%	64.56%	96.88%	98.63%

Figure 78. Collective Availability for the Circled Sites in Eastern South America

Atlantic Ocean/ West Coast of Africa

Cape Verde: 16.73N 337.06E
Dakar: 14.68N 342.54E
Ascension: 7.98S 345.59E



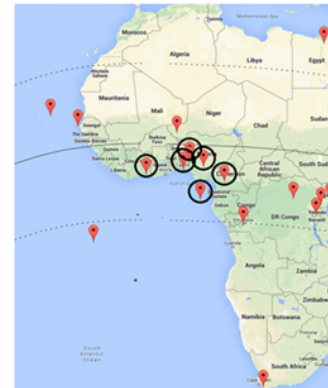
2012: Cape Verde 78.57%	Dakar, Senegal 26.23%	Ascension Island 95.28%	Cumulative Atl <u>99.40%</u>
2013: Cape Verde 94.42%	Dakar, Senegal 81.64%	Ascension Island 97.90%	Cumulative Atl <u>99.57%</u>
2014: Cape Verde 98.53%	Dakar, Senegal 49.10%	Ascension Island 97.39%	Cumulative Atl <u>99.79%</u>

Figure 79. Collective Availability for the Circled Sites in the East Atlantic/West African Region

West Central Africa

Abidjan:	5.34N	356.01E
Lagos:	6.52N	3.39E
Ilorin:	8.48N	4.67E
S Tome & Principe:	0.34N	6.74E
Nsukka:	6.86N	7.41E
Yaounde:	3.52S	11.31E

- Subset of sites well positioned for overlapping coverage.

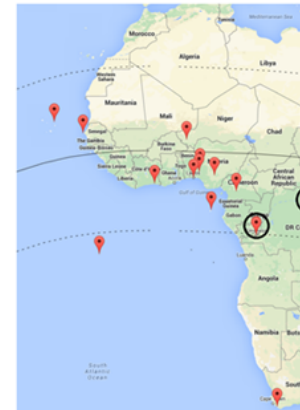


2012: Abidjan, Ivory Coast	Lagos, Nigeria 0%	Ilorin, Nigeria 73.48%	Sao Tome & Principe 31.16%	Nsukka, Nigeria 2.51%	Yaounde, Cameroon 82.17%
2013: Abidjan, Ivory Coast	Lagos, Nigeria 0%	Ilorin, Nigeria 0%	Sao Tome & Principe 20.53%	Nsukka, Nigeria 0.38%	Yaounde, Cameroon 0%
2014: Abidjan, Ivory Coast	Lagos, Nigeria 77.30%	Ilorin, Nigeria 0%	Sao Tome & Principe 0%	Nsukka, Nigeria 3.92%	Yaounde, Cameroon 4.68%

Figure 80. Collective Availability for Circled Sites in West Central Africa

Central Africa

Brazzaville: 4.28S 15.25E
 Kinshasa: 4.42S 15.31E
 Kisangani: 0.51N 25.21E
 Butare: 2.61S 29.74E

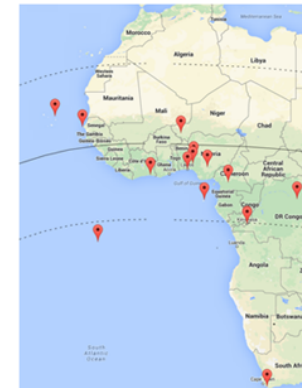


2012: Brazzaville, Congo	Kinshasa, Congo	Kisangani, Congo	Butare, Rwanda	Cumulative
43.76%	57.62%	0%	7.47%	<u>77.41%</u>
2013: Brazzaville, Congo	Kinshasa, Congo	Kisangani, Congo	Butare, Rwanda	Cumulative <u>77.41%</u>
0%	1.09%	0%	30.83%	<u>31.52%</u>
2014: Brazzaville, Congo	Kinshasa, Congo	Kisangani, Congo	Butare, Rwanda	Cumulative <u>31.52%</u>
0%	10.80%	0%	76.76%	<u>73.13%</u>

Figure 81. Collective Availability for the Circled Sites in Central Africa

East Africa

Helwan:	29.86N	31.32E
Kampala:	0.37N	32.56E
Kisumu:	0.00	34.60E
Nairobi:	1.27S	36.81E
Addis Ababa:	9.03N	38.42E
Zanzibar:	6.23S	39.21E



2012:	Helwan, Egypt	Kampala, Uganda	Kisumu, Kenya	Nairobi, Kenya	Addis Ababa, Ethiopia	Zanzibar, Tanzania
	43.81%	78.18%	39.69%	89.73%	55.61%	47.99%
2013:	Helwan, Egypt	Kampala, Uganda	Kisumu, Kenya	Nairobi, Kenya	Addis Ababa, Ethiopia	Zanzibar, Tanzania
	45.02%	67.16%	69.09%	0%	48.70%	22.07%
2014:	Helwan, Egypt	Kampala, Uganda	Kisumu, Kenya	Nairobi, Kenya	Addis Ababa, Ethiopia	Zanzibar, Tanzania
	32.39%	45.19%	75.57%	12.75%	51.65%	77.18%

Figure 82. Collective Availability for the Circled Sites in East Africa

Southwest Asia

Rajkot: 22.30N 70.80E
Diego Garcia: 7.30S 72.42E
Tirunelveli: 8.67N 77.81E
Kolkata: 22.58N 88.37E

- No data from Diego Garcia due to C&A



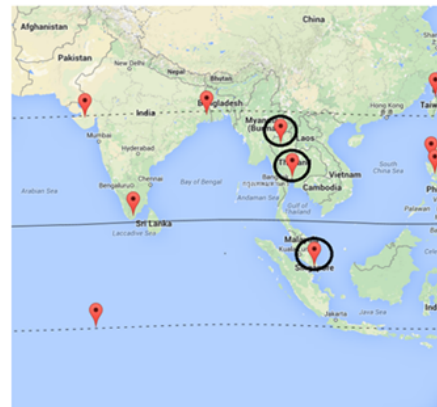
2012: Rajkot, India	Tirunelveli, India	Diego Garcia	Kolkata, India	Cumulative C
41.49%	80.77%	0.00%	79.35%	<u>93.95%</u>
2013: Rajkot, India	Tirunelveli, India	Diego Garcia	Kolkata, India	Cumulative C
15.90%	92.71%	0.00%	67.77%	<u>96.56%</u>
2014: Rajkot, India	Tirunelveli, India	Diego Garcia	Kolkata, India	Cumulative C
39.71%	85.41%	0.00%	93.42%	<u>99.09%</u>

Figure 83. Collective Availability for the Circled Sites in Southwest Asia

Indochina

Chiang Mai: 18.80N 98.95E
Bangkok: 14.08N 100.61E
Singapore: 1.46N 103.83E

- GPS and UHF data from Chiang Mai have same reliability 2012, but UHF has quality issue.
- No data from Singapore due to lack of support and C&A issues



2012: Chiang Mai, Thailand	Bangkok, Thailand	Singapore, Malaysia	Cumulative Indochina
84.80%	79.69%	0%	<u>96.35%</u>
2013: Chiang Mai, Thailand	Bangkok, Thailand	Singapore, Malaysia	Cumulative Indochina
66.65%	91.02%	0%	<u>97.05%</u>
2014: Chiang Mai, Thailand	Bangkok, Thailand	Singapore, Malaysia	Cumulative Indochina
37.05%	97.43%	0%	<u>98.55%</u>

Figure 84. Collective Availability for the Circled Sites in Indochina

Western Pacific

Baguio:	16.41S	120.58E
Manila:	14.63N	121.08E
Davao:	7.3N	125.40E
Taiwan:	24.98N	121.19E
Darwin:	12.54S	131.06E



- Internet needed at Baguio.
- Davao GPS showed reliability in 2012, but has multipath up to 60% elevation.

	Baguio, Philippines	Davao, Philippines	Manila, Philippines	Taipei, Taiwan	Darwin, Australia
2012:	0%	75.0%	72.05%	94.45%	80.18%
2013:	0%	0%	2.13%	96.84%	23.23%
2014:	0%	0%	0%	97.97%	71.95%

Figure 85. Collective Availability for the Circled Sites in the Western Pacific Region

Central Pacific

Kwajalein: 9.40N 167.47E

- True stand alone station, about 35 degrees longitude from nearest operating neighbor.
- Has history of reliability and excellent on-site support at a US government installation.

2012: Kwajalein,
Pacific Ocean
97.06%

Cumulative P. 1
97.06%

2013: Kwajalein,
Pacific Ocean
93.73%

Cumulative P. 1
93.73%

2014: Kwajalein,
Pacific Ocean
96.22%

Cumulative P. 1
96.22%

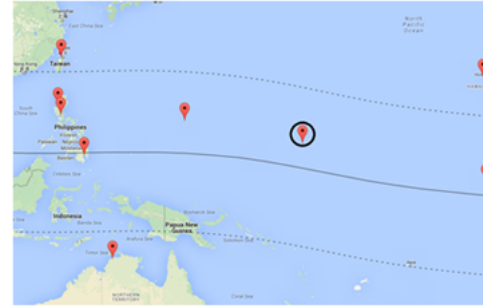
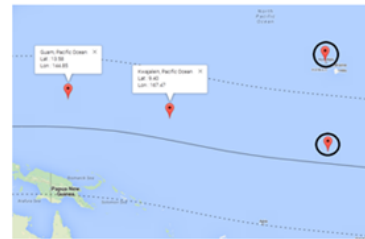


Figure 86. Collective Availability for the Circled Sites in the Central Pacific Region

Eastern Pacific

Wahiawa: 21.52N 202.01E
Christmas Island 2.00N 202.60E

- Wahiawa equipment installed mid 2012.
- About the same time, Christmas Island received equipment repairs/upgrades.



2012: Wahiawa, Hawaii 98.39%	Christmas Is, Pacific Ocean 47.73%	Cumulative P 2 <u>99.32%</u>
2013: Wahiawa, Hawaii 98.78%	Christmas Is, Pacific Ocean 82.55%	Cumulative P 2 <u>99.52%</u>
2014: Wahiawa, Hawaii 98.94%	Christmas Is, Pacific Ocean 50.28%	Cumulative P 2 <u>99.44%</u>

Disclaimer: Where the slides showed operational percentages for all 12 months of 2012, these are shown for the 6 months of that year.

Figure 87. Collective Availability for the Circled Sites in the Eastern Pacific Region

4.0 RESULTS AND DISCUSSION

This contract has addressed a number of studies supporting the goal to forecast the appearance and evolution of ionospheric irregularities and structures and to define their effects on Air Force Systems. Each study is described separately under Section 3 and is inclusive of the results and discussion on each topic.

5.0 CONCLUSIONS

The studies described in this report address a wide variety of topics on the observations, analysis and modeling of the low, middle and high latitude ionosphere; on the analysis, modeling and simulation of scintillation effects on DoD systems; on ionospheric sensor installations; and on the operation and maintenance of the SCINDA network. Although each of the studies described in Section 3 are inclusive of the conclusions of each study, we provide the following key points described in this report.

Re: 3.1 Observations, Analysis and Modeling of the Low, Middle and High Latitude Ionosphere

The study on *Observations of MSTIDs over South and Central America* [Valladares et al., 2015] provided regional maps of TEC perturbations associated with the TIDs that circulated throughout South and Central America and the Caribbean region on August 20 and 21, 2011. A group of TIDs, observed in the Caribbean region between 0 and 6 UT on August 21, 2011, were likely associated with primary AGWs. These waves were triggered within the region of the tropical storm Irene.

The investigation on *Near Midnight TEC Enhancements over South America* [Valladares and Chau, 2012] demonstrated that near-midnight TEC enhancements are formed by a receding equatorial anomaly driven by a reverse fountain effect acting in response to downward vertical drift.

The research effort on *Characteristics of TIDs using Small and Regional GPS Networks* [Valladares and Hei, 2012] presented calculations of the phase velocity, scale size, and angle of propagation of TIDs that are likely originated by gravity waves that are propagating in the north-western side of the South American continent. The values that were obtained using the SADM-GPS and a cross-correlation methods were consistent with values of medium scale TIDs observed by other authors.

The work on the *Statistics of TEC Depletions Observed over the South American Continent in 2008* [Seemala and Valladares, 2011] focused on the day-to-day variability of the TEC depletions over the South American continent for the entire year of 2008. Observations of depletions in this year of low solar activity show that the seasonal and longitudinal variability agree with *Tsunoda*'s hypothesis on the alignment of the sunset terminator and the local magnetic field lines.

It was discovered the existence of *The Tropical Ionization Anomaly* [Valladares and Eccles, 2014] that was observed over South and Central America and the Caribbean region and was characterized by anomalous plasma enhancements that develop over Central America during the June solstice and over the southern part of Brazil during the December solstice seasons. It was postulated and demonstrated by using numerical simulations, that the neutral wind, both the north-south and the east-west components, under the peculiar geometry of the magnetic declination across the South American continent acts accordingly to transport the plasma along the field lines and toward higher altitudes slowing down the recombination rate and producing an accumulation of plasma density during afternoon hours.

Polar Cap Patches Observed During the Magnetic Storm of November 2003 [Valladares et al., 2015] showed that their 630.0 nm airglow intensities can vary as much as 250 Rayleighs as they transit across the imager field of view. These authors used the GTIM model to investigate the effect of a downward neutral wind associated with a train of large-scale gravity waves to produce an increase in the intensity of the 630.0 nm airglow emissions.

Re: 3.2 Analysis, Modeling and Simulation of Scintillation Effects on DoD Systems

To predict the impact of ionospheric scintillation on DoD communications, navigation, and space radar systems it is often necessary to simulate the RF conditions under which these systems must operate. This involves physical modeling of the disturbed ionosphere followed by radio propagation techniques. A realistic simulation must account for the motion of the transmitter and receiver platforms, the drift and anisotropy of the irregularities, and the oblique

angle of propagation, all of which determine the scale sizes of the refractive index irregularities sampled by the radio wave.

Under this contract we have developed and validated phase screen algorithms to simulate RF conditions in highly realistic scenarios which take all of these aspects into account for space-to-ground [Carrano et al., 2012], ground-to-space [Caton et al., 2009; Carrano et al., 2012d], and space-to-space [Carrano et al., 2011] radio propagation scenarios. We applied these techniques to simulate scintillation impacts on tracking / FOPEN radar and SAR system. We have analyzed GPS observations during scintillation to characterize navigation degradation in terms of well-studied metrics of scintillation severity, namely the S_4 index and decorrelation time [Carrano et al., 2010]. Finally, we have developed two new techniques (CLM and IPE) for interpreting scintillation in the strong scatter regime [Carrano et al., 2012c] and mapping the effects to systems operating at frequencies other than those actually measured [Carrano et al., 2014]. Application of these techniques to strong scatter measurements at Ascension Island has also led to new insights into the details of irregularity evolution at low latitudes.

Re: 3.3 Ionospheric Sensor Installations

These efforts have resulted in the successful deployment of three ionosondes. Two of them are in East Africa with one in Addis Ababa, Ethiopia and the other in Maseno, Kenya. The third system is part of the LISN network in Bolivia. At the end of this contract, all systems are operational and capable of providing continuous measurements with a cadence of 15 minutes. The data is of sufficiently high quality for inferring the major ionogram characteristics of peak density (foF2) and peak height (hmF2). The major challenges for the systems in Africa are intermittent power and internet connectivity. These challenges limit remote access, data transfers and continuous operations. However, some of these issues are improving but require frequent communication and support to the local operators. A data repository for these measurements has been established at Boston College. The data from the Ethiopian system is also available on a NOAA server (<http://ngdc.noaa.gov/ionosonde/data/AA109/individual/2014/>)

The system installed in Tupiza, Bolivia is also running continuously with few interruptions. We have now collected 2 years of data from this system. The data is currently used in studies of the variability of density profiles over the South American region. Access to the Bolivian ionosonde data is available from the LISN website (<http://lisn.igp.gob.pe>).

Under this contract, Boston College also worked with AFRL to install a 50 MHz coherent backscatter radar in Bahir Dar, Ethiopia. Currently, the radar is being operated in two modes, one targeting daytime electrojet echoes and another aimed at detecting post-sunset Spread F events.

Re: 3.4 Operations and Maintenance of SCINDA

Our efforts have supported the operations and maintenance of the SCINDA network. This is been quite a successful effort with the purchase, installation and maintenance of a number of diagnostic instruments; the initiation of routine operation of remote sites; the set-up for data transmission from remote sites to a server at Boston College on a real time basis; the provision for off-line data backup, data storage and real-time data processing. The Appendix includes the Equipment Inventory for SCINDA.

An important conclusion of this effort is that we were able to supply real-time data to the Air Force Weather Agency (AFWA) to enable the agency to continue to provide regional specification and short-term forecasts of scintillation activity. Section 3.4 illustrated the locations of the SCINDA stations together with availability results by region for the last three years of this project. Except for Central Africa, which truly is a dark and difficult place, every longitude sector enjoys at least 90% uptime with respect to regional coverage.

Finally, this contract supported a wide array of studies with successful results. Most of our results and conclusions have been published in the referred literature and are referenced in this report.

REFERENCES

Aarons, J. (1982), Global morphology of ionospheric scintillations, Proc. IEEE, 70, pp. 360-378, doi:10.1109/PROC.1982.12314.

Afraimovich, E. L., K. S. Palamartchouk, and N. P. Perevalova (1998), GPS radio interferometry of traveling ionospheric disturbances, J. Atmos. Solar-Terr. Phys., 60, pp. 1205-1223.

Akala, A. O., P. H. Doherty, C. S. Carrano, C. E. Valladares, and K. M. Groves (2012), Impacts of ionospheric scintillations on GPS receivers intended for equatorial aviation applications, Radio Sci., 47, RS4007, doi:10.1029/2012RS004995.

Basu, S., E. M. MacKenzie, Su. Basu, E. L. Costa, P. F. Fougere, H. C. Carlson, Jr., and H. E. Whitney (1987), IEEE J. on Selected Areas in Communications, v. sac-5, 2.

Beach, T. L., T. R. Pedersen, and M. J. Starks (2004), Estimating the amplitude scintillation index from sparsely sampled phase screen data, Radio Sci., 39, RS5001, doi:10.1029/2002RS002792.

Bhattacharyya, A., K. M. Groves, S. Basu, H. Kuenzler, C. E. Valladares and R. Sheehan (2003), L-band scintillation activity and space-time structure of low-latitude UHF scintillations, Radio Sci., 38(1), 1004, doi:10.1029/2002RS002711.

Carrano, C. S., K. Groves and J. Griffin (2005), Empirical Characterization and Modeling of GPS Positioning Errors Due to Ionospheric Scintillation, Proceedings of the Ionospheric Effects Symposium, Alexandria, VA, May 3-5, 2005.

Carrano, C. S. and K. M. Groves (2010), Temporal decorrelation of GPS satellite signals due to multiple scattering from ionospheric irregularities, Proceedings of the 2010 Institute of Navigation ION GNSS Meeting, Portland, OR, September 21-24.

Carrano, C. S., K. M. Groves, R. G. Caton, C. L. Rino, and P. R. Straus (2011), Multiple phase screen modeling of ionospheric scintillation along radio occultation raypaths, Radio Sci., 46, RS0D07, doi:10.1029/2010RS004591.

Carrano, C. S., K. M. Groves, and R. G. Caton (2012a), Simulating the impacts of ionospheric scintillation on L band SAR image formation, Radio Sci., 47, RS0L20, doi:10.1029/2011RS004956.

Carrano, C. S., K. M. Groves, W. J. McNeil, and P. H. Doherty (2012b), Scintillation Characteristics Across the GPS Frequency Band, Proceedings of the 25th International Technical Meeting of The Satellite Division of the Institute of Navigation (ION GNSS 2012), Nashville, TN, September 2012, pp. 1972-1989.

Carrano, S., C. Valladares, and K. Groves (2012c), Latitudinal and Local Time Variation of Ionospheric Turbulence Parameters during the Conjugate Point Equatorial Experiment in Brazil, International Journal of Geophysics, vol. 2012, Article ID 103963, doi:10.1155/2012/103963.

Carrano, C. S., K. M. Groves, and R. G. Caton (2012d), The effect of phase scintillations on the accuracy of phase screen simulation using deterministic screens derived from GPS and ALTAIR measurements, Radio Sci., 47, RS0L25, doi:10.1029/2011RS004958.

Carrano, C. S., K. M. Groves, S. H. Delay, and P. H. Doherty (2014), An Inverse Diffraction Technique for Scaling Measurements of Ionospheric Scintillations on the GPS L1, L2, and L5 Carriers to Other Frequencies, Proceedings of the 2014 Institute of Navigation ION ITM Meeting, San Diego, California, January 27-29, 2014.

Caton, R. G., C. S. Carrano, C. M. Alcala, K. M. Groves, T. Beach, and D. Sponseller (2009), Simulating the effects of scintillation on transitionospheric signals with a two-way phase screen constructed from ALTAIR phase-derived TEC, *Radio Sci.*, 44, RS0A12, doi:10.1029/2008RS004047.

Chapin, E. S. F. Chan, B. D. Chapman, C. W. Chen, J. M. Martin, T. R. Miche, R. J. Muellerschoen, X. Pi, and P. A. Rosen (2006), Impact of the ionosphere on an L-band space based radar, *2006 IEEE Conference on Radar*, 24-27 April 2006, doi: 10.1109/RADAR.2006.1631775.

Datta-Barua, S., P. H. Doherty, S. H. Delay, T. Dehel, and J. A Klobuchar (2003), Ionospheric Scintillation Effects on Single and Dual Frequency GPS Positioning, *Proceedings of the 16th International Technical Meeting of the Satellite Division of The Institute of Navigation (ION GPS/GNSS 2003)*, Portland, OR, September 2003, pp. 336-346.

Franke, S. J. and C. H. Liu (1985), Modeling of equatorial multifrequency scintillation, *Radio Science*, vol. 20, no. 3, pp. 403-415.

Fremouw, E. J. and A. Ishimaru (1992), Intensity scintillation index and mean apparent radar cross section on monostatic and bistatic paths, *Radio Sci.*, 27(4), pp. 539-543, doi:10.1029/92RS00293.

Humphreys, T. E., M. L. Psiaki, and P. M. Kintner (2010), Modeling the Effects of Ionospheric Scintillation on GPS Carrier Phase Tracking, *IEEE Trans. Aerospace Electron. Systs.* 46(4), pp, 1624-1637.

Knepp, D. L. and H. L. F. Houpis (1991), Altair VHF/UHF/observations of multipath and backscatter enhancement, *IEEE Trans. Antennas Propag.*, 39(4), pp. 528-534, doi:10.1109/8.81467.

Knepp, D. L. and W. A. Brown (1997), Average received signal power after two-way propagation through ionized turbulence, *Radio Sci.*, 32(4), pp. 1575-1596, doi:10.1029/97RS00450.

Pi, X., A. Freeman, B. Chapman, P. Rosen, and Z. Li (2011), Imaging ionospheric inhomogeneities using spaceborne synthetic aperture radar, *J. Geophys. Res.*, 116, A04303, doi:10.1029/2010JA016267.

Ratcliffe, J. A. (1956), Some aspects of diffraction theory and their application to the ionosphere, *Rep. Prog. Phys.*, 19, pp. 188-267, doi:10.1088/0034-4885/19/1/306.

Rino, C. L. (2011), *The Theory of Scintillation With Applications in Remote Sensing*, John Wiley, New York, NY, USA.

Rino, C. L. and C. S. Carrano (2013), A compact strong-scatter scintillation model, *Proceedings of the International Beacon Satellite Symposium*, July 8-12, 2013, Bath, UK.

Rogers, N. and P. Cannon (2009), The synthetic aperture radar trans-ionospheric radio propagation simulator (SAR-TIRPS), paper presented at 11th International Conference on Ionospheric Radio Systems and Techniques, Inst. of Eng. and Technol., Edinburgh, U. K., 28-30 April.

Roth, A. P., B. D. Huxtable, K. Chotoo, and S. Chotoo (2010), Simulating and mitigating ionospheric effects in synthetic aperture radar, paper presented at the 2010 IEEE International Geoscience and Remote Sensing Symposium, Honolulu, HI, July 25-30.

Secan, J., R. Bussey, E. Fremouw, and S. Basu (1995), Improved model of equatorial scintillation, *Radio Science*, vol. 30, no. 3, pp. 607-617.

Seemala, G.K. and C.E. Valladares (2011), Statistics of total electron content depletions observed over the South American continent for the year 2008, *Radio Sci.*, 46, RS5019, doi: 10.1029/2011RS004722.

Shimada, M., Y. Muraki, and Y. Otsuka (2008), Discovery of anomalous stripes over the Amazon by the PALSAR onboard ALOS satellite, paper presented at the 2008 IEEE International Geoscience and Remote Sensing Symposium, July 6-11, 2008, Boston, MA.

Spatz, D. E., S. J. Franke, and K. C. Yeh (1988), Analysis and interpretation of spaced receiver scintillation data recorded at an equatorial station, *Radio Sci.*, 23, 3, pp. 347-361.

Tsunoda, R. T. (1985), Control of the seasonal and longitudinal occurrence of equatorial scintillations by the longitudinal gradient in integrated *E* region Pedersen conductivity, *Journal of Geophysical Research*, Volume 90, Issue A1, 1 January 1985, pp. 447-456, DOI: 10.1029/JA090iA01p00447.

Vacchione, J., S. Franke, and K. Yeh (1987), A new technique for estimating zonal irregularity drifts and variability in the equatorial F region using spaced receiver scintillation data, *Radio Sci.*, 22, 5, pp. 745-756.

Valladares, C. E. and J. L. Chau (2012), The Low-Latitude Ionosphere Sensor Network: Initial Results, *Radio Sci.*, RS0L17, doi: 10.1029/2011RS004978.

Valladares, C. E. and M. A. Hei, (2012), Measurement of the Characteristics of TIDs Using Small and Regional Networks of GPS Receivers during the Campaign of 17-30 July 2008, *International Journal of Geophysics*, vol. 2012, Article ID 548784, doi:10.1155/2012/548784.

Valladares, C.E. and J. V. Eccles (2014), The Tropical Ionization Anomaly, submitted to *Geophy. Res. Lett.*, under review.

Valladares, C. E., R. Sheehan, and E. E. Pacheco (2015), Observations of MSTIDs over South and Central America, AGU monograph (accepted for publication).

Valladares, C. E., T. Pedersen, and R. Sheehan (2015), Polar Cap Patches Observed during the Magnetic Storm of November 2003: Observations and Modeling, submitted to *Ann. Geophysicae*.

Xu, Z.-W., J. Wu, Z.-S. Wu (2004), A survey of ionospheric effects on space-based radar, *Waves in Random and Complex Media*, (14) 2, pp. S189-S273.

LIST OF SYMBOLS, ABBREVIATIONS, AND ACRONYMS

1-D	One dimensional
2-D	Two dimensional
3-D	Three dimensional
AFRL	Air Force Research Laboratory
AFWA	Air Force Weather Agency
AGW	Atmospheric Gravity Waves
ALOS	Advanced Land Observation Satellite
ALTAIR	ARPA long-range tracking and identification radar
ARPA	Advanced Research Projects Agency
ATRAD	Atmospheric radars
BC	Boston College
BNR	Blue Nile Radar
C&A	Certification and Accreditation
C/N0	Carrier to Noise Ratio
CCM	Cross Correlation Method
CG	Corrected Geomagnetic
CGLAT	Corrected geomagnetic latitude
CLM	Correlation Length Mapping
dB	decibels
DMSP	Defense Meteorological Satellite Program
DoD	Department of Defense
DOY	Day of Year
E _s	Sporadic E
EUV	Extreme Ultra Violet
EUVAC	Solar EUV flux model for aeronomic calculations
E-W	East to West Direction
F0F2	Peak density
FOPEN	Foliage Penetrating Radars
GOES	Geostationary Satellite System
GPS	Global Positioning System
GTIM	Global Theoretical Ionospheric Model
GW	Gravity Waves
HWM	Hedin's Wind Model
IGRF	International Geomagnetic Reference Field
IMF	Interplanetary Magnetic Field
InSar	Interferometric synthetic aperture radar
IPE	Irregularity Parameter Estimation
IPP	Ionospheric Pierce Point
ISR	Incoherent Scatter Radar
IT	Information Technology
ITCZ	Intertropical Convergence Zone
L Band	1210 MHz; 1-2 GHz range of radio spectrum
LCS	Liquid Cooling System
LEO	Low Earth Orbit

LISN	Low Latitude Sensor Network
LLIONS	Low-latitude ionospheric sector
LOS	Line Of Sight
LT	Local Time
MHz	MegaHertz
M-I	Magnetosphere-Ionosphere
MLAT	Magnetic latitude
MSID	Medium scale traveling ionospheric disturbances
MSIS90	Mass spectrometer and incoherent scatter model
NEC	National Electrical Code
N-M TECE	Near midnight TEC enhancements
NOAA	National Oceanic and Atmospheric Administration
N-S	North to South Direction
O&M	Operations and Maintenance
Ohms	Unit of electrical resistance
PALSOR	Phased array type L-band synthetic aperture radar
PC	Personal Computer
PRN	Pseudo-random number representing GPS satellite
PVC	Poly vinyl chloride
PWE	Parabolic Wave Equation
RCS	Radar Cross Section
RF	Radio Frequency
RX	Receiver
S4	Index for strength of scintillation
SADM-GPS	Statistical angle of arrival and Doppler method for GPS interferometry
SAR	Synthetic Aperture Radar
SAR-SS	SAR Scintillation Simulator
SATCOM	Family of communication satellites
SCINDA	Scintillation Network and Decision Aid
SNR	Signal to Noise Ratio
T/R	Trans receiver
TEC	Total Electron Content
TECP	Perturbed TEC
TECu	Total Electron Content Unit
TID	Traveling Ionospheric Disturbances
TOMCO	Commercial RF Amplifier
TS	Tropical Storm
U	Universal Scaling Parameter
UHF	Ultra High Frequency
UT	Universal Time
UV	Ultra Violet
VHF	Very High Frequency
VIPIR	Vertical Incidence Pulsed Ionospheric Radar
VSWR	Voltage Standard Wave Radio
WBMOD	Wideband scintillation model
WIDE	Wideband Ionospheric Distortion Experiment

dTEC	Differential Total Electron Content
hmF2	Peak height
superDARN	Super Dual Auroral Radar Network
upB	Radar pointing along magnetic field
USAF	United States Air Force
USRP	Universal Software Radio Peripheral

APPENDIX – EQUIPMENT LIST FOR SCINDA O&M

Funding source	Descr	Serial ID	Acquisition date	Offsite	Offsite Location	Quantity Received/ Fabricated	Unit Acquisition Cost	BC Project/Grant	Contract Number
GPE - govt issued	GPS RECEIVERS ONR FOR ISR	NYMD055000-03	05/14/2012	Y	Sal, Cape Verde	1	\$6,000.00	5001336	FA8718-09-C-0041
GPE - govt issued	GPS RECEIVERS ONR FOR ISR	NYMD063000-02	05/14/2012	Y	Akure, Nigeria	1	\$6,000.00	5001336	FA8718-09-C-0041
GPE - govt issued	GPS RECEIVERS ONR FOR ISR	NYMD062900-06	05/14/2012	Y	Jhongli-City, Taiwan	1	\$6,000.00	5001336	FA8718-09-C-0041
GPE - govt issued	GPS RECEIVERS ONR FOR ISR	NYMD062900-09	05/14/2012	Y	Kirtland AFB	1	\$6,000.00	5001336	FA8718-09-C-0041
GPE - govt issued	GPS RECEIVERS ONR FOR ISR	NYMD062900-12	05/14/2012	Y	Guam	1	\$6,000.00	5001336	FA8718-09-C-0041
GPE - govt issued	GPS RECEIVERS ONR FOR ISR	NYMD062900-13	05/14/2012	Y	Gakona, Alaska (HAARP)	1	\$6,000.00	5001336	FA8718-09-C-0041
GPE - govt issued	GPS RECEIVERS ONR FOR ISR	NYMD062900-14	05/14/2012	Y	Kirtland AFB	1	\$6,000.00	5001336	FA8718-09-C-0041
GPE - govt issued	GPS RECEIVERS ONR FOR ISR	NYMD062900-16	05/14/2012	Y	Bahir Dar, Ethiopia	1	\$6,000.00	5001336	FA8718-09-C-0041
GPE - govt issued	GPS RECEIVERS ONR FOR ISR	NYMD062900-18	05/14/2012	Y	Rajkot, India	1	\$6,000.00	5001336	FA8718-09-C-0041
GPE - govt issued	GPS RECEIVERS ONR FOR ISR	NYMD062900-19	05/14/2012	Y	Addis Ababa, Ethiopia	1	\$6,000.00	5001336	FA8718-09-C-0041
GPE - govt issued	GPS RECEIVERS ONR FOR ISR	NYMD062900-20	05/14/2012	Y	millstone hill 3	1	\$6,000.00	5001336	FA8718-09-C-0041
GPE - govt issued	GPS RECEIVERS ONR FOR ISR	NYMD062900-26	05/14/2012	Y	millstone hill 2	1	\$6,000.00	5001336	FA8718-09-C-0041
GPE - govt issued	GPS RECEIVERS ONR FOR ISR	NYMD062900-33	05/14/2012	Y	Kirtland AFB	1	\$6,000.00	5001336	FA8718-09-C-0041
GPE - govt issued	GPS RECEIVERS ONR FOR ISR	NYMD062900-37	05/14/2012	Y	Kirtland AFB	1	\$6,000.00	5001336	FA8718-09-C-0041
GPE - govt issued	GPS RECEIVERS ONR FOR ISR	NYMD062900-45	05/14/2012	Y	Greensboro, NC (NC A&T)	1	\$6,000.00	5001336	FA8718-09-C-0041
GPE - govt issued	GPS RECEIVERS ONR FOR ISR	NYMD062900-46	05/14/2012	Y	Diego Garcia	1	\$6,000.00	5001336	FA8718-09-C-0041
GPE - govt issued	GPS RECEIVERS ONR FOR ISR	NYMD062900-49	05/14/2012	Y	Abijan, Ivory Coast	1	\$6,000.00	5001336	FA8718-09-C-0041
GPE - govt issued	GPS RECEIVERS ONR FOR ISR	NYMD062900-51	05/14/2012	Y	Kolka, India	1	\$6,000.00	5001336	FA8718-09-C-0041
GPE - govt issued	GPS RECEIVERS ONR FOR ISR	NYMD062900-60	05/14/2012	Y	Tirunelveli, India	1	\$6,000.00	5001336	FA8718-09-C-0041
GPE - govt issued	GPS RECEIVERS ONR FOR ISR	NYMD062900-61	05/14/2012	Y	Nairobi, Kenya	1	\$6,000.00	5001336	FA8718-09-C-0041
GPE - govt issued	GPS RECEIVERS ONR FOR ISR	NYMD062900-62	05/14/2012	Y	millstone hill 11	1	\$6,000.00	5001336	FA8718-09-C-0041
GPE - govt issued	GPS RECEIVERS ONR FOR ISR	NYMD062900-65	05/14/2012	Y	Manila, Philippines	1	\$6,000.00	5001336	FA8718-09-C-0041
GPE - govt issued	GPS RECEIVERS ONR FOR ISR	NYMD073000-01	05/14/2012	Y	Kirtland AFB	1	\$6,000.00	5001336	FA8718-09-C-0041
GPE - govt issued	GPS RECEIVERS ONR FOR ISR	NYMD073000-02	05/14/2012	Y	Nsukka, Nigeria	1	\$6,000.00	5001336	FA8718-09-C-0041
GPE - govt issued	GPS RECEIVERS ONR FOR ISR	NYMD073300-01	05/14/2012	Y	Kirtland AFB	1	\$6,000.00	5001336	FA8718-09-C-0041
GPE - govt issued	GPS RECEIVERS ONR FOR ISR	NYMD073300-02	05/14/2012	Y	Cairo, Egypt	1	\$6,000.00	5001336	FA8718-09-C-0041
GPE - govt issued	GPS RECEIVERS ONR FOR ISR	NYMD073300-04	05/14/2012	Y	Singapore	1	\$6,000.00	5001336	FA8718-09-C-0041
GPE - govt issued	GPS RECEIVERS ONR FOR ISR	NYMD073300-05	05/14/2012	Y	Nairobi, Kenya	1	\$6,000.00	5001336	FA8718-09-C-0041
GPE - govt issued	GPS RECEIVERS ONR FOR ISR	NYMD073300-06	05/14/2012	Y	Kirtland AFB	1	\$6,000.00	5001336	FA8718-09-C-0041
GPE - govt issued	GPS RECEIVERS ONR FOR ISR	NYMD073300-07	05/14/2012	Y	Brazzaville, Republic of Congo	1	\$6,000.00	5001336	FA8718-09-C-0041
GPE - govt issued	GPS RECEIVERS ONR FOR ISR	NYMD073300-10	05/14/2012	Y	Kampala, Uganda	1	\$6,000.00	5001336	FA8718-09-C-0041
GPE - govt issued	GPS RECEIVERS ONR FOR ISR	NYMD074700-01	05/14/2012	Y	Brazil	1	\$6,000.00	5001336	FA8718-09-C-0041
GPE - govt issued	GPS RECEIVERS ONR FOR ISR	NYMD074700-06	05/14/2012	Y	Portugal	1	\$6,000.00	5001336	FA8718-09-C-0041
GPE - govt issued	GPS RECEIVERS ONR FOR ISR	NYMD074700-07	05/14/2012	Y	Brazil	1	\$6,000.00	5001336	FA8718-09-C-0041
GPE - govt issued	GPS RECEIVERS ONR FOR ISR	NYMD074700-15	05/14/2012	Y	Brazil	1	\$6,000.00	5001336	FA8718-09-C-0041
GPE - govt issued	GPS RECEIVERS ONR FOR ISR	NYMD074700-16	05/14/2012	Y	Kirtland AFB	1	\$6,000.00	5001336	FA8718-09-C-0041
GPE - govt issued	GPS RECEIVERS ONR FOR ISR	NYMD062900-09	05/14/2012	Y	Kolka, India	1	\$6,000.00	5001336	FA8718-09-C-0041
GPE - govt issued	GPS RECEIVERS ONR FOR ISR	NYMD062900-47	05/14/2012	Y	AFLRL/RY, Rome-Roatan, Hond	1	\$6,000.00	5001336	FA8718-09-C-0041
GPE - govt issued	GPS RECEIVERS ONR FOR ISR	NHVD062900-13	05/14/2012	Y	AFLRL/RY, Rome-Seoul Korea	1	not a receiver, only an antenna	5001336	FA8718-09-C-0041
GPE - govt issued	GPS RECEIVERS ONR FOR ISR	NYME062900-30	05/14/2012	Y	AFLRL/RY, Rome-Quebec	1	\$6,000.00	5001336	FA8718-09-C-0041
GPE - govt issued	GPS RECEIVERS ONR FOR ISR	NYMD062900-31	05/14/2012	Y	AFLRL/RY, Rome-Wright-Pat	1	\$6,000.00	5001336	FA8718-09-C-0041
					Transfer Date				
xfer from 0055 to 0041	Iono sonde	none available	12/4/13	Y	Addis Ababa, Ethiopia	1	\$86,000.00	5001336	FA8718-09-C-0041
xfer from 0055 to 0041	Iono sonde	none available	12/4/13	Y	Maseno, Kenya	1	\$86,000.00	5001336	FA8718-09-C-0041
purchased w/govt funded award	PowerEdge Server with Accessor	JDC8C21	1/16/14	N	17601106J	1	8,580.63	5001336	FA8718-09-C-0041
purchased w/govt funded award	GPS Receivers	NYM10160009	5/21/10	Y	Bangkok, Thailand	1	6,995.00	5001399	FA8718-09-C-0041
purchased w/govt funded award	GPS Receivers	NYM10160010	5/21/10	Y	Chiang Mai, Thailand	1	6,995.00	5001399	FA8718-09-C-0041
purchased w/govt funded award	GPS Receivers	NYM10160011	5/21/10	Y	Niamey, Niger	1	6,995.00	5001399	FA8718-09-C-0041
purchased w/govt funded award	GPS Receivers	NYM10160012	5/21/10	Y	Kwajalein	1	6,995.00	5001399	FA8718-09-C-0041
purchased w/govt funded award	GPS Receivers	NYM10160002	5/21/10	Y	Zanzibar, Tanzania	1	6,995.00	5001399	FA8718-09-C-0041
purchased w/govt funded award	GPS Receivers	NYM10160003	5/21/10	Y	Brazzaville, Congo	1	6,995.00	5001399	FA8718-09-C-0041
purchased w/govt funded award	GPS Receivers	NYM10160004	5/21/10	Y	Mbarara, Uganda	1	6,995.00	5001399	FA8718-09-C-0041
purchased w/govt funded award	Dell PowerEdge R510	4013JN1	7/20/10	N	Boston College, 24401	1	6,322.39	5001399	FA8718-09-C-0041
purchased w/govt funded award	GSV4004B Receiver	NYM10210001	1/13/11	Y	Kirtland AFB, NM	1	8,170.00	5001526	FA8718-09-C-0041
purchased w/govt funded award	GSV4004B Receiver	NYM10210004	1/13/11	Y	Kinshasa, DRC	1	8,170.00	5001526	FA8718-09-C-0041
purchased w/govt funded award	GSV4004B Receiver	NYM10210007	1/13/11	Y	Christmas Island, Australia	1	8,170.00	5001526	FA8718-09-C-0041
purchased w/govt funded award	GSV4004B Receiver	NYM10210009	1/13/11	Y	Kisangani, DRC	1	8,170.00	5001526	FA8718-09-C-0041
purchased w/govt funded award	GSV4004B Receiver	NYM10390005	1/13/11	Y	Seychelles	1	8,170.00	5001526	FA8718-09-C-0041
purchased w/govt funded award	GSV4004B Receiver	NYM10390006	1/13/11	Y	Abidjan, Ivory Coast	1	8,170.00	5001526	FA8718-09-C-0041
purchased w/govt funded award	GSV4004B Receiver	NYM10430001	1/13/11	Y	Phuket, Thailand	1	8,170.00	5001526	FA8718-09-C-0041
purchased w/govt funded award	GSV4004B Receiver	NYM10430002	1/13/11	Y	Taipei, Taiwan	1	8,170.00	5001526	FA8718-09-C-0041
purchased w/govt funded award	GSV4004B Receiver	NYM10430004	1/13/11	Y	Koudougou, Burkina Faso	1	8,170.00	5001526	FA8718-09-C-0041
purchased w/govt funded award	GSV4004B Receiver	NYM10430005	1/13/11	Y	Dakar, Senegal	1	8,170.00	5001526	FA8718-09-C-0041
purchased w/govt funded award	GSV4004B Receiver	NYM10430007	1/13/11	Y	Wahlawa, HI	1	8,170.00	5001526	FA8718-09-C-0041
purchased w/govt funded award	GSV4004B Receiver	NYM10430008	1/13/11	Y	Apiai, Colombia	1	8,170.00	5001526	FA8718-09-C-0041
purchased w/govt funded award	GSV4004B Receiver	NYM10430009	1/13/11	Y	Kwajalein	1	8,170.00	5001526	FA8718-09-C-0041
purchased w/govt funded award	GSV4004B Receiver	NYM10430010	1/13/11	Y	Christmas Island, Australia	1	8,170.00	5001526	FA8718-09-C-0041
purchased w/govt funded award	Generators (2) - 5001526	2003894	9/9/11	Y	Sao Jose Campos, Brazil	1	10,268.00	5001526	FA8718-09-C-0041
purchased w/govt funded award	Generators (2) - 5001526	n/a	9/13/11	Y	Christmas Island, Kiribati	1	8,983.50	5001526	FA8718-09-C-0041
purchased w/govt funded award	GPS Receiver	NMAS12030005R	6/25/12	N	Boston College, 17601219	1	13,162.00	5001686	FA8718-09-C-0041
purchased w/govt funded award	GPS Receiver	NMAS11470005H	6/25/12	Y	Sao Jose Campos, Brazil	1	13,162.00	5001686	FA8718-09-C-0041
purchased w/govt funded award	GPS Receivers	NMAS12350004R	9/11/12	N	Boston College, 17601205	1	14,324.00	5001686	FA8718-09-C-0041
purchased w/govt funded award	GPS Receivers	NMAS12350005E	9/11/12	N	Boston College, 17601205	1	14,324.00	5001686	FA8718-09-C-0041
purchased w/govt funded award	GPS Receivers	NMAS12360009N	9/11/12	N	Boston College, 17601205	1	14,324.00	5001686	FA8718-09-C-0041
purchased w/govt funded award	PolaRxS Pro Receiver	2003928	12/31/12	Y	Wallops Island, VA	1	13,898.00	5001842	FA8718-09-C-0041
purchased w/govt funded award	GPS Recovier (GSV4004B)	NYM1044008	10/31/12	N	Boston College, 17601219	1	8,095.00	5001842	FA8718-09-C-0041
purchased w/govt funded award	Dell PowerVault Server Storage	JDC8CZ1	12/9/14	N	Boston College, 17601106J	1	15,685.74	5001875	FA8718-09-C-0041
purchased w/govt funded award	RF Power Amplifier	10302	1/4/14	Y	Bahia Dar, Ethiopia	1	48,510.00	5001875	FA8718-09-C-0041
purchased w/govt funded award	Box w/ 4X VHF T/R Switches	003,004	3/11/14	Y	Bahia Dar, Ethiopia	1	6,958.75	5001875	FA8718-09-C-0041
purchased w/govt funded award	Antenna Array System	n/a	4/11/14	Y	Bahia Dar, Ethiopia	1	6,925.51	5001875	FA8718-09-C-0041
purchased w/govt funded award	PolaRxS Pro Receiver	2003960	5/13/14	Y	Rome, NY	1	10,425.00	5001875	FA8718-09-C-0041
purchased w/govt funded award	Antenna Array System	n/a	6/1/14	N	Bahia Dar, Ethiopia	1	84,134.37	5001875	FA8718-09-C-0041
purchased w/govt funded award	USRP x300 (2)	F51CA7, F517C8	8/25/14	N	Bahia Dar, Ethiopia	1	6,669.01	5001875	FA8718-09-C-0041
purchased w/govt funded award	USRP N210 Kit + Otdt Clock	F43075	11/15/13	Y	Bahia Dar, Ethiopia	1	7,105.00	5002051	FA8718-09-C-0041
							\$656,185.40		
							\$896,185.40		

DISTRIBUTION LIST

DTIC/OCP
8725 John J. Kingman Rd, Suite 0944
Ft Belvoir, VA 22060-6218 1 cy

AFRL/RVIL
Kirtland AFB, NM 87117-5776 2 cys

Official Record Copy
AFRL/RVBYE/Dr. James T. Keeney 1 cy

This page is intentionally left blank.